

**SOLUTION OF HIGH SPEED FLOWS
USING
THREE DIMENSIONAL METHOD OF CHARACTERISTICS**

76085

**A THESIS SUBMITTED TO
THE GRADUATE SCHOOL OF NATURAL AND APPLIED SCIENCES
OF
THE MIDDLE EAST TECHNICAL UNIVERSITY**


BY

ERTUĞRUL ALP BAŞEŞME

**IN PARTIAL FULFILLMENT OF THE REQUIREMENTS FOR THE DEGREE OF
DOCTOR OF PHILOSOPHY
IN
THE DEPARTMENT OF MECHANICAL ENGINEERING**

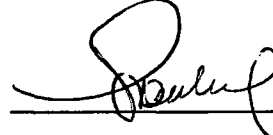
JANUARY 1998

Approval of the Graduate School of Natural and Applied Sciences



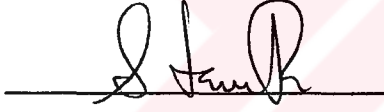
Prof. Dr. Fayfur ÖZTÜRK
Director

I certify that this thesis satisfies all the requirements as a thesis for the degree of Doctor of Philosophy.



Prof. Dr. Ediz PAYKOÇ
Head of Department

This is to certify that we have read this thesis and that in our opinion it is fully adequate, in scope and quality, as a thesis for the degree of Doctor of Philosophy.



Assoc. Prof. Dr. İ. Sinan AKMANDOR
Co-Supervisor



Prof. Dr. Ahmet Ş. ÜÇER
Supervisor

Examining Committee Members

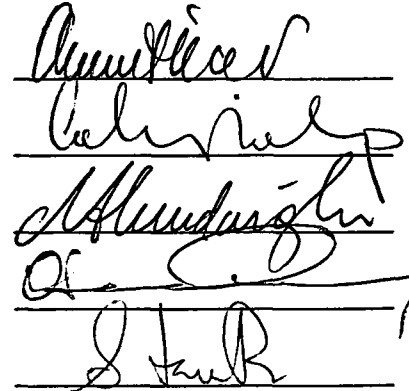
Prof. Dr. Ahmet Ş. ÜÇER (supervisor)

Prof. Dr. Cahit ERALP

Prof. Dr. Nafiz ALEMDAROĞLU

Prof. Dr. Ali DURMAZ

Assoc. Prof. Dr. İ. Sinan AKMANDOR



ABSTRACT

SOLUTION OF HIGH SPEED FLOWS USING THREE DIMENSIONAL METHOD OF CHARACTERISTICS

BAŞEŞME, Ertuğrul Alp

Ph.D., Department of Mechanical Engineering

Supervisor: Prof. Dr. Ahmet Ş. ÜÇER

Co-Supervisor: Assoc. Prof. Dr. İ. Sinan AKMANDOR

January 1998, 110 Pages

A three-dimensional explicit time marching numerical code has been developed which can simulate subsonic, transonic and supersonic inviscid internal flows. The formulation is based on the QAZ1D method of Verhoff and uses natural streamline coordinate system. The unsteady Euler equations in non-conservative form are expressed in terms of extended Riemann variables. The other dependent variables are entropy and flow angles. In this form, multidimensional equations reduce to a quasi-one dimensional system which is in the characteristic form. Euler equations when expressed along the characteristic trajectories in the space-time domain reduce to a system of ordinary differential equations which can be solved numerically. The solution scheme is first order accurate in space and time. Boundary conditions are implemented in the characteristic form and are physically consistent. Shock waves are automatically captured by the method, but a one-point shock correction must be employed after each iteration to maintain conservation across the discontinuity. Steady flow solutions are obtained as the asymptotic solution in time.

The developed code has been applied to a wide range of subsonic, transonic and supersonic test cases. Despite the wide range in the Mach number and diversity of flow geometries which have been tested, close agreement have been obtained with available analytical and numerical results associated with these test cases.

Keywords: Euler Solver, Finite Difference, Time-Marching, Characteristic Method, Three-Dimensional Flow



ÖZ

YÜKSEK HIZLI AKIŞLARIN ÜÇ BOYUTLU KARAKTERİSTİK METOD KULLANILARAK ÇÖZÜMÜ

BAŞEŞME, Ertuğrul Alp

Doktora, Makina Mühendisliği Bölümü

Tez Yöneticisi: Prof. Dr. Ahmet Ş. ÜÇER

Yardımcı Tez Yöneticisi: Assoc. Prof. Dr. İ. Sinan AKMANDOR

Ocak 1998, 110 Sayfa

Üç boyutlu sesaltı, ses civarı ve sesüstü hızlı sürtünmesiz iç akışı simüle eden zamanda ilerleyen bir sayısal algoritma geliştirilmiştir. Formülasyonda Verhoff'un QAZ1D metodu esas alınmış olup, doğal akım çizgisi koordinat sistemi kullanılmaktadır. Zamana bağımlı Euler denklemleri genişletilmiş Riemann değişkenleri cinsinden *non-conservatif* formda ifade edilmiştir. Kullanılan diğer değişkenler entropi ve akım açılarıdır. Bu şekilde, üç boyutlu denklemler karakteristik formdaki bir boyutlu denklem sistemlerine dönüşür. Euler denklemleri uzay-zaman düzleminde karakteristik yörüngeler üzerinde ifade edildiklerinde sayısal olarak çözülebilen *ordinary* diferansiyel denklem sistemlerine indirgenir. Çözüm yöntemi uzayda ve zamanda birinci derece hassastır. Sınır şartları karakteristik formda ve fiziksel olarak tutarlı bir şekilde hesaba katılmıştır. Şok dalgaları otomatik olarak yakalanmakta olup, şok civarında korunmanın sağlanması için her zaman diliminde noktasal şok düzeltmesi gereklidir.

Geliştirilen yöntem ile sesaltı, ses civarı ve sesüstü akım rejimlerinde değişik problemler çözülmüştür. Çözülen problemlerdeki Mach sayısı ve akış

geometrisindeki çeşitliliğe rağmen, analitik veya sayısal yöntemlerle yakın sonuçlar elde edilmiştir.

Anahtar Kelimeler: Euler Çözücüsü, Sonlu Fark, Zamanda İlerleme, Karakteristik Metod, Üç Boyutlu Akış.





To my dear wife, my son and my parents

ACKNOWLEDGMENTS

I would like to express my gratitude to Prof. Dr. Ahmet Ş. Üçer for his invaluable guidance and support throughout this study.

I would also like to thank to my co-supervisor Assoc. Prof. Dr. İ. Sinan Akmandor, for his advice and encouragement.

I would like to thank to ROKETSAN for supporting this study.

I would like to thank my wife and my son for their patience and support.

Finally my thanks go to my parents, without their support this work could not be completed.

TABLE OF CONTENTS

ABSTRACT	iii
ÖZ	v
ACKNOWLEDGMENTS	viii
TABLE OF CONTENTS	ix
LIST OF TABLES	xi
LIST OF FIGURES	xii
LIST OF SYMBOLS	xv
CHAPTERS	
1. INTRODUCTION	1
2. GOVERNING EQUATIONS	5
2.1. EULER EQUATIONS	5
2.2. NON-DIMENSIONALIZATION.....	8
3. SOLUTION ALGORITHM	9
3.1. METHOD OF CHARACTERISTICS	9
3.2. SOLUTION METHOD.....	10
3.3. INVERSE MARCHING PROCEDURE.....	12
3.4. SHOCK CORRECTION.....	24
3.5. PROGRAMMING	31
4. BOUNDARY CONDITIONS	35
4.1. FARFIELD BOUNDARY CONDITIONS.....	36
4.2. SOLID WALL BOUNDARY CONDITIONS.....	41
4.3. PERIODIC BOUNDARY CONDITIONS.....	44

5. RESULTS AND DISCUSSION.....	49
5.1. SHOCK TUBE (1D).....	51
5.2. TRANSONIC LAVAL NOZZLE (Q1D).....	57
5.3. RECTANGULAR INLET (2D).....	62
5.4. SINUSOIDAL BUMP (2D).....	66
5.5. SUPERSONIC CONSTANT AREA DUCT (3D).....	73
5.6. 90° BEND (3D).....	80
6. CONCLUSION.....	87
6.1. SUMMARY OF THE WORK.....	87
6.2. FUTURE WORK.....	90
REFERENCES.....	91
APPENDICES	
A. EULER EQUATION EXPRESSED IN NATURAL STREAMLINE COORDINATE SYSTEM.....	94
B. SPLITTING OF MATRICES.....	96
C. DIFFERENCE EQUATIONS.....	99
D. SHOCK EQUATIONS.....	101
E. NODE TYPES.....	103
F. COMPONENTS OF UNIT VECTORS s, n & m.....	109
VITA.....	110

LIST OF TABLES

TABLE

3.1.	<i>Computational cells used in calculating s and n derivatives</i>	18
3.2.	<i>Primitive node tags</i>	33
4.1.	<i>Variables specified as far-field numerical boundary conditions</i>	41
5.1.	<i>Summary of test cases</i>	50
C.1.	<i>Finite Difference Equations Used in Calculation of $\frac{\partial w}{\partial s}$, $\frac{\partial w}{\partial n}$ and $\frac{\partial w}{\partial m}$</i>	99
E.1.	<i>Specific Factors for Different Characters</i>	103
E.2.	<i>Node tags in two-dimensional flow with solid wall boundaries</i>	104
E.3.	<i>Node tags in two-dimensional flow with solid wall boundaries</i>	104
E.4.	<i>Node tags in two-dimensional flow with solid wall and periodic boundaries</i>	105
E.5.	<i>Node tags in three-dimensional flow with solid wall boundaries</i>	106
E.6.	<i>Node tags in three-dimensional flow with solid wall and periodic boundaries</i>	107
E.7.	<i>Node tags in three-dimensional flow with solid wall and periodic boundaries</i>	108

LIST OF FIGURES

FIGURE

2.1.	<i>Definition of flow angles and streamline coordinates</i>	6
3.1.	<i>Characteristic trajectories in the space-time domain (1D).....</i>	13
3.2.	<i>Marching algorithm for the inverse marching method.....</i>	13
3.3.	<i>Characteristic trajectories in the space-time domain (2D).....</i>	14
3.4.	<i>Characteristic trajectories in the space-time domain (3D).....</i>	15
3.5.	<i>Inverse marching procedure.....</i>	20
3.6.	<i>Shock wave with high pressure to the left.....</i>	25
3.7.	<i>Shock wave with high pressure to the right</i>	26
3.8.	<i>Reimann variable change across a shock wave.....</i>	26
3.9.	<i>Shock jump correction procedure.....</i>	28
3.10.	<i>Shock on a two dimensional grid.....</i>	29
3.11.	<i>Program flowchart.....</i>	32
4.1.a	<i>Subsonic inflow boundary in one-dimensional flow</i>	37
4.1.b	<i>Subsonic inflow boundary in two-dimensional flow</i>	37
4.2.a	<i>Supersonic inflow boundary in one-dimensional flow.....</i>	38
4.2.b	<i>Supersonic inflow boundary in two-dimensional flow.....</i>	38
4.3.a	<i>Subsonic outflow boundary in one-dimensional flow</i>	39
4.3.b	<i>Subsonic outflow boundary in two-dimensional flow</i>	39
4.4.a	<i>Supersonic outflow boundary in one-dimensional flow.....</i>	40
4.4.b	<i>Supersonic outflow boundary in two-dimensional flow.....</i>	40
4.5.a	<i>Subsonic solid wall boundary in two-dimensional flow.....</i>	42
4.5.b	<i>Supersonic solid wall boundary in two-dimensional flow</i>	42
4.6.	<i>Phantom node P1 (linear cascade).....</i>	45
4.7.	<i>Phantom node P2 (linear cascade).....</i>	45
4.8.	<i>Phantom node P1 (annular cascade).....</i>	46
4.9.	<i>Phantom node P2 (annular cascade).....</i>	47
5.1.1.	<i>Shock tube at time=0 and time=t.....</i>	52
5.1.2.	<i>Velocity distribution along the shock tube.....</i>	53
5.1.3.	<i>Entropy distribution along the shock tube</i>	53
5.1.4.	<i>Pressure distribution along the shock tube.....</i>	54
5.1.5.	<i>Density distribution along the shock tube.....</i>	54

5.1.6.	<i>Change of flow velocity across the zones.....</i>	55
5.1.7.	<i>Change of entropy across the zones.....</i>	55
5.1.8.	<i>Change of pressure across the zones</i>	56
5.1.9.	<i>Change of density across the zones</i>	56
5.2.1.	<i>Converging-diverging nozzle geometry</i>	58
5.2.2.	<i>Unsteady evolution of the flow.....</i>	59
5.2.3.	<i>Steady state pressure distribution along the converging-diverging nozzle.....</i>	59
5.2.4.	<i>Steady state density distribution along the converging-diverging nozzle.....</i>	60
5.2.5.	<i>Steady state velocity distribution along the converging-diverging nozzle.....</i>	60
5.2.6.	<i>Convergence history</i>	61
5.2.7.	<i>Shock location and its effect on convergence history</i>	61
5.3.1.	<i>Convergence history</i>	62
5.3.2.	<i>71x21 computational mesh</i>	63
5.3.3.	<i>Pressure contours</i>	63
5.3.4.	<i>Mach number contours</i>	64
5.3.5.	<i>Mach number contours [2]</i>	64
5.3.6.	<i>Flow angle (θ) contours.....</i>	65
5.3.7.	<i>Flow angle (θ) contours [2].....</i>	65
5.4.1.	<i>Convergence history</i>	66
5.4.2.	<i>161x41 computational mesh</i>	67
5.4.3.	<i>161x41 computational mesh [12]</i>	67
5.4.4.	<i>Mach number contours</i>	68
5.4.5.	<i>Mach number contours [12]</i>	68
5.4.6.	<i>Pressure contours</i>	69
5.4.7.	<i>Pressure contours [12].....</i>	69
5.4.8.	<i>Flow angle (θ) contours.....</i>	70
5.4.9.	<i>Flow angle (θ) contours [12].....</i>	70
5.4.10.	<i>Mach number distribution along the walls</i>	71
5.4.11.	<i>Mach number distribution along the walls [12]</i>	71
5.4.12.	<i>Pressure distribution along the walls</i>	72
5.4.13.	<i>Pressure distribution along the walls [12].....</i>	72
5.5.1.	<i>21x21x21 computational mesh</i>	74
5.5.2.	<i>Convergence history</i>	74
5.5.3.	<i>Mach contours at $x/L=0.20$</i>	75
5.5.4.	<i>Mach contours at $x/L=0.45$</i>	75
5.5.5.	<i>Mach contours at $x/L=0.70$</i>	76
5.5.6.	<i>Mach contours at $x/L=0.95$</i>	76
5.5.7.	<i>Mach contours at $y/h=0$.....</i>	77
5.5.8.	<i>Mach contours at $y/h=1.0$.....</i>	77

5.5.9.	<i>Mach contours at $z/w=0$</i>	78
5.5.10.	<i>Mach contours at $z/w=1.0$</i>	78
5.5.11.	<i>Mach contours [13]</i>	79
5.6.1.	<i>Duct geometry and coordinate system</i>	80
5.6.2.a.	<i>71x11x11 computational mesh</i>	81
5.6.2.b.	<i>Side view of the 71x11x11 computational mesh</i>	81
5.6.2.c.	<i>Cross-section of the 71x11x11 computational mesh</i>	82
5.6.3.	<i>Inlet velocity profile</i>	82
5.6.4.	<i>Convergence history</i>	83
5.6.5.	<i>Flow angle (θ) contours at $\alpha=45^\circ$ plane</i>	83
5.6.6.	<i>Flow angle (ϕ) contours at $\alpha=45^\circ$ plane</i>	84
5.6.7.	<i>Mach contours at $\alpha=45^\circ$ plane</i>	84
5.6.8.	<i>Pressure contours at $\alpha=45^\circ$ plane</i>	85
5.6.9.	<i>Velocity vectors at $\alpha=45^\circ$ plane</i>	85
5.6.10.	<i>Streamlines at $\alpha=45^\circ$ plane</i>	86
E.1.	<i>Two-dimensional flow with solid wall boundaries</i>	104
E.2.	<i>Two-dimensional flow with solid wall boundaries</i>	104
E.3.	<i>Two-dimensional flow with solid wall and periodic boundaries</i>	105
E.4.	<i>Three-dimensional flow with solid wall boundaries</i>	106
E.5.	<i>Three-dimensional flow with solid wall and periodic boundaries</i>	107
E.6.	<i>Three-dimensional flow with solid wall and periodic boundaries</i>	108
F.1.	<i>Streamline coordinate system</i>	109

LIST OF SYMBOLS

a	Speed of sound
d	Differential
e	Internal energy per unit mass
h	Height
J	Jacobian
M	Mach number
CFL	Courant-Friedrich-Lewy number
L	Length
LE	Leading edge
m	Unit vector normal to the streamline and n-direction
n	Unit vector normal to the streamline direction (in the plane defined by the y-axis and s vector)
p	Pressure
P	Logarithm of pressure ($P \equiv \ln(p)$)
Q	Modified Riemann variable ($Q \equiv q + a S$) Heat transfer ($dQ \equiv de + p dv$)
q	Flow speed
R	Modified Riemann variable ($R \equiv q - a S$) Gas constant
S	Modified entropy ($dS \equiv -\frac{1}{\gamma} \frac{dQ}{T}$)
s	Unit vector in the streamline direction
t	Time
T	Temperature
TE	Trailing edge
u	Velocity magnitude relative to a steady shock wave
v	Specific volume
V _s	Shock velocity

W	Upstream Mach number relative to a steady shock
w	Vector of the principle variables, Q, R, S, θ, ϕ
	Width
x	Spatial variable
y	Spatial variable
z	Spatial variable
	Vector of the right hand sides of the governing equations

Greek Symbols

∇	Gradient operator
∂	Partial derivative operator
Δt	Time step
α	Pitch of annular cascade
ϕ	Flow angle
γ	Ratio of specific heats
η	Spatial variable in the computational domain
λ	Characteristic (eigen value)
	The slope of characteristic trajectory in the space-time plane
θ	Flow angle
ρ	Density
ξ	Spatial variable in the computational domain
ζ	Spatial variable in the computational domain

Subscripts

i	Node index (along x direction)
j	Node index (along y direction)
k	Node index (along z direction)
m	m-derivative
n	n-derivative
o	Reference condition (stagnation condition)
s	s-derivative
x	x-component or x-derivative
y	y-component or y-derivative
z	z-component or z-derivative

η η -derivative
 ξ ξ -derivative
 ζ ζ -derivative

Superscripts

c **Corrector**
n **n-the time level**
 Normal
p **Predictor**
' **Dimensional flow variable**



CHAPTER 1

INTRODUCTION

Obtaining solutions to the governing equations of fluid mechanics to calculate the fluid flow around bodies for different speed regimes represents one of the most challenging problems in science and engineering.

Pioneering studies were devoted to solving the equations of fluid mechanics analytically using simplifying assumptions. However, with the rapid progress in computer capabilities, the technique known as the Computational Fluid Dynamics (CFD), which refers to the use of computers for numerically solving the nonlinear equations governing the fluid motion, has gained popularity in the recent years and revolutionised the way aerodynamic and internal flow solutions are obtained.

The pioneering work in this field employed hand computations to demonstrate that nonlinear equations of fluid motion can be solved numerically. However, these studies did not affect aerospace research and has not found practical application until the mid 1970s. However, rapid improvements in computer hardware, resulting in increased memory and speed, have made it possible to solve equations in fluid mechanics using various numerical techniques.

CFD is classified as a critical technology that will become a design tool, much like the wind tunnel, to increase the performance and effectiveness of aircraft, missiles, and hypersonic vehicles [1]. CFD will help to lower design risks, accelerate development and lower costs of all future flight vehicles that currently cannot be tested in restrictive flight regimes. CFD will be used to rapidly identify promising design concepts before wind tunnel tests are conducted, thereby significantly reducing system development time.

The basic formulations of fluid mechanics, known as the Navier Stokes equations were first derived in 1827. Before Navier and Stokes, the Swiss scientist Leonhard Euler had derived in 1775 a set of equations valid for a fluid assumed to be inviscid and non-heat conducting. These equations are known as the Euler equations.

Flow with high Reynolds numbers are essentially dominated by convective effects and can be approximated by Euler equations which incorporate major elements of fluid dynamics, such as shock waves and contact discontinuities. Since many flow situations encountered in industry and nature have high Reynolds numbers Euler equations are of high interest.

The history of numerical techniques for the solution of Euler equations goes back to early 1950's. Since these early days many schemes have been developed, such as space-centred schemes, upwind schemes, etc.

The common point of upwind schemes is the relation established between the characteristic propagation properties and the differencing such as to apply directional space discretizations in accordance with the physical behaviour of wave propagation.

Practically all schemes of Euler equations behave in a satisfactory way for smooth flows without strong gradients, but they can have very different behaviours in the presence of shock waves, for instance. Most of the schemes solve for the conservative Euler equations and capture the shocks automatically. However, they generate oscillations around shock discontinuities. Various methods had to be developed to control or limit these oscillations, such as introduction of artificial viscosity.

To allow high resolution of discontinuities, such as shock waves and contact discontinuities without oscillations, special upwind schemes were developed, which introduce information from the exact solutions of the Euler equations in the numerical discretization. This technique is known as shock fitting.

Shock fitting makes special treatment for explicitly computing the discontinuities. Discontinuities are located and treated as boundaries between regions where a regular solution is valid. For this approach the equations need not be in conservative form.

The present method falls into the shock fitting category, and uses the quasi-one dimensional formulation of the Euler equations.

The quasi-one-dimensional formulation of the Euler equations was first described in 1984 [2]. Verhoff used natural streamline coordinates and Riemann variables modified to include entropy in their definition. Even though conservative variables were not used highly accurate solutions were obtained. Shock waves were automatically captured but a one-point shock correction operator had to be employed after each solution iteration to maintain complete conservation across the shock. Single and dual diaphragm shock tube problems were solved to show the code's transient solution capability. The flow in a two-dimensional rectangular inlet at angle of attack was calculated for an inlet Mach number of 2 using first-order numerical methods. Results for a non-lifting NACA 0012 airfoil had been obtained for free stream Mach numbers of 0.72, 0.80, 0.90 and 1.20. Shock waves were located within one grid interval. Laminar Couette flow was solved including the viscous effects as additional source terms.

The formulation was employed to solve the flow properties in wave rotor applications [14, 15]. Time accurate solutions were obtained, where shocks and contact discontinuities were tracked and corrected explicitly.

The formulation was shown to be suitable to supersonic/hypersonic analysis of flow fields with predominantly oblique shocks [3]. For situations encountered in supersonic/hypersonic flows where shock waves are oblique and attached, the assumption of isentropic shocks were shown to yield results which are qualitatively correct and reasonably accurate.

A spatial marching technique was developed to numerically solve the Euler equations for supersonic and hypersonic flow [4, 5 and 6]. A computer program called SCRAM (Streamline Coordinate Riemann Axial Marching) has been developed based on the QAZ1D formulation. For fully supersonic inviscid flow, 3D flow field analysis was reduced to sequence of 2D problems by using a spatial marching solution procedure. The method was validated by comparison with analytic cone solutions and test data for several realistic wing/body configurations. Real gas results were presented for a

cone along with a demonstration that the procedure can be extended to incorporate parabolised viscous terms.

The normal derivatives in the source terms were decomposed and approximated with one-sided differences determined by the local direction of wave propagation [7]. Previously these terms were approximated by central differences which caused excessively slow convergence. The flow over AGARD ONERA M6 wing was computed for subcritical and transonic free stream velocities.

A method was developed for channel and cascade flows based on the linearized solutions of the full system of Euler equations, in order to correct the uniform boundary conditions, strictly valid at infinity, for the finite distance of the limits of the computational domain [8, 9]. The linearized solutions were obtained by separation of variables along the inlet and exit stations and an exponential variation in the axial direction. The Fourier coefficients obtained from this expression were used to generate the non-uniform corrections on the physical boundary conditions. The procedure is stated to allow computational boundaries to be located extremely close to the nonlinear region of interest.

In [10, 11] far field computational boundary conditions for 2D inviscid external flow problems were developed from analytical solutions of the steady state Euler equations. Computational efficiency gains were shown to be substantial. In [12] a similar study was reported for 2D inviscid duct flow problems.

In this thesis it was aimed to develop a computational method for the solution of Euler equations. The method was required to be accurate, fast and physical. The method was developed to solve unsteady inviscid 3D internal flow. Solution of unsteady equations of motion was achieved by the method of characteristics. Codes were developed to solve 1D, 2D and 3D flow problems. 2D and 3D flow problems were treated very similar to 1D problems.

The chapters are organised as follows: The second chapter includes the governing equations. The third chapter explains the solution algorithm and the fourth chapter deals with the boundary condition procedures. Solution of various test cases are given in Chapter 5 and the results are discussed. Chapter 6 summarises the study and recommendations for the future work.

CHAPTER 2

GOVERNING EQUATIONS

The present study deals with the equations of motion describing the flow of an inviscid compressible ideal gas with respect to a stationary reference frame. Governing equations are presented in the following sections.

2.1. EULER EQUATIONS

The Euler equations [2], describing the three-dimensional unsteady flow of an inviscid, adiabatic compressible fluid, expressed in natural streamline coordinate system (s, m, n) are

$$Q_t + (q + a) Q_s = -\frac{\gamma-1}{2} a \left(S - \frac{2}{\gamma-1}\right) \frac{\partial}{\partial s} \left(q - \frac{2}{\gamma-1} a\right) - \frac{\gamma-1}{2} q a S (\theta_n + \phi_m \cos\theta) \quad (2.1)$$

$$R_t + (q - a) R_s = +\frac{\gamma-1}{2} a \left(S - \frac{2}{\gamma-1}\right) \frac{\partial}{\partial s} \left(q + \frac{2}{\gamma-1} a\right) + \frac{\gamma-1}{2} q a S (\theta_n + \phi_m \cos\theta) \quad (2.2)$$

$$S_t + q S_s = 0 \quad (2.3)$$

$$\theta_t + q \theta_s = -\frac{a^2}{\gamma q} P_n \quad (2.4)$$

$$\phi_t + q \phi_s = -\frac{a^2}{\gamma q \cos\theta} P_m \quad (2.5)$$

where, velocity magnitude and speed of sound are denoted by q and a , respectively, and P is the logarithm of pressure. The extended Riemann variables Q and R are defined as

$$Q \equiv q + a S \quad (2.6)$$

$$R \equiv q - a S \quad (2.7)$$

while the modified entropy is defined in terms of pressure p and density ρ as

$$S \equiv \frac{1}{\gamma(\gamma-1)} \left[2\gamma - \ln\left(\frac{p}{\rho^\gamma}\right) \right] \quad (2.8)$$

The flow angles θ and ϕ and the streamline coordinate system are defined in Figure 2.1. Time is denoted by t while distances along and normal to the streamline direction are denoted by the vectors s , m and n , respectively. The n direction lies in the plane defined by the y -axis and the angle ϕ ; the m direction is normal to this plane. Partial differentiation is denoted by t , s , m or n subscripting.

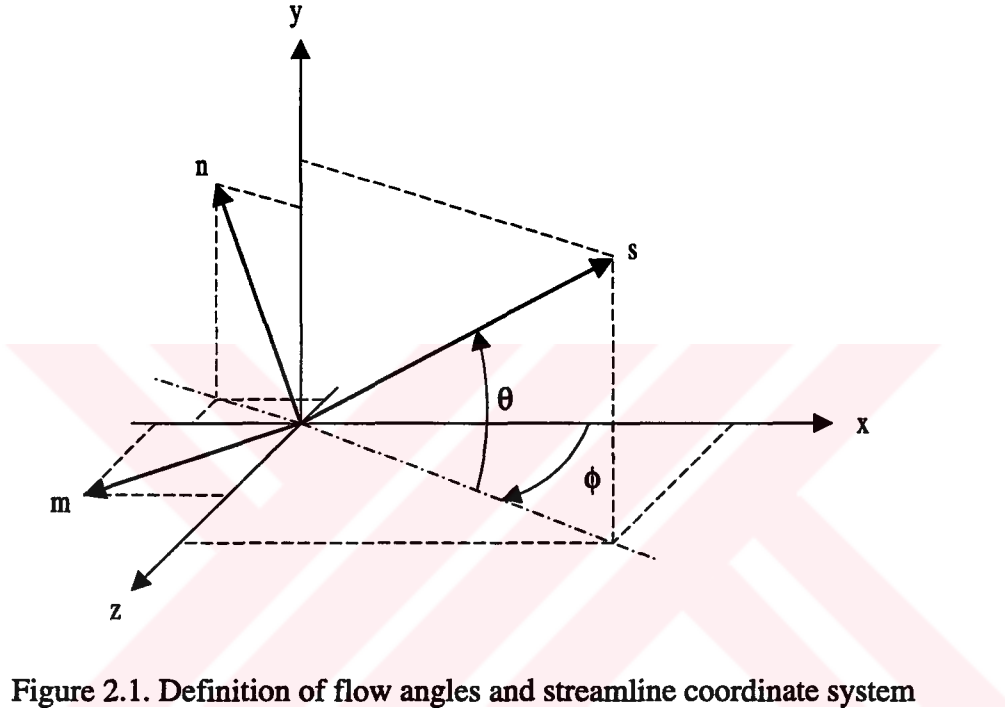


Figure 2.1. Definition of flow angles and streamline coordinate system

The equations for 1D, quasi 1D and 2D flows expressed in the streamline coordinate system are given in Appendix A.

Following the procedure for flux vector splitting [7] (See Appendix B) to distinguish directions of propagation normal to the local streamline direction, the system of equations (2.1) to (2.5) for the 3D isentropic flow becomes,

$$Q_t + (q+a) Q_s = -\frac{a}{4} \left[\frac{\partial}{\partial n} (Q-R)^+ - \frac{\partial}{\partial n} (Q-R)^- + \frac{\partial}{\partial m} (Q-R)^+ - \frac{\partial}{\partial m} (Q-R)^- \right] - \frac{q a}{2} \left[\left(\frac{\partial \theta^+}{\partial n} + \frac{\partial \theta^-}{\partial n} \right) + \cos \theta \left(\frac{\partial \phi^+}{\partial m} + \frac{\partial \phi^-}{\partial m} \right) \right] \quad (2.9)$$

$$R_t + (q-a) R_s = \frac{a}{4} \left[\frac{\partial}{\partial n} (Q-R)^+ - \frac{\partial}{\partial n} (Q-R)^- + \frac{\partial}{\partial m} (Q-R)^+ - \frac{\partial}{\partial m} (Q-R)^- \right] + \frac{q a}{2} \left[\left(\frac{\partial \theta^+}{\partial n} + \frac{\partial \theta^-}{\partial n} \right) + \cos \theta \left(\frac{\partial \phi^+}{\partial m} + \frac{\partial \phi^-}{\partial m} \right) \right] \quad (2.10)$$

$$\theta_t + q \theta_s = -\frac{a}{4q} \left[\frac{\partial}{\partial n} (Q-R)^+ + \frac{\partial}{\partial n} (Q-R)^- \right] - \frac{a}{2} \left(\frac{\partial \theta^+}{\partial n} - \frac{\partial \theta^-}{\partial n} \right) \quad (2.11)$$

$$\phi_t + q \phi_s = -\frac{a}{4q \cos \theta} \left[\frac{\partial}{\partial m} (Q-R)^+ + \frac{\partial}{\partial m} (Q-R)^- \right] - \frac{a}{2} \left(\frac{\partial \phi^+}{\partial m} - \frac{\partial \phi^-}{\partial m} \right) \quad (2.12)$$

where, $\frac{\partial}{\partial n} ()^+$ and $\frac{\partial}{\partial n} ()^-$ are one sided-derivatives along n , corresponding to the positive and negative eigen values normal to the streamline direction, respectively.

Along m , $\frac{\partial}{\partial m} ()^+$ and $\frac{\partial}{\partial m} ()^-$ derivatives have similar meaning.

The splitting of the matrices allows numerical differencing normal to the streamline direction in a manner consistent with the physical direction of wave propagation.

2.2. NON-DIMENSIONALIZATION

Far field conditions are chosen as the reference condition and the flow variables are non-dimensionalized as follows

$$q = \frac{q'}{a_{\text{ref}}} \quad (2.13)$$

$$a = \frac{a'}{a_{\text{ref}}} \quad (2.14)$$

$$p = \frac{p'}{p_{\text{ref}}} \quad (2.15)$$

$$\rho = \frac{\rho'}{\rho_{\text{ref}}} \quad (2.16)$$

$$S = \frac{S'}{R} \quad (2.17)$$

where a_{ref} , p_{ref} , ρ_{ref} are the free stream values of speed of sound, pressure, density respectively and R is the gas constant.

CHAPTER 3

SOLUTION ALGORITHM

In this chapter the solution algorithm developed for the solution of Euler equations expressed in the natural streamline coordinate system will be presented.

3.1. METHOD OF CHARACTERISTICS

The Euler equations governing the motion of an inviscid, adiabatic gas have a different character in different flow regimes. The unsteady equations are hyperbolic for both subsonic and supersonic flows. If the time dependent terms are eliminated, the resulting steady equations are elliptic when flow is subsonic and hyperbolic when the flow is supersonic.

Since closed form solutions of nonlinear hyperbolic partial differential equations do not exist, numerical methods have to be used to obtain solutions to such equations. The method of characteristics (MOC) is the oldest and most accurate numerical technique for solving hyperbolic partial differential equations.

The basis of the method of characteristics is the replacement of the original partial differential equations by the equivalent system of ordinary differential equations (compatibility equations) along special trajectories called characteristic curves.

The characteristic curve is the path of propagation of a physical disturbance. Across the characteristic curve the derivatives of a physical property may or may not be continuous, while the property itself remains continuous.

The MOC is applicable only to quasi-linear hyperbolic partial differential equations. A quasi-linear PDE of the 1st order is defined as one that is nonlinear in dependent variables, but linear in the first partial derivatives of the dependent variables.

In the present study the MOC is used and the solution method will be described in the following sections.

3.2. SOLUTION METHOD

Each equation in the system (Equation 2.9 to 2.12) has the general form,

$$\frac{\partial w}{\partial t} + \lambda \frac{\partial w}{\partial s} = z \quad (3.1)$$

where

$$\lambda = \begin{bmatrix} q+a & 0 & 0 & 0 & 0 \\ 0 & q-a & 0 & 0 & 0 \\ 0 & 0 & q & 0 & 0 \\ 0 & 0 & 0 & q & 0 \\ 0 & 0 & 0 & 0 & q \end{bmatrix} \quad (3.2)$$

$$w = \begin{Bmatrix} Q \\ R \\ S \\ \theta \\ \phi \end{Bmatrix} \quad (3.3)$$

$$z = \begin{bmatrix} -\frac{a}{4}[(Q-R)_n^+ - (Q-R)_n^- + (Q-R)_m^+ - (Q-R)_m^-] - \frac{qa}{2}[(\theta_n^+ + \theta_n^-) + \cos\theta(\phi_m^+ + \phi_m^-)] \\ \frac{a}{4}[(Q-R)_n^+ - (Q-R)_n^- + (Q-R)_m^+ - (Q-R)_m^-] + \frac{qa}{2}[(\theta_n^+ + \theta_n^-) + \cos\theta(\phi_m^+ + \phi_m^-)] \\ 0 \\ -\frac{a}{4q}[(Q-R)_n^+ + (Q-R)_n^-] - \frac{a}{2}[\theta_n^+ - \theta_n^-] \\ -\frac{a}{4q \cos\theta}[(Q-R)_m^+ + (Q-R)_m^-] - \frac{a}{2}[\phi_m^+ - \phi_m^-] \end{bmatrix} \quad (3.4)$$

In the s-t plane, along the trajectories with slopes,

$$\frac{ds}{dt} = \lambda \quad \lambda = q \pm a, q \quad (3.5)$$

the system of partial differential equations reduce to a system of ordinary differential equations,

$$\frac{dw}{dt} = z \quad (3.6)$$

where Equation 3.5 is called the “Characteristic Equation” and Equation 3.6 is called the “Compatibility Equation”.

The compatibility equations are,

$$\frac{dQ}{dt} = z_1 \quad \text{along} \quad \frac{ds}{dt} = q + a \quad (3.7)$$

$$\frac{dR}{dt} = z_2 \quad \text{along} \quad \frac{ds}{dt} = q - a \quad (3.8)$$

$$\frac{dS}{dt} = z_3 \quad \text{along} \quad \frac{ds}{dt} = q \quad (3.9)$$

$$\frac{d\theta}{dt} = z_4 \quad \text{along} \quad \frac{ds}{dt} = q \quad (3.10)$$

$$\frac{d\phi}{dt} = z_5 \quad \text{along} \quad \frac{ds}{dt} = q \quad (3.11)$$

where

$$z_1 = -\frac{a}{4}[(Q-R)_n^+ - (Q-R)_n^- + (Q-R)_m^+ - (Q-R)_m^-] - \frac{qa}{2}[(\theta_n^+ + \theta_n^-) + \cos\theta(\phi_m^+ + \phi_m^-)] \quad (3.12)$$

$$z_2 = \frac{a}{4}[(Q-R)_n^+ - (Q-R)_n^- + (Q-R)_m^+ - (Q-R)_m^-] + \frac{qa}{2}[(\theta_n^+ + \theta_n^-) + \cos\theta(\phi_m^+ + \phi_m^-)] \quad (3.13)$$

$$z_3 = 0 \quad (3.14)$$

$$z_4 = -\frac{a}{4q}[(Q-R)_n^+ + (Q-R)_n^-] - \frac{a}{2}[\theta_n^+ - \theta_n^-] \quad (3.15)$$

$$z_5 = -\frac{a}{4q \cos\theta}[(Q-R)_m^+ + (Q-R)_m^-] - \frac{a}{2}[\phi_m^+ - \phi_m^-] \quad (3.16)$$

Using an inverse marching procedure, these ordinary differential equations are integrated along the characteristic trajectories to calculate the flow variables (Q , R , S , θ and ϕ) at the next time level.

3.3. INVERSE MARCHING PROCEDURE

Since the equations governing the unsteady quasi-one-dimensional flow are hyperbolic, they must be integrated by a marching type numerical method. In the present study inverse marching procedure was used and it will be described below.

Figure 3.1 illustrates schematically the finite difference grid, in the s - t plane, based on the inverse marching method. In this method the location of the solution points are specified a priori. The three characteristics intersecting at the solution point are extended rearward to intersect a line on which initial data points from previous calculations are located. The flow properties at initial data points are calculated using the flow properties and their spatial derivatives at point "i".

To ensure that the solution is stable, the Courant-Friedrichs-Lewy (CFL) stability criterion must be specified. The criterion requires that the initial data points (such as points 1, 2 and 3 in Figure 3.1) fall between the previous solution points (such as points $i-1$, i and $i+1$).

The characteristic trajectories are shown on the s - t plane in Figure 3.1.

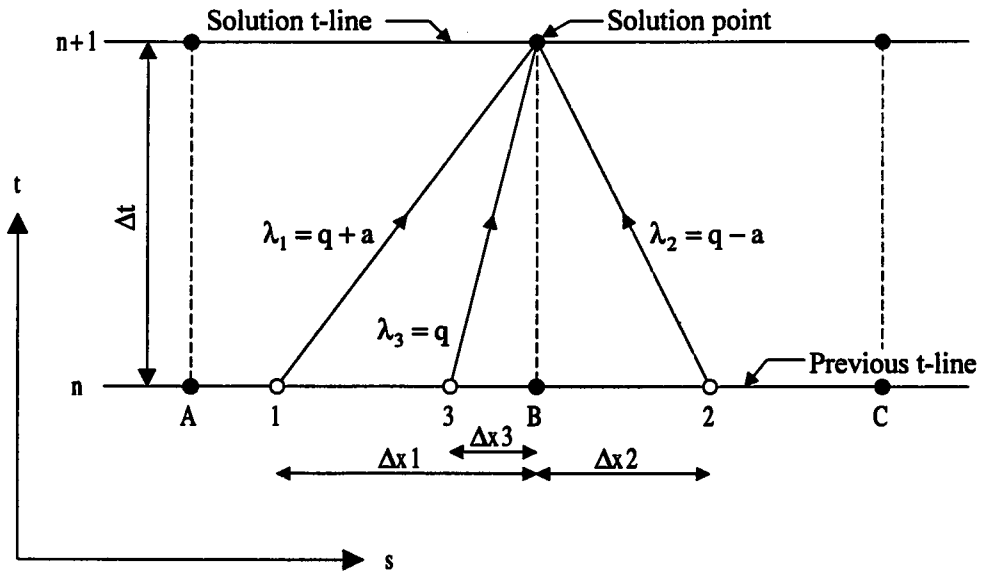


Figure 3.1. Characteristic trajectories in the space-time domain (1D)

For two dimensional and three dimensional flows, inverse marching procedure is handled in a similar fashion. This time the three characteristics intersecting at a solution point are extended rearward to intersect on the streamline which passes through the same point in the previous t-plane (or t-volume in 3D). The flow properties at initial data points 1, 2 and 3 are calculated using the flow properties and their spatial derivatives at point (i,j) (point (i,j,k) in 3D). Figure 3.2 illustrates the overall marching algorithm based on the grid for the inverse marching method shown in Figure 3.1.

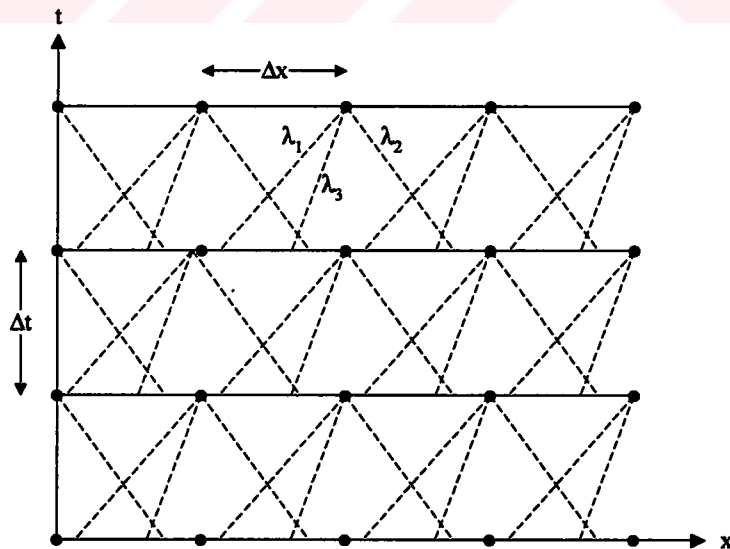


Figure 3.2. Marching algorithm for the inverse marching method

For two and three dimensional flows the characteristic trajectories in space-time domain are shown in Figure 3.3 and Figure 3.4, respectively.

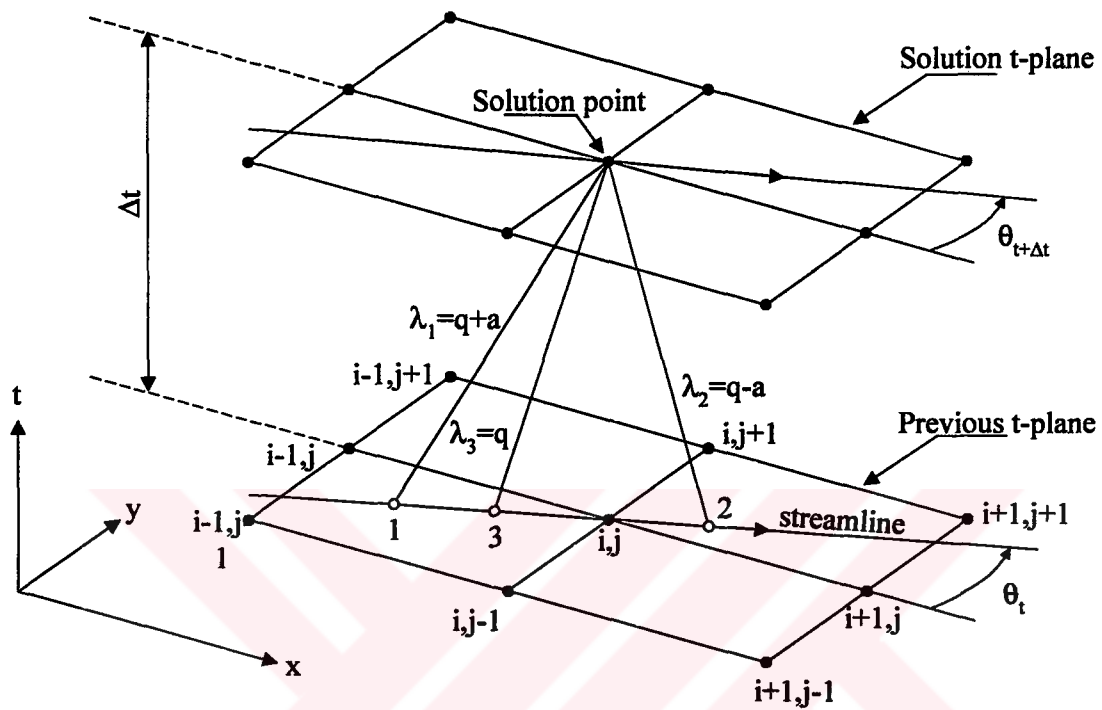


Figure 3.3. Characteristic trajectories in the space-time domain (2D)

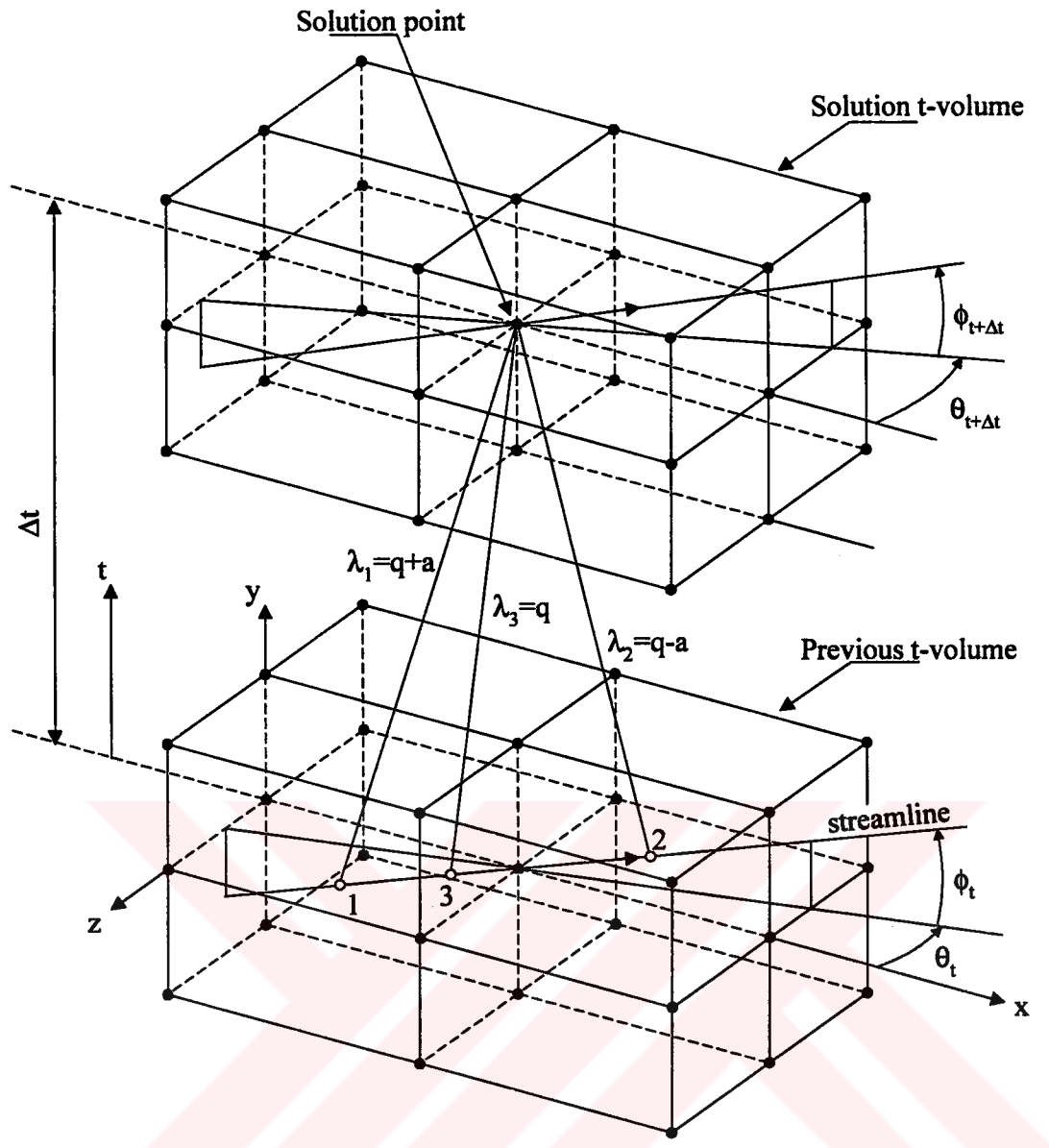


Figure 3.4. Characteristic trajectories in the space-time domain (3D)

The discussion given in the following sections of this study is based on 3D flow assumption.

The time derivatives in Equation 3.7 to Equation 3.11 are approximated by first order forward finite differences as,

$$\left. \frac{dQ}{dt} \right)_{1,n} = \frac{Q_i^{n+1} - Q_i^n}{\Delta t} + O(\Delta t) \quad (3.17)$$

$$\left. \frac{dR}{dt} \right)_{2,n} = \frac{R_i^{n+1} - R_2^n}{\Delta t} + O(\Delta t) \quad (3.18)$$

$$\left. \frac{dS}{dt} \right)_{3,n} = \frac{S_i^{n+1} - S_3^n}{\Delta t} + O(\Delta t) \quad (3.19)$$

$$\left. \frac{d\theta}{dt} \right)_{3,n} = \frac{\theta_i^{n+1} - \theta_3^n}{\Delta t} + O(\Delta t) \quad (3.20)$$

$$\left. \frac{d\phi}{dt} \right)_{3,n} = \frac{\phi_i^{n+1} - \phi_3^n}{\Delta t} + O(\Delta t) \quad (3.21)$$

Substituting these approximations in the above equation

$$Q_i^{n+1} = Q_1^n + z_1 \Delta t \quad (3.22)$$

$$R_i^{n+1} = R_2^n + z_2 \Delta t \quad (3.23)$$

$$S_i^{n+1} = S_3^n + z_3 \Delta t \quad (3.24)$$

$$\theta_i^{n+1} = \theta_3^n + z_4 \Delta t \quad (3.25)$$

$$\phi_i^{n+1} = \phi_3^n + z_5 \Delta t \quad (3.26)$$

The source terms z_1 , z_2 , z_3 , z_4 and z_5 are evaluated using the flow parameters at points 1, 2, 3, 3 and 3 respectively.

The flow parameters w (i.e. Q , R , S , θ and ϕ) at points 1, 2 and 3 are calculated using:

$$w_1 = w_i^n - (\Delta x_1) \left(\frac{\partial w}{\partial s} \right)_1 \quad (3.27)$$

$$w_2 = w_i^n - (\Delta x_2) \left(\frac{\partial w}{\partial s} \right)_2 \quad (3.28)$$

$$w_3 = w_i^n - (\Delta x_3) \left(\frac{\partial w}{\partial s} \right)_3 \quad (3.29)$$

where,

$$\Delta x_1 = \lambda_1 \Delta t \quad (3.30)$$

$$\Delta x_2 = \lambda_2 \Delta t \quad (3.31)$$

$$\Delta x_3 = \lambda_3 \Delta t \quad (3.32)$$

The dependent variables q and a at points 1, 2 and 3 are calculated using

$$q_1 = 0.5 (Q_1 + R_1) \quad (3.33)$$

$$q_2 = 0.5 (Q_2 + R_2) \quad (3.34)$$

$$q_3 = 0.5 (Q_3 + R_3) \quad (3.35)$$

$$a_1 = 0.5 (Q_1 - R_1) / S_1 \quad (3.36)$$

$$a_2 = 0.5 (Q_2 - R_2) / S_2 \quad (3.37)$$

$$a_3 = 0.5 (Q_3 - R_3) / S_3 \quad (3.38)$$

Streamwise spatial derivative, $\frac{\partial w}{\partial s}$, and the derivatives normal to the streamline direction, $\frac{\partial w}{\partial n}$ and $\frac{\partial w}{\partial m}$, are discretized with one sided differences in a manner consistent with the physical direction of wave propagation.

If the flow is supersonic, s derivatives of all the flow variables are calculated using backward differencing. However, if the flow is subsonic, $\frac{\partial R}{\partial s}$ should be calculated using forward differencing, where the rest of the s derivatives should be calculated using backward differencing. $\frac{\partial w^+}{\partial n}$ and $\frac{\partial w^+}{\partial m}$ derivatives are calculated using forward differencing, where $\frac{\partial w^-}{\partial n}$ and $\frac{\partial w^-}{\partial m}$ derivatives are calculated using backward differencing.

For a 2D flow, the computational cells used in the calculation of the $\frac{\partial w}{\partial s}$ and $\frac{\partial w}{\partial n}$ derivatives are shown in Table 3.1.

Table 3.1. Computational cells used in calculating s and n derivatives

	$\frac{\partial w}{\partial s}$	$\frac{\partial w}{\partial n}$
F O R W A R D		
B A C K W A R D		

The time step, Δt , is determined using the CFL condition which requires the domain of dependence of the numerical approximation to include the domain of dependence of the differential equations. The maximum time step is calculated using,

$$\max(\Delta t) = \text{CFL} \frac{\max(\Delta x)}{\min|q + a|} \quad (3.39)$$

The time step, Δt , can be calculated either for each individual node, or for the entire computational domain. The former method is called the “local maximum time stepping” where the latter is called the “global maximum time stepping”. If local maximum time stepping is used the solution is not time accurate, but convergence to steady state is faster.

Once Δt is known, the locations of the initial data points 1, 2 and 3 are calculated using an iterative procedure. Initially, the slopes of the characteristic lines are predicted using,

$$\lambda_1^p = q_i^n + a_i^n \quad (3.40)$$

$$\lambda_2^p = q_i^n - a_i^n \quad (3.41)$$

$$\lambda_3^p = q_i^n \quad (3.42)$$

Δx_1 , Δx_2 and Δx_3 are calculated using the predicted slopes as,

$$\Delta x_1 = \lambda_1^p \Delta t \quad (3.43)$$

$$\Delta x_2 = \lambda_2^p \Delta t \quad (3.44)$$

$$\Delta x_3 = \lambda_3^p \Delta t \quad (3.45)$$

The flow parameters at points 1, 2 and 3 are calculated using Equation 3.27 to Equation 3.29.

The corrected slopes of the characteristic lines are calculated using,

$$\lambda_1^c = q_1 + a_1 \quad (3.46)$$

$$\lambda_2^c = q_2 - a_2 \quad (3.47)$$

$$\lambda_3^c = q_3$$

(3.48)

At this point, λ^p and λ^c values are compared. If the slopes do not meet the convergence criteria, λ^c is assigned to λ^p , and the algorithm described above is repeated until the convergence criteria is met. The algorithm to calculate the values of the flow variables at initial data points 1, 2 and 3 is given in Figure 3.5

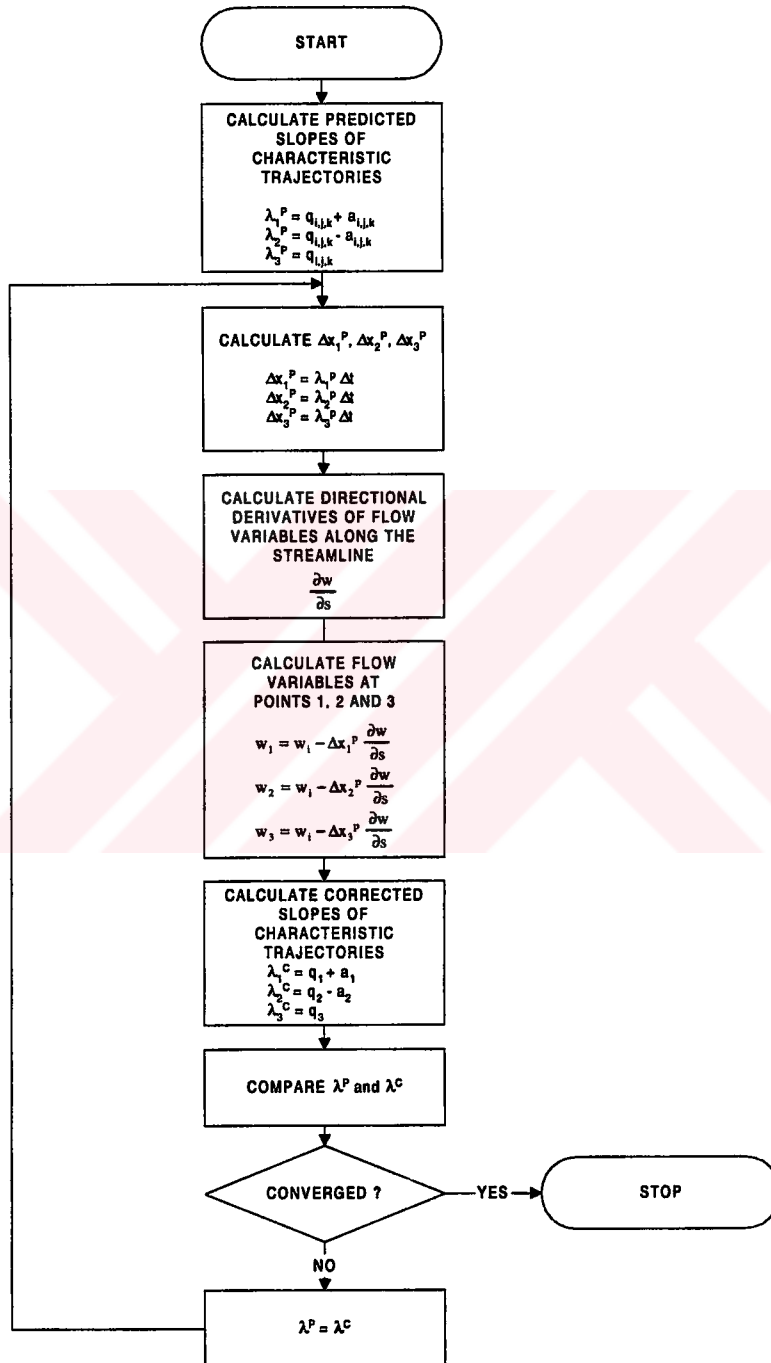


Figure 3.5. Inverse marching procedure

Once, the values flow variables at points 1, 2 and 3 are determined, the flow properties at the solution point are calculated using Equation 3.22 to Equation 3.26.

The derivative along the streamline, $\frac{\partial w}{\partial s}$, and the derivatives normal to the streamline

$\frac{\partial w}{\partial n}$ and $\frac{\partial w}{\partial m}$, are calculated using,

$$\frac{\partial w}{\partial s} = \bar{s} \cdot \nabla w \quad (3.49)$$

$$\frac{\partial w}{\partial n} = \bar{n} \cdot \nabla w \quad (3.50)$$

$$\frac{\partial w}{\partial m} = \bar{m} \cdot \nabla w \quad (3.51)$$

where

$$\nabla w = \frac{\partial w}{\partial x} \bar{i} + \frac{\partial w}{\partial y} \bar{j} + \frac{\partial w}{\partial z} \bar{k} \quad (3.52)$$

For the 3-dimensional flow $w = f(x, y, z)$, and using the chain rule we can write,

$$\frac{\partial w}{\partial x} = \frac{\partial w}{\partial \xi} \frac{\partial \xi}{\partial x} + \frac{\partial w}{\partial \eta} \frac{\partial \eta}{\partial x} + \frac{\partial w}{\partial \zeta} \frac{\partial \zeta}{\partial x} \quad (3.53)$$

$$\frac{\partial w}{\partial y} = \frac{\partial w}{\partial \xi} \frac{\partial \xi}{\partial y} + \frac{\partial w}{\partial \eta} \frac{\partial \eta}{\partial y} + \frac{\partial w}{\partial \zeta} \frac{\partial \zeta}{\partial y} \quad (3.54)$$

$$\frac{\partial w}{\partial z} = \frac{\partial w}{\partial \xi} \frac{\partial \xi}{\partial z} + \frac{\partial w}{\partial \eta} \frac{\partial \eta}{\partial z} + \frac{\partial w}{\partial \zeta} \frac{\partial \zeta}{\partial z} \quad (3.55)$$

where ξ , η and ζ are the coordinates in the computational domain.

The unit vector along the streamline is

$$\bar{s} = \cos(\theta) \cos(\phi) \bar{i} + \sin(\theta) \bar{j} + \cos(\theta) \sin(\phi) \bar{k} \quad (3.56)$$

and the unit vectors normal to the streamline are

$$\bar{n} = -\sin(\theta) \cos(\phi) \bar{i} + \cos(\theta) \bar{j} - \sin(\theta) \sin(\phi) \bar{k} \quad (3.57)$$

$$\bar{m} = -\sin(\phi) \bar{i} + \cos(\phi) \bar{k} \quad (3.58)$$

Substituting these in Equations 3.49 to 3.51,

$$\begin{aligned} \frac{\partial w}{\partial s} = & \left(\frac{\partial w}{\partial \xi} \frac{\partial \xi}{\partial x} + \frac{\partial w}{\partial \eta} \frac{\partial \eta}{\partial x} + \frac{\partial w}{\partial \zeta} \frac{\partial \zeta}{\partial x} \right) \cos(\theta) \cos(\phi) \\ & + \left(\frac{\partial w}{\partial \xi} \frac{\partial \xi}{\partial y} + \frac{\partial w}{\partial \eta} \frac{\partial \eta}{\partial y} + \frac{\partial w}{\partial \zeta} \frac{\partial \zeta}{\partial y} \right) \sin(\theta) \\ & + \left(\frac{\partial w}{\partial \xi} \frac{\partial \xi}{\partial z} + \frac{\partial w}{\partial \eta} \frac{\partial \eta}{\partial z} + \frac{\partial w}{\partial \zeta} \frac{\partial \zeta}{\partial z} \right) \cos(\theta) \sin(\phi) \end{aligned} \quad (3.59)$$

$$\begin{aligned} \frac{\partial w}{\partial n} = & - \left(\frac{\partial w}{\partial \xi} \frac{\partial \xi}{\partial x} + \frac{\partial w}{\partial \eta} \frac{\partial \eta}{\partial x} + \frac{\partial w}{\partial \zeta} \frac{\partial \zeta}{\partial x} \right) \sin(\theta) \cos(\phi) \\ & + \left(\frac{\partial w}{\partial \xi} \frac{\partial \xi}{\partial y} + \frac{\partial w}{\partial \eta} \frac{\partial \eta}{\partial y} + \frac{\partial w}{\partial \zeta} \frac{\partial \zeta}{\partial y} \right) \cos(\theta) \\ & - \left(\frac{\partial w}{\partial \xi} \frac{\partial \xi}{\partial z} + \frac{\partial w}{\partial \eta} \frac{\partial \eta}{\partial z} + \frac{\partial w}{\partial \zeta} \frac{\partial \zeta}{\partial z} \right) \sin(\theta) \sin(\phi) \end{aligned} \quad (3.60)$$

$$\begin{aligned} \frac{\partial w}{\partial m} = & - \left(\frac{\partial w}{\partial \xi} \frac{\partial \xi}{\partial x} + \frac{\partial w}{\partial \eta} \frac{\partial \eta}{\partial x} + \frac{\partial w}{\partial \zeta} \frac{\partial \zeta}{\partial x} \right) \sin(\phi) \\ & + \left(\frac{\partial w}{\partial \xi} \frac{\partial \xi}{\partial z} + \frac{\partial w}{\partial \eta} \frac{\partial \eta}{\partial z} + \frac{\partial w}{\partial \zeta} \frac{\partial \zeta}{\partial z} \right) \cos(\phi) \end{aligned} \quad (3.61)$$

The terms $\frac{\partial \xi}{\partial x}, \frac{\partial \eta}{\partial x}, \frac{\partial \zeta}{\partial x}, \frac{\partial \xi}{\partial y}, \frac{\partial \eta}{\partial y}, \frac{\partial \zeta}{\partial y}, \frac{\partial \xi}{\partial z}, \frac{\partial \eta}{\partial z}, \frac{\partial \zeta}{\partial z}$ are the metrics and are calculated numerically using,

$$\xi_x = J(y_\eta z_\zeta - y_\zeta z_\eta) \quad (3.62)$$

$$\xi_y = J(x_\zeta z_\eta - x_\eta z_\zeta) \quad (3.63)$$

$$\xi_z = J(x_\eta y_\zeta - x_\zeta y_\eta) \quad (3.64)$$

$$\eta_x = J(y_\zeta z_\xi - y_\xi z_\zeta) \quad (3.65)$$

$$\eta_y = J(x_\xi z_\zeta - x_\zeta z_\xi) \quad (3.66)$$

$$\eta_z = J(x_\zeta y_\xi - x_\xi y_\zeta) \quad (3.67)$$

$$\zeta_x = J(y_\xi z_\eta - y_\eta z_\xi) \quad (3.68)$$

$$\zeta_y = J(x_\eta z_\xi - x_\xi z_\eta) \quad (3.69)$$

$$\zeta_z = J(x_\xi y_\eta - x_\eta y_\xi) \quad (3.70)$$

where the Jacobian J is,

$$J = \frac{1}{x_\xi(y_\eta z_\zeta - y_\zeta z_\eta) - x_\eta(y_\xi z_\zeta - y_\zeta z_\xi) + x_\zeta(y_\xi z_\eta - y_\zeta z_\xi)} \quad (3.71)$$

Note that the formulation given above holds true if the computational grid is independent of time, and therefore time gradients of the metrics are zero.

The derivatives $x_\xi, x_\eta, x_\zeta, y_\xi, y_\eta, y_\zeta, z_\xi, z_\eta, z_\zeta$ are calculated using 2nd order central differences.

$$x_\xi = 0.5 (x_{i+1,j,k} - x_{i-1,j,k}) \quad (3.72)$$

$$x_\eta = 0.5 (x_{i,j+1,k} - x_{i,j-1,k}) \quad (3.73)$$

$$x_\zeta = 0.5 (x_{i,j,k+1} - x_{i,j,k-1}) \quad (3.74)$$

$$y_\xi = 0.5 (y_{i+1,j,k} - y_{i-1,j,k}) \quad (3.75)$$

$$y_\eta = 0.5 (y_{i,j+1,k} - y_{i,j-1,k}) \quad (3.76)$$

$$y_\zeta = 0.5 (y_{i,j,k+1} - y_{i,j,k-1}) \quad (3.77)$$

$$z_\xi = 0.5 (z_{i+1,j,k} - z_{i-1,j,k}) \quad (3.78)$$

$$z_\eta = 0.5 (z_{i,j+1,k} - z_{i,j-1,k}) \quad (3.79)$$

$$z_\zeta = 0.5 (z_{i,j,k+1} - z_{i,j,k-1}) \quad (3.80)$$

The other derivatives that must be evaluated for calculating the streamwise and

normal derivatives are $\frac{\partial w}{\partial \xi}$, $\frac{\partial w}{\partial \eta}$ and $\frac{\partial w}{\partial \zeta}$.

The differencing algorithm employed in the evaluation of these derivatives depend upon the variable "w" and the flow regime.

The cell to be used in differencing is selected according to the direction of signal propagation and the alignment of the local velocity vector with the computational grid. Finite difference equations used in the computation of $\frac{\partial w}{\partial \xi}$, $\frac{\partial w}{\partial \eta}$ and $\frac{\partial w}{\partial \zeta}$ derivatives are tabulated in Appendix C.

3.4. SHOCK CORRECTION

Since Equation 3.1 is not valid across discontinuities a special additional treatment is required in the numerical procedure to model flows which contain discontinuities. Although the numerical solution procedure described in Section 3.2 can be applied to a grid cell containing a shock wave, and the shock can be captured within one cell, the shock discontinuity which is not formally accounted for produces conservation error. This results in an incorrect shock position and error in the jump conditions across the shock. After each iteration application of a simple shock correction based on mass, momentum and energy conservation should be employed to eliminate the shock jump errors and force the shock wave to the correct location.

3.4.1. Shock Identification

To apply shock correction, the grid interval where the shock wave is starting to form must be identified. Initially shocks can be located simply by monitoring the sign of the characteristic velocity $q-a$. In the grid interval bracketing the shock the characteristic velocity $q-a$ changes its sign. At the upstream $q-a$ is greater than zero, where downstream of the shock $q-a$ is less than zero. No correction is made until the shock gains significant strength (e.g. upstream Mach number relative to the shock, $W > 1.1$). However, for problems where the flow is initiated by the rupture of a diaphragm which separates two regions with high pressure ratio, shock is assumed to be formed at the moment of the rupture and be spatially located at the location of the diaphragm.

3.4.2. Isentropic Shocks

A “hands off” shock procedure is obtained by ignoring the entropy equation in the quasi-one-dimensional formulation while assuming continuous Q and R across the shock. Since the equations for the extended Riemann variables Q and R are derived

only from the mass and momentum equations, this approximation is equivalent to disregarding energy conservation in favour of isentropic shocks with mass and momentum conservation. The result is a local total temperature decrease or “cooling” of the flow downstream of an isentropic shock [3].

3.4.3. Shock Jump Correction

The method used in the present work to correct shock jump errors is based on that of Moretti [16]. The method makes use of the analytical relationship between the change in the Riemann variables across a shock and the incoming Mach number relative to the shock wave. The relation is used to determine the shock speed and to transform the problem to a steady case which can be handled using normal shock relations.

Consider a shock wave propagating with velocity V_s into a gas with velocity q_B as shown in Figure 3.6.a. Let the conditions to the left of the shock be denoted by A subscript and conditions to the right by B subscript. Let the high pressure side is to the left. Viewed from a reference frame moving with the shock wave (Figure 3.6.b), the shock wave is a stationary one with an upstream velocity u_B and a downstream velocity u_A . Then the upstream Mach number relative to the shock wave is,

$$W = -\frac{u_B}{a_B} = -\frac{(q_B - V_s)}{a_B} \quad (3.81)$$

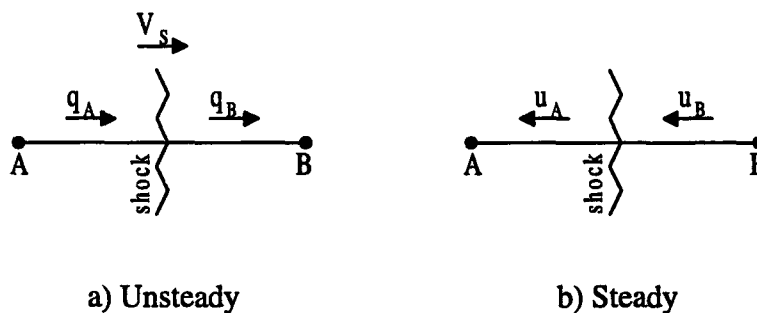


Figure 3.6. Shock wave with high pressure to the left

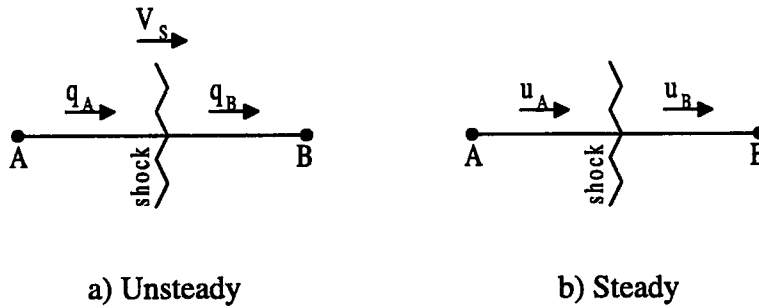


Figure 3.7. Shock wave with high pressure to the right

Using normal shock relations the jump in Riemann variable Q across the shock is shown to be a function of upstream Mach number W [14], such that

$$\frac{Q_A - Q_B}{a_B} = f(W) \tag{3.82}$$

It was also shown that [14] for upstream Mach numbers W in the range of 1.0 to 4.0, the exact relationship $f(W)$ can be approximated by a 2nd order polynomial (Figure 3.8), and Equation 3.82 becomes

$$\frac{Q_A - Q_B}{a_B} \approx -2.7574 + 3.1573 W - 0.2863 W^2 \tag{3.83}$$

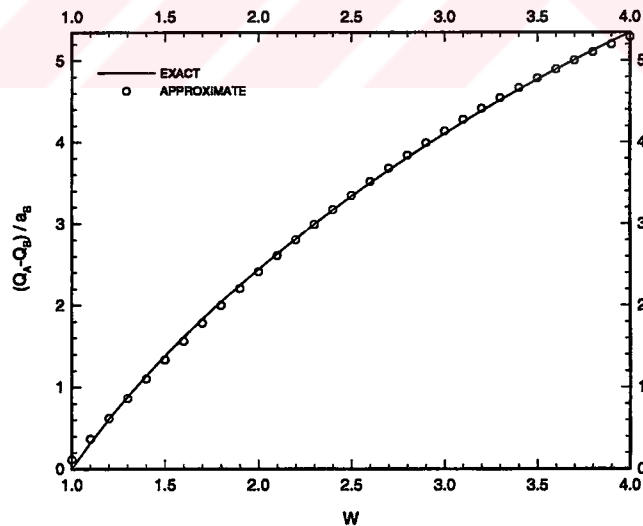


Figure 3.8. Riemann variable change across a shock wave

It should be noted that if the high pressure side were to the right, as in Figure 3.7, Equation 3.81 would become

$$W = \frac{u_A}{a_A} = \frac{q_A - V_s}{a_A} \quad (3.84)$$

and Equation 3.82 would become

$$\frac{R_A - R_B}{a_A} = f(W) \quad (3.85)$$

Once the grid interval housing a shock wave is identified, the change in Q is measured across an interval. This value, call it ΔQ_m is used in Equation 3.83 to get an approximation for the value of W . W is used in the exact function $f(W)$ to calculate the exact value of ΔQ , call it ΔQ_e . If the value of ΔQ is not equal to the value measured across the shock, a new value ΔQ is calculated according to

$$\Delta Q_{i+1} = \Delta Q_i + (\Delta Q_m - \Delta Q_e) \quad (3.86)$$

ΔQ_{i+1} is used in Equation 3.83 to obtain another value of W . The above procedure is repeated until the exact value of ΔQ calculated from Equation 3.82 equals the measured value of ΔQ . Then W is known to be correct and the normal shock relations can be used to calculate the values at node A. V_s can also be calculated from Equation 3.81 and used to track the shock during the next time level.

Shock jump correction procedure described above is summarised in Figure 3.9.

The equations governing the change of flow variables across the shock are given in Appendix D.

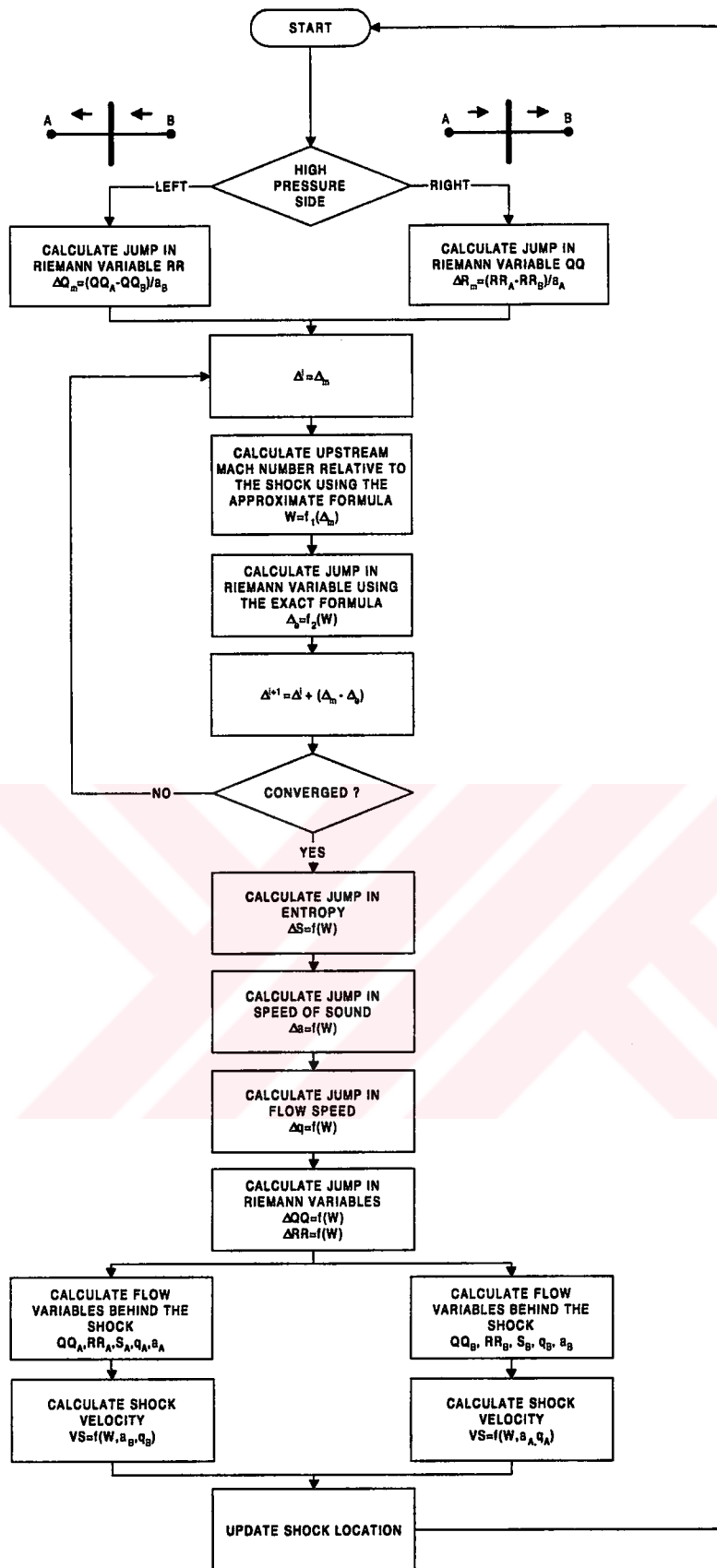


Figure 3.9. Shock jump correction procedure

3.4.4. Shocks in Multi-Dimensional Flows

The concept of shock correction described above is also applicable in problems involving two or three dimensional flows. Since the formulation is based on a quasi-one-dimensional flow, information about the orientation of the shock normal is necessary. Similar to that of Moretti [16] a shock parameter is defined as

$$\Sigma = \frac{Q_B^n - Q_A^n}{a_A} \quad (3.87)$$

where

$$Q_A^n = q_A^n + a_A S_A \quad (3.88)$$

and

$$Q_B^n = q_B^n + a_B S_B \quad (3.89)$$

where q_A^n and q_B^n are the velocity components normal to the shock on the low and high pressure sides, respectively (Figure 3.7).

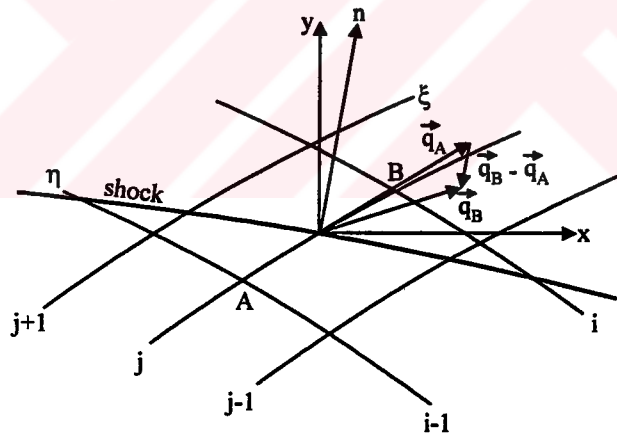


Figure 3.10. Shock on a two-dimensional grid

Substituting Equation 3.88 and 3.89 in 3.87

$$\Sigma = \frac{q_B^n - q_A^n}{a_A} + \frac{a_B}{a_A} S_B - S_A \quad (3.90)$$

Note that

$$q_B^n - q_A^n = -\bar{n} \cdot (\bar{q}_B - \bar{q}_A) \quad (3.91)$$

$$q_B^n - q_A^n = -n^x (q_B^x - q_A^x) - n^y (q_B^y - q_A^y) \quad (3.92)$$

where q_A^x , q_A^y , q_B^x , q_B^y are the velocity components in x and y directions on the low and high pressure sides of the shock and

$$q_A^x = q_A \cos(\theta_A) \quad (3.93)$$

$$q_B^x = q_B \cos(\theta_B) \quad (3.94)$$

$$q_A^y = q_A \sin(\theta_A) \quad (3.95)$$

$$q_B^y = q_B \sin(\theta_B) \quad (3.96)$$

The components of the unit vector normal to the shock wave in x and y directions are n^x and n^y , where

$$n^x = \frac{-(q_B^x - q_A^x)}{\sqrt{(q_B^x - q_A^x)^2 + (q_B^y - q_A^y)^2}} \quad (3.97)$$

$$n^y = \frac{-(q_B^y - q_A^y)}{\sqrt{(q_B^x - q_A^x)^2 + (q_B^y - q_A^y)^2}} \quad (3.98)$$

Substituting Equations 3.93 to 3.98 in Equation 3.92

$$q_B^n - q_A^n = \sqrt{(q_B^x - q_A^x)^2 + (q_B^y - q_A^y)^2} \quad (3.99)$$

Finally, substituting Equation 3.99 in Equation 3.90 gives

$$\Sigma = \sqrt{(q_B^x - q_A^x)^2 + (q_B^y - q_A^y)^2} + \frac{a_B}{a_A} S_B - S_A \quad (3.100)$$

The shock correction process is started by evaluating Σ for every possible pair of neighbouring grid points. If Σ as computed from Equation 3.100 exceeds some threshold, the interval is marked as having a shock fragment.

The velocity components normal to the shock wave are calculated using

$$q_A^n = -\vec{n} \cdot \vec{q}_A \quad (3.101)$$

and

$$q_B^n = -\vec{n} \cdot \vec{q}_B \quad (3.102)$$

Using the normal velocity components and the shock jump correction method described in Section 3.4.3, shock jump errors are eliminated.

3.5. PROGRAMMING

The program is coded in FORTRAN language. The flowchart of the program is given in Figure 3.11.

Initially, the input data file is read. Input data file contains the following information: name of the grid data file, name of the restart data file, CFL number, inflow and outflow boundary conditions, convergence criteria, etc.

If the start up is fresh one, then the flow variables (Q , R , S , θ and ϕ) are initialised at all nodes in the computational domain. Initial values of the variables are assigned by a linear interpolation between the inflow and outflow boundary conditions. Hence, they are physically incorrect.

If the program is restarted, the restart data file is read and flow variables are initialised based on the results of a previous run.

Following initialisation each node is assigned with a numerical tag which identifies node characteristics, such as whether the node is a normal inner node, or it is on a solid wall boundary, etc. Numerical node tags used for two and three-dimensional flow problems are given in Appendix E.

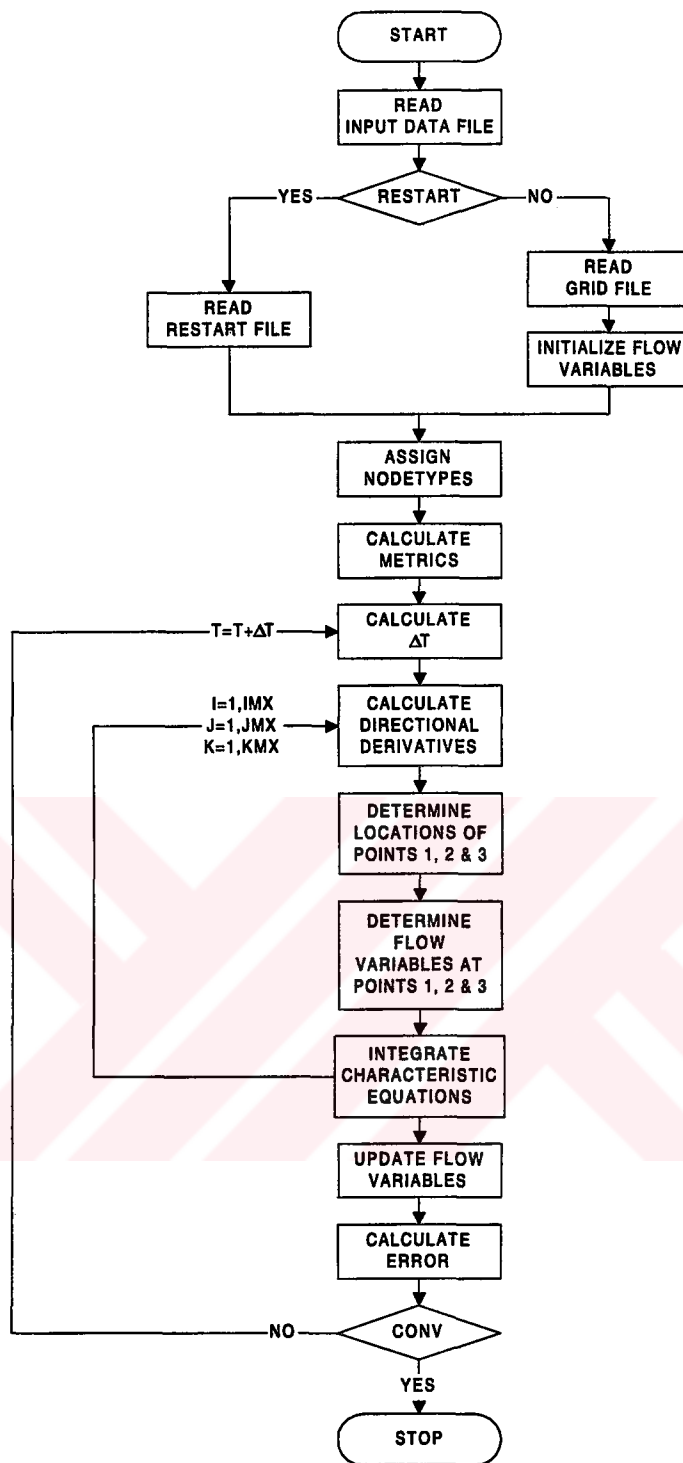


Figure 3.11. Program flowchart

The node tag is a one to four digit integer (eg. 1, 12, 222, 1001). "0" is used for a normal inner node. Primitive node tags and their meaning is given below:

Table 3.2. Primitive node tags

TAG	i, j, k	CHARACTER
1	i=1	Node on inflow boundary
2	i=imx	Node on outflow boundary
10	j=1	Node on solid wall boundary
20	j=jmx	Node on solid wall boundary
100	k=1	Node on periodic boundary
200	k=kmx	Node on periodic boundary
1000	k=1	Node on solid wall boundary
2000	k=kmx	Node on solid wall boundary

Other node tags are obtained by addition of primitive node tags. Examining the digits of any node tag the character of that node can be deduced. For example, node tag "121=100+20+1" indicates that the node is on the inflow surface (i=1) and it is on a solid wall (j=jmx) and also on periodic boundary (k=1).

After assigning the nodes tags, metrics ($\frac{\partial \xi}{\partial x}, \frac{\partial \eta}{\partial x}, \frac{\partial \zeta}{\partial x}$, etc.) are calculated using second order central finite differencing.

Afterwards time step Δt is calculated. If local maximum stepping used, a maximum allowable Δt is calculated for each individual node, ie. every node proceeds with different steps in time and solution is not time accurate. However, if global maximum time stepping used a common Δt is calculated for the entire computational domain, hence the solution at every node proceeds with a common time step and the solution is time accurate.

Directional derivatives of the flow variables ($\frac{\partial}{\partial s}, \frac{\partial}{\partial n}, \frac{\partial}{\partial m}$) are calculated considering the physical direction of wave propagation.

The flow variables at initial data points (1, 2 and 3) are calculated using the iterative procedure described in Section 3.3

Once the initial data points and the values of flow variables at these points are determined the characteristics equations are integrated along the characteristic trajectories to determine the values of flow variables at the next time step.

This procedure is repeated until convergence. The error term checked for convergence is determined by calculating the maximum change in pressure between two consecutive time levels. That is

$$\text{error} = \max \left| \frac{P_{i,j,k}^{n+1} - P_{i,j,k}^n}{P_{i,j,k}^n} \right| \quad \begin{array}{l} i=1 \rightarrow \text{imx} \\ j=1 \rightarrow \text{jmx} \\ k=1 \rightarrow \text{kmx} \end{array} \quad (3.103)$$

CHAPTER 4

BOUNDARY CONDITIONS

During the solutions of fluid dynamic equations, usually one or more artificial computational boundaries located at some distance from the primary region of interest are used in order to limit the physical domain to finite size. On such boundaries some type of boundary conditions must be imposed to simulate the influence of the true far field conditions.

In addition to far field boundaries, the physical domains are also bounded by surface boundaries (solid wall/porous wall), periodic boundaries or a combination of these. Hence, numerical solution procedures must handle such types of boundaries.

In this study, characteristic type boundary conditions are used. Characteristic trajectories are considered to transport information about certain parameters and boundary conditions are imposed based on the direction of these characteristic trajectories.

The number of physical variables that can be imposed freely at a boundary is dependent on the direction of information propagation. Only the variables whose direction of propagation is toward the computational domain can be imposed freely at the boundaries as physical boundary conditions. The remaining variables on the boundary depend on the information from interior of the computational domain. The values of these variables are specified as numerical boundary conditions based on the information from inside the computational domain.

Far field, solid wall and periodic type boundary conditions are explained in the following paragraphs.

4.1. FAR FIELD BOUNDARY CONDITIONS

Usually one or more artificial computational boundaries located at some distance from the primary region of interest are used to limit the physical domain to finite size. In this study, on the far field boundaries zeroth order far field boundary conditions are imposed to simulate the influence of the true far field conditions at infinity.

Zeroth order far field boundary conditions consist of imposing the constant value of the flow variables Q_∞ , R_∞ , S_∞ , θ_∞ or ϕ_∞ along the boundaries.

First order boundary conditions, on the other hand, consist of imposing distributions of flow variables Q_∞ , R_∞ , S_∞ , θ_∞ or ϕ_∞ along the boundaries. Second order boundary conditions provide high accuracy corrections to the first-order distributions [12].

If the boundary is sufficiently far removed, all three sets of boundary conditions produce essentially the same results within the computational domain.

The treatment of subsonic and supersonic, inflow and outflow boundaries are explained below.

4.1.1. Subsonic Inflow Boundary Condition

If the inflow velocity is subsonic (Figure 4.1),

$$\lambda_1 = q + a > 0$$

$$\lambda_2 = q - a < 0$$

$$\lambda_3 = q > 0$$

Hence, the characteristics with slopes λ_1 and λ_3 carry information from outside the computational domain. So, at the subsonic inflow boundary the values of the variables Q , S and the flow angles θ and ϕ are specified as the physical boundary conditions. The value of the remaining variable R at the boundary is determined with the information from the interior of the computational domain.

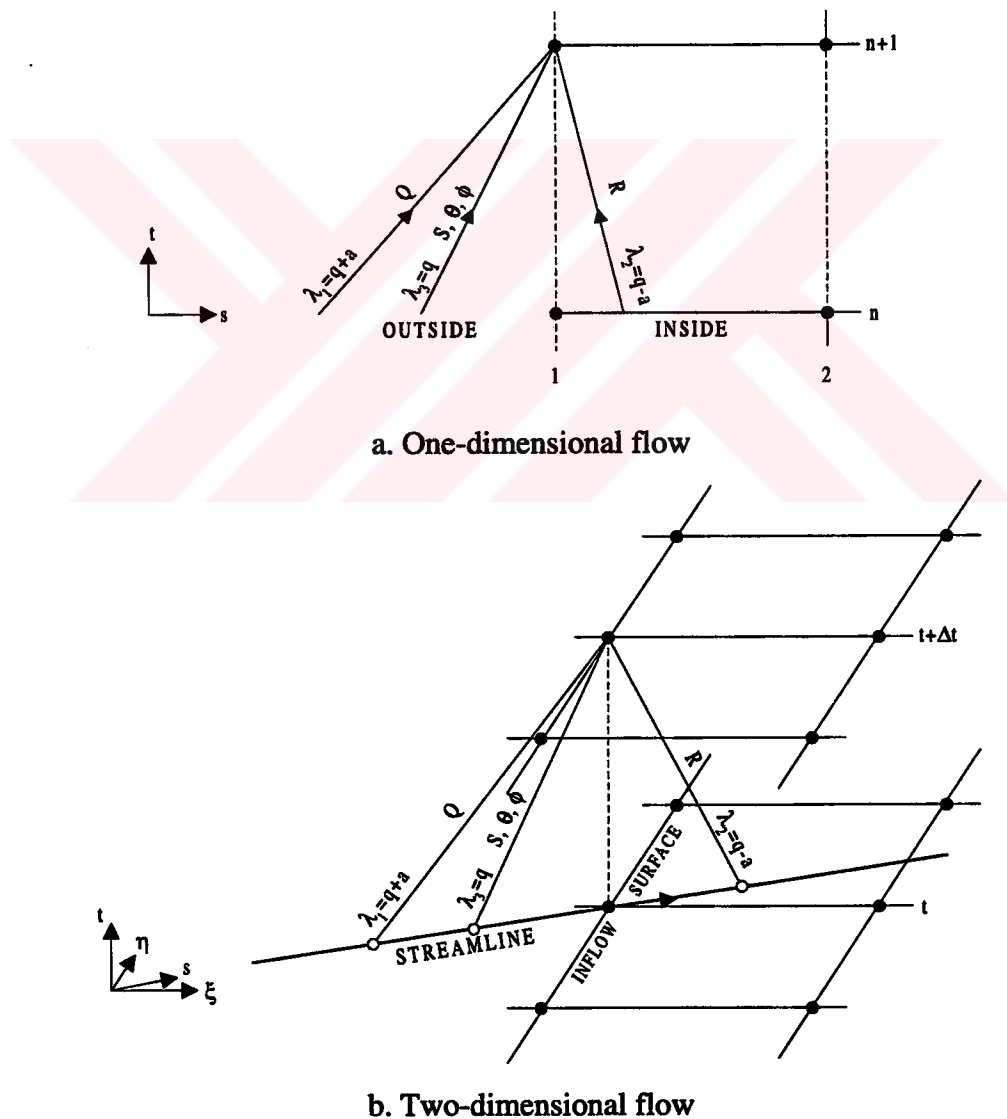


Figure 4.1. Subsonic inflow boundary

4.1.2. Supersonic Inflow Boundary Condition

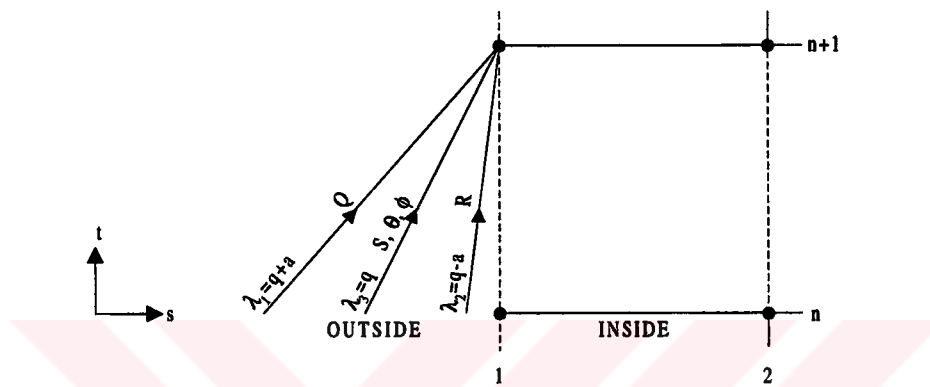
If the inflow velocity is supersonic (Figure 4.2),

$$\lambda_1 = q + a > 0$$

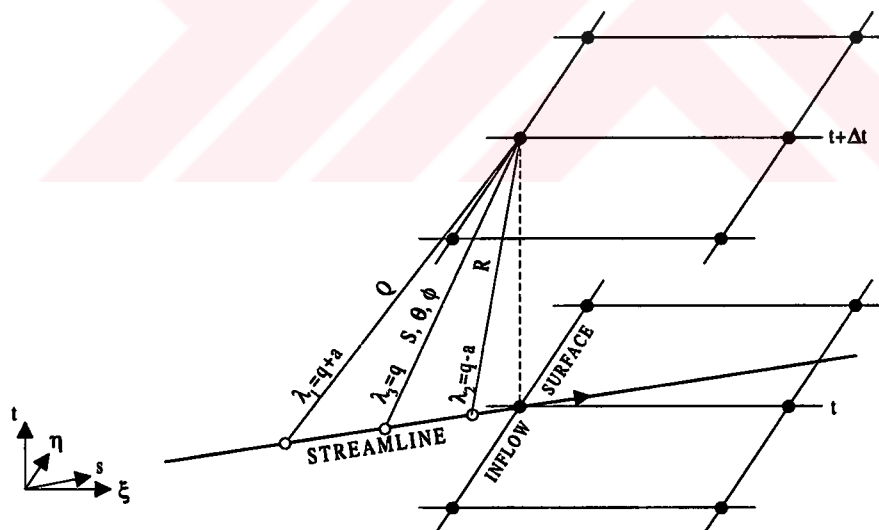
$$\lambda_2 = q - a > 0$$

$$\lambda_3 = q > 0$$

Hence, all of the characteristics carry information from outside the computational domain. So, the value of R at the boundary must be specified as a physical boundary condition in addition to Q , S and the flow angles θ and ϕ .



a. One-dimensional flow



b. Two-dimensional flow

Figure 4.2. Supersonic inflow boundary

4.1.3. Subsonic Outflow Boundary Condition

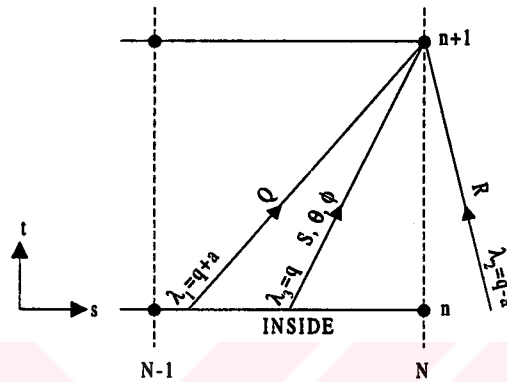
If the outflow velocity is subsonic (Figure 4.3),

$$\lambda_1 = q + a > 0$$

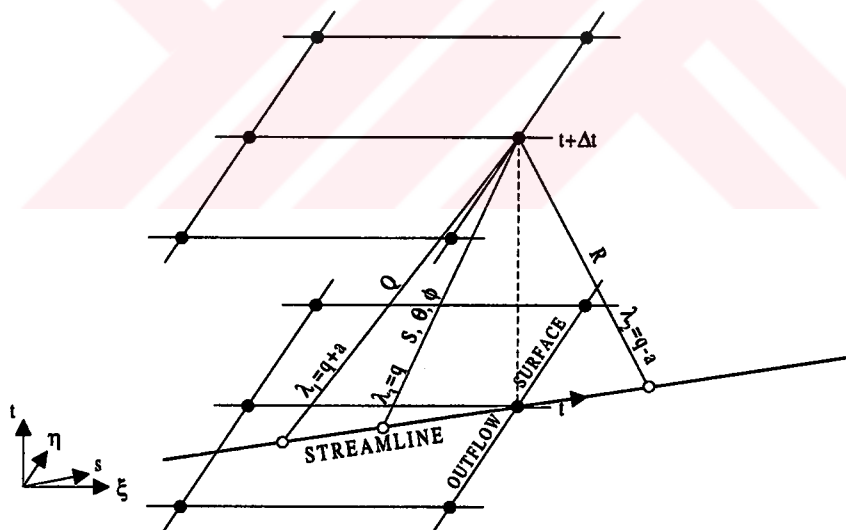
$$\lambda_2 = q - a < 0$$

$$\lambda_3 = q > 0$$

Since the only incoming characteristic from outside the computational domain is that of R, only the value of R must be specified as the physical boundary condition.



a. One-dimensional flow



b. Two-dimensional flow

Figure 4.3. Subsonic outflow boundary

4.1.4. Supersonic Outflow Boundary Condition

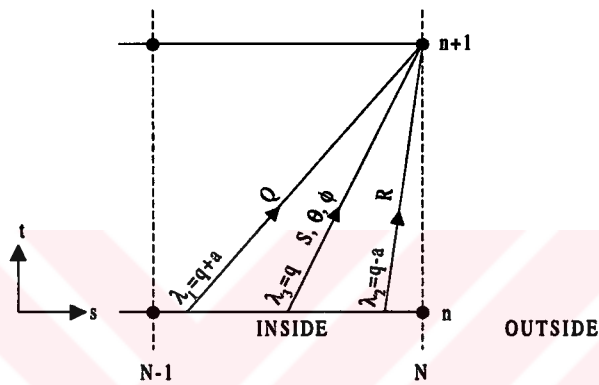
If the outflow velocity is supersonic (Figure 4.4),

$$\lambda_1 = q + a > 0$$

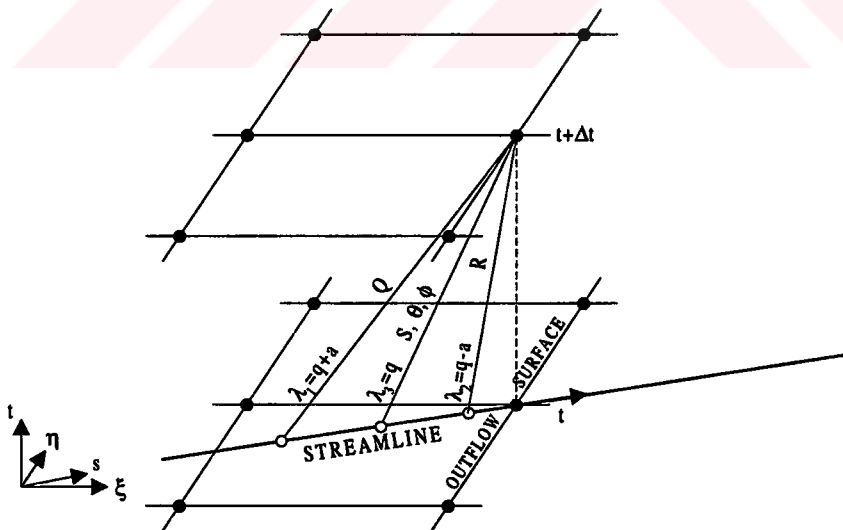
$$\lambda_2 = q - a > 0$$

$$\lambda_3 = q > 0$$

Since, no characteristic line brings any information from outside the computational domain, all of the dependent variables are determined with information from the interior of the computational domain and no physical boundary condition need to be specified.



b. One-dimensional flow



b. Two-dimensional flow

Figure 4.4. Supersonic outflow boundary

Note that, the discussion given above in Sections 4.1.1 to 4.1.4 holds true no matter the flow direction is from left to the right or vice versa. The flow variables which must be specified explicitly on the boundaries just depend on the flow regime (ie. subsonic or supersonic flow) and the type of far field boundary (ie. inflow or outflow boundary). To summarise a table is given below.

Table 4.1. Variables specified as far field physical boundary conditions

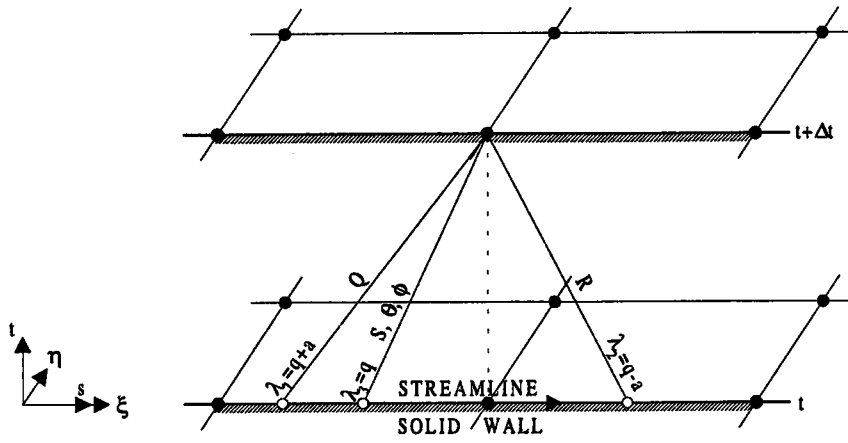
	<i>Subsonic Flow</i>	<i>Supersonic Flow</i>
<i>Inflow Boundary</i>	Q, S, θ , ϕ	Q, R, S, θ , ϕ
<i>Outflow Boundary</i>	R	–

4.2. SOLID WALL BOUNDARY CONDITIONS

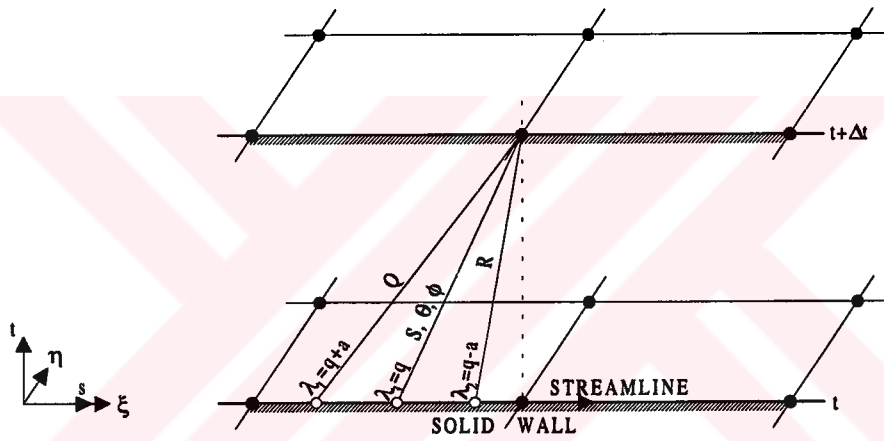
Solid wall is a stream surface in a multi-dimensional flow (Figure 4.5). Since the streamlines are constrained to the solid wall, the velocity vector can only rotate in the local tangency plane. Because of this, the flow angles θ and ϕ are algebraically related on a solid surface.

Solid wall boundary points are therefore treated as normal interior points of the computational domain with the exception that the flow angles θ and ϕ are dependent on each other on the solid wall. Therefore, on the solid wall the flow angles θ and ϕ are updated taking the solid wall geometry into account.

On a solid wall, since the flow angles θ and ϕ are algebraically related, one of the flow angles (θ on $k=1$ and $k=k_{mx}$ surface, ϕ on $j=1$ and $j=j_{mx}$ surface) is calculated through integration of the equations of motion, while the other is calculated based on the other flow angle and the local tangency plane.



a. Subsonic flow



b. Supersonic flow

Figure 4.5. Solid wall boundary in two-dimensional flow

Let at a point on a solid wall the unit normal vector be \bar{u}_n , where

$$\bar{u}_n = \begin{pmatrix} x_n \\ y_n \\ z_n \end{pmatrix} \quad (4.1)$$

and let the flow angle be ϕ , then the intersection of the plane defined by the unit normal vector \bar{u}_ϕ , where

$$\bar{u}_\phi = \begin{pmatrix} -\sin(\phi) \\ 0 \\ \cos(\phi) \end{pmatrix} \quad (4.2)$$

and the solid wall forms a line which is parallel to the velocity vector \bar{u} , where

$$\bar{u} = \begin{pmatrix} \cos(\phi) \\ \tan(\theta) \\ \sin(\phi) \end{pmatrix} \quad (4.3)$$

In mathematical terms

$$\bar{u}_n \times \bar{u}_\phi \parallel \bar{u} \quad (4.4)$$

which implies the relation

$$x_n \cos(\phi) + z_n \sin(\phi) = -y_n \tan(\theta) \quad (4.5)$$

The equation derived above forms the basis of solid wall boundary treatment. Using this relation θ and ϕ can be expressed in terms of each other and the normal vector of the solid wall as follows,

$$\theta = a \tan\left(\frac{x_n \cos(\phi) + z_n \sin(\phi)}{-y_n}\right) \quad (4.6)$$

and

$$\phi_{1,2} = 2 a \tan\left(\frac{-z_n \pm \sqrt{z_n^2 + x_n^2 - y_n^2 \tan^2(\theta)}}{-x_n + y_n \tan(\theta)}\right) \quad (4.7)$$

On a solid wall boundary ($k=1$ or $k=kmx$) the flow angle θ is determined using the unit process of a normal inner node. The value of the other flow angle, ϕ is calculated using Equation 4.7.

Similarly, on a solid wall boundary ($j=1$ or $j=j_{mx}$) the flow angle ϕ is determined using the unit process of a normal inner node. The value of the other flow angle, θ is calculated using Equation 4.6.

4.3. PERIODIC BOUNDARY CONDITIONS

In cascades the flow has a periodic nature in blade to blade direction. The boundaries separating regions of this nature are called the periodic boundaries. Periodic boundaries need special treatment in the solution process.

If the cascade is linear, the flow repeats itself in blade to blade direction which is parallel to the z-axis. In this case, the periodic boundaries are on $k=1$ and $k=k_{mx}$ planes and the nodes on the periodic boundaries are treated as normal inner nodes.

Phantom nodes are required for this purpose. Geometric and flow parameters of phantom nodes used in unit operations on $k=1$ periodic boundary are obtained using those of $k=k_{mx}-1$ nodes (See Figure 4.6). In mathematical terms, on phantom nodes P1,

$$Q_{i,j,P1} = Q_{i,j,k_{mx}-1} \quad (4.8)$$

$$R_{i,j,P1} = R_{i,j,k_{mx}-1} \quad (4.9)$$

$$S_{i,j,P1} = S_{i,j,k_{mx}-1} \quad (4.10)$$

$$\theta_{i,j,P1} = \theta_{i,j,k_{mx}-1} \quad (4.11)$$

$$\phi_{i,j,P1} = \phi_{i,j,k_{mx}-1} \quad (4.12)$$

$$X_{i,j,P1} = X_{i,j,k_{mx}-1} \quad (4.13)$$

$$Y_{i,j,P1} = Y_{i,j,k_{mx}-1} \quad (4.14)$$

$$Z_{i,j,P1} = Z_{i,j,k_{mx}-1} - \ell_p \quad (4.15)$$

where ℓ_p is the pitch of the linear cascade.

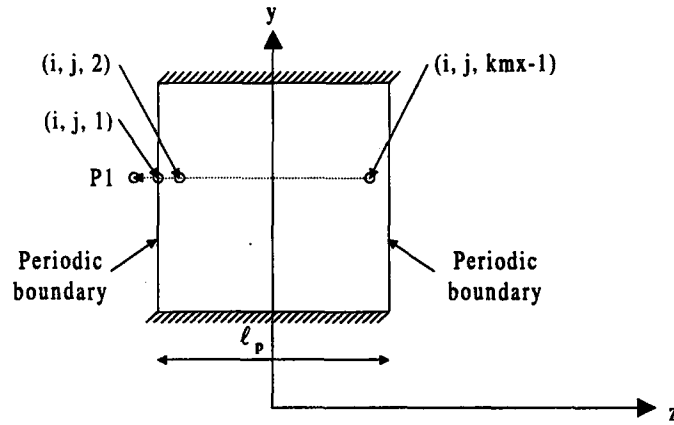


Figure 4.6. Phantom node P1 (linear cascade)

Similarly, geometric and flow parameters of phantom nodes used in unit operations on $k=kmx$ periodic boundary are obtained using those of $k=2$ nodes (See Figure 4.7).

In mathematical terms, on phantom nodes P2,

$$Q_{i,j,P2} = Q_{i,j,2} \quad (4.16)$$

$$R_{i,j,P2} = R_{i,j,2} \quad (4.17)$$

$$S_{i,j,P2} = S_{i,j,2} \quad (4.18)$$

$$\theta_{i,j,P2} = \theta_{i,j,2} \quad (4.19)$$

$$\phi_{i,j,P2} = \phi_{i,j,2} \quad (4.20)$$

$$x_{i,j,P2} = x_{i,j,2} \quad (4.21)$$

$$y_{i,j,P2} = y_{i,j,2} \quad (4.22)$$

$$z_{i,j,P2} = z_{i,j,2} + \ell_p \quad (4.23)$$

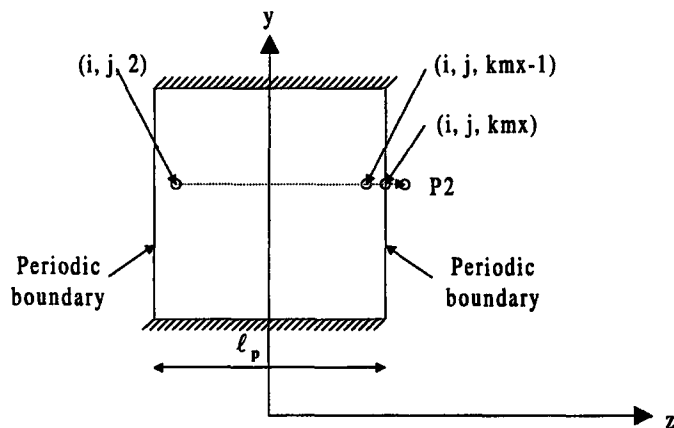


Figure 4.7. Phantom node P2 (linear cascade)

However, if the cascade is annular, periodic wall treatment is somewhat complicated compared to the approach described above. Assumptions given above for linear cascades do not hold for annular cascades. For annular cascades, on phantom nodes P1 (See Figure 4.8),

$$Q_{i,j,P1} = Q_{i,j,kmx-1} \quad (4.24)$$

$$R_{i,j,P1} = R_{i,j,kmx-1} \quad (4.25)$$

$$S_{i,j,P1} = S_{i,j,kmx-1} \quad (4.26)$$

$$\theta_{i,j,P1} = a \sin\left(\sin(\theta_{i,j,kmx-1}) \cos(\alpha) + \cos(\theta_{i,j,kmx-1}) \sin(\phi_{i,j,kmx-1}) \sin(\alpha)\right) \quad (4.27)$$

$$\phi_{i,j,P1} = a \tan\left(-\frac{\tan(\theta_{i,j,kmx-1})}{\cos(\phi_{i,j,kmx-1})} \sin(\alpha) - \tan(\phi_{i,j,kmx-1}) \cos(\alpha)\right) \quad (4.28)$$

$$X_{i,j,P1} = X_{i,j,kmx-1} \quad (4.29)$$

$$Y_{i,j,P1} = \sqrt{y_{i,j,kmx-1}^2 + z_{i,j,kmx-1}^2} \sin\left(a \tan\left(\frac{y_{i,j,kmx-1}}{z_{i,j,kmx-1}}\right) + \alpha\right) \quad (4.30)$$

$$Z_{i,j,P1} = \sqrt{y_{i,j,kmx-1}^2 + z_{i,j,kmx-1}^2} \cos\left(a \tan\left(\frac{y_{i,j,kmx-1}}{z_{i,j,kmx-1}}\right) + \alpha\right) \quad (4.31)$$

where α is the pitch of the annular cascade.

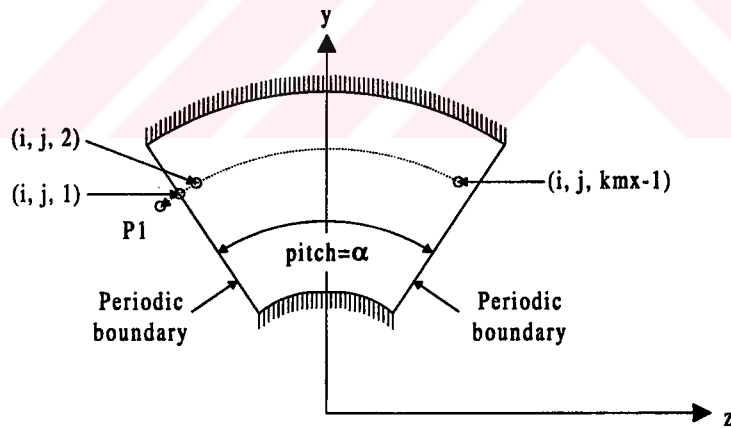


Figure 4.8. Phantom node P1 (annular cascade)

On phantom nodes P2 (See Figure 4.9),

$$Q_{i,j,P2} = Q_{i,j,2} \quad (4.32)$$

$$R_{i,j,P2} = R_{i,j,2} \quad (4.33)$$

$$S_{i,j,P2} = S_{i,j,2} \quad (4.34)$$

$$\theta_{i,j,P2} = a \sin(\sin(\theta_{i,j,2}) \cos(\alpha) - \cos(\theta_{i,j,2}) \sin(\phi_{i,j,2}) \sin(\alpha)) \quad (4.35)$$

$$\phi_{i,j,P2} = a \tan\left(\frac{\tan(\theta_{i,j,2})}{\cos(\phi_{i,j,2})} \sin(\alpha) - \tan(\phi_{i,j,2}) \cos(\alpha)\right) \quad (4.36)$$

$$y_{i,j,P2} = \sqrt{y_{i,j,2}^2 + z_{i,j,2}^2} \sin\left(a \tan\left(\frac{y_{i,j,2}}{z_{i,j,2}}\right) - \alpha\right) \quad (4.37)$$

$$z_{i,j,P2} = \sqrt{y_{i,j,2}^2 + z_{i,j,2}^2} \cos\left(a \tan\left(\frac{y_{i,j,2}}{z_{i,j,2}}\right) - \alpha\right) \quad (4.38)$$

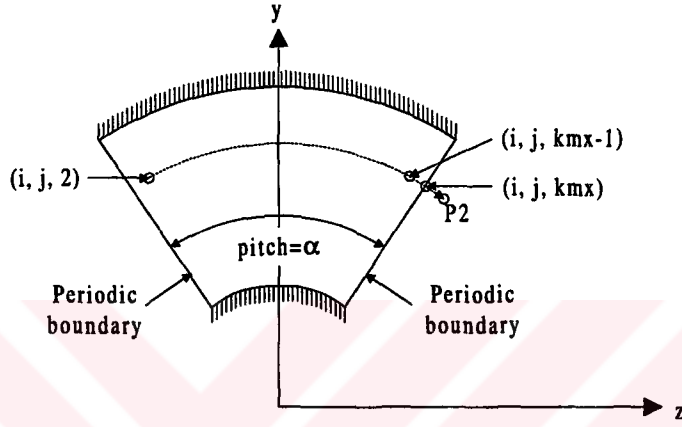


Figure 4.9. Phantom node P2 (annular cascade)

In addition to the process described above, after each time level the values of parameters on periodic boundary nodes are updated by averaging the values at the previous time level, such that, for linear cascades,

$$Q_{i,j,1}^{n+1} = Q_{i,j,kmx}^{n+1} = \frac{1}{2} (Q_{i,j,1}^n + Q_{i,j,kmx}^n) \quad (4.39)$$

$$R_{i,j,1}^{n+1} = R_{i,j,kmx}^{n+1} = \frac{1}{2} (R_{i,j,1}^n + R_{i,j,kmx}^n) \quad (4.40)$$

$$S_{i,j,1}^{n+1} = S_{i,j,kmx}^{n+1} = \frac{1}{2} (S_{i,j,1}^n + S_{i,j,kmx}^n) \quad (4.41)$$

$$\theta_{i,j,1}^{n+1} = \theta_{i,j,kmx}^{n+1} = \frac{1}{2} (\theta_{i,j,1}^n + \theta_{i,j,kmx}^n) \quad (4.42)$$

$$\phi_{i,j,1}^{n+1} = \phi_{i,j,kmx}^{n+1} = \frac{1}{2} (\phi_{i,j,1}^n + \phi_{i,j,kmx}^n) \quad (4.43)$$

and for annular cascades,

$$Q_{i,j,l}^{n+1} = Q_{i,j,kmx}^{n+1} = \frac{1}{2}(Q_{i,j,l}^n + Q_{i,j,kmx}^n) \quad (4.44)$$

$$R_{i,j,l}^{n+1} = R_{i,j,kmx}^{n+1} = \frac{1}{2}(R_{i,j,l}^n + R_{i,j,kmx}^n) \quad (4.45)$$

$$S_{i,j,l}^{n+1} = S_{i,j,kmx}^{n+1} = \frac{1}{2}(S_{i,j,l}^n + S_{i,j,kmx}^n) \quad (4.46)$$

$$\theta_{i,j,l}^{n+1} = \frac{1}{2}(\theta_{i,j,l}^n + \theta_{i,j,P1}^n) \quad (4.47)$$

$$\theta_{i,j,kmx}^{n+1} = \frac{1}{2}(\theta_{i,j,kmx}^n + \theta_{i,j,P2}^n) \quad (4.48)$$

$$\phi_{i,j,l}^{n+1} = \frac{1}{2}(\phi_{i,j,l}^n + \phi_{i,j,P1}^n) \quad (4.49)$$

$$\phi_{i,j,kmx}^{n+1} = \frac{1}{2}(\phi_{i,j,kmx}^n + \phi_{i,j,P2}^n) \quad (4.50)$$

where

$$\theta_{i,j,P1}^n = a \sin(\sin(\theta_{i,j,kmx}^n) \cos(\alpha) + \cos(\theta_{i,j,kmx}^n) \sin(\phi_{i,j,kmx}^n) \sin(\alpha)) \quad (4.51)$$

$$\theta_{i,j,P2}^n = a \sin(\sin(\theta_{i,j,l}^n) \cos(\alpha) + \cos(\theta_{i,j,l}^n) \sin(\phi_{i,j,l}^n) \sin(\alpha)) \quad (4.52)$$

$$\phi_{i,j,P1}^n = a \tan\left(-\frac{\tan(\theta_{i,j,kmx}^n)}{\cos(\phi_{i,j,kmx}^n)} \sin(\alpha) - \tan(\phi_{i,j,kmx}^n) \cos(\alpha)\right) \quad (4.53)$$

$$\phi_{i,j,P2}^n = a \tan\left(-\frac{\tan(\theta_{i,j,l}^n)}{\cos(\phi_{i,j,l}^n)} \sin(\alpha) - \tan(\phi_{i,j,l}^n) \cos(\alpha)\right) \quad (4.54)$$

Updating by averaging the values at the previous time level is necessary to impose the periodicity condition that the values of flow parameters must be equal at corresponding nodes of periodic boundaries.

CHAPTER 5

RESULTS AND DISCUSSION

In this chapter the tests cases solved for the validation of the present numerical method are presented and the results are discussed.

The first test case is a classical shock tube problem. It is used to verify that the unsteady wave motion is modelled correctly and discontinuities in the flow are solved accurately. The results are compared with the analytical solution.

The second test case deals with the quasi-one-dimensional transonic flow in a Laval nozzle. In this test case, the results are compared with the analytical solution and the steady state solution is shown to be accurate and the discontinuities are shown to be located in the nozzle correctly.

The third test case is about a two-dimensional inlet flow where the supersonic flow is turned by a ramp. This test case demonstrates that an isentropic shock is captured and its geometry is predicted. The results are compared with that of another numerical solution.

The fourth test case deals with a two-dimensional subsonic flow over a sinusoidal bump. Symmetry about the bump which is an indication of the accuracy is demonstrated. The results are compared with that of another numerical solution.

The fifth test case demonstrates capability of solving three-dimensional problems. The inlet flow is supersonic and symmetric about the diagonal of the inlet area. The solution is shown to be symmetric all through the constant area duct. The results are compared with that of another numerical solution.

The sixth case involves the subsonic flow through a 90° curved duct with uniform square cross-section. A non-uniform inlet velocity distribution is specified which might have been created by upstream frictional effects. The secondary flow created due to non-uniform inlet condition and high turning of the flow is examined.

The test cases worked on are summarised in the Table 5.1 and details are discussed in the following sections.

Table 5.1. Summary of Test Cases

Test Case	Geometry	Dim.	Mach Number	Flow Regime	Flow Features Tested
1	Shock Tube	1D	N/A	Transonic	Shock tracking and shock correction
2	Laval Nozzle	Quasi 1D	0.8	Transonic	Shock tracking and shock correction
3	Rectangular Inlet	2D	2.0	Supersonic	Shock geometry
4	Sinusoidal Bump	2D	0.39	Subsonic	Symmetry about the throat
5	Constant Area Duct	3D	2.0	Supersonic	Shock-shock interaction
6	90° Bend	3D	0.2–0.5	Subsonic	Secondary flow

5.1. SHOCK TUBE (1D)

Shock tube is an important tool in understanding high speed compressible flow and unsteady wave propagation. It is a tube closed at both ends, with a diaphragm separating a region of high pressure gas from a region of low pressure gas. The high pressure side is called the driver section and the low pressure side is called the driven section. The gases separated by the diaphragm can be at different temperatures and have different molecular weights. The flow field in the tube after the diaphragm is ruptured is completely determined by the initial conditions across the diaphragm before it is broken. When the diaphragm is ruptured, a shock wave propagates into the driven section and an expansion wave propagates into the driver section. As the normal shock wave propagates towards the stationary low pressure gas it increases the pressure of the gas behind it and induces a flow velocity. The interface between the driver and the driven gases is called the contact surface which also moves with the above mentioned velocity. Across the contact surface entropy might change discontinuously, however, the pressure and velocity are constant. The expansion wave propagates towards the high pressure gas, smoothly and continuously decreasing the high pressure ahead to a lower value behind it. The unsteady wave motion described above is shown in Figure 5.1.1.

A classical shock tube problem was solved to demonstrate that the unsteady wave propagation is modelled correctly. The tube was divided into 100 equal spatial intervals. Initially the gas was at rest at constant temperature with a pressure ratio of 5:1 across the diaphragm which was located in the middle of the tube. After the diaphragm was burst, the contact surface and the shock wave were tracked and a one point shock correction (see Section 3.4.3) was applied after each iteration. The unsteady wave propagation is shown in Figures 5.1.2 to 5.1.5 using the plots of velocity, modified entropy, pressure and density distributions. Steep discontinuities at the contact surface and the shock wave are evident. As expected, across the shock velocity, modified entropy, pressure and density change discontinuously. On the other hand, across the contact surface modified entropy and density change discontinuously whereas velocity and pressure are continuous. The change of flow velocity, modified entropy, pressure and density across the zones 1 to 4 are plotted in

Figure 5.1.6 to Figure 5.1.9 and compared with the exact solution. The results of the present code and the exact solution are in close agreement.

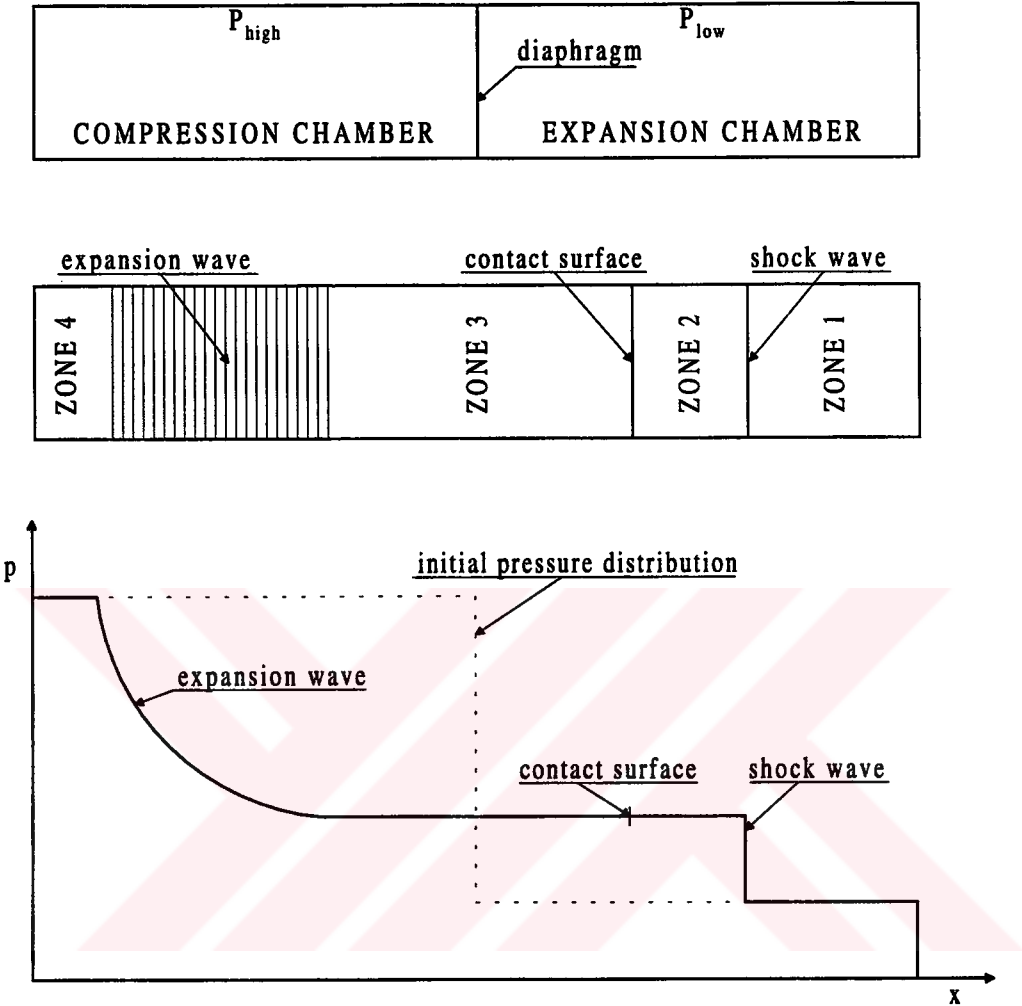


Figure 5.1.1. Shock tube at time=0 and time=t

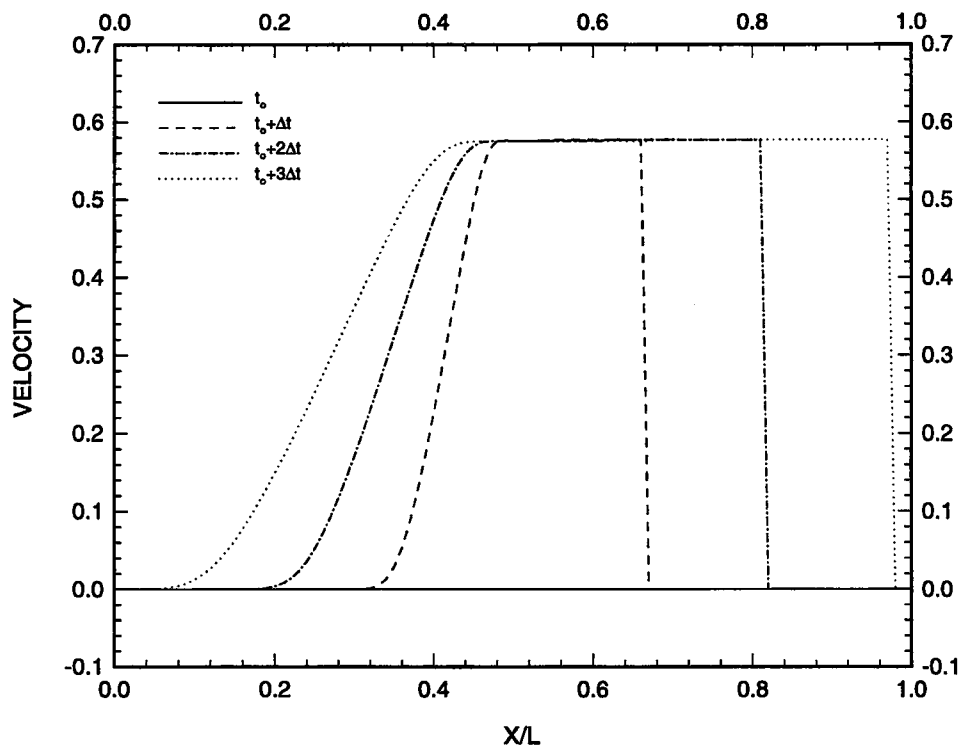


Figure 5.1.2. Velocity distribution along the shock tube

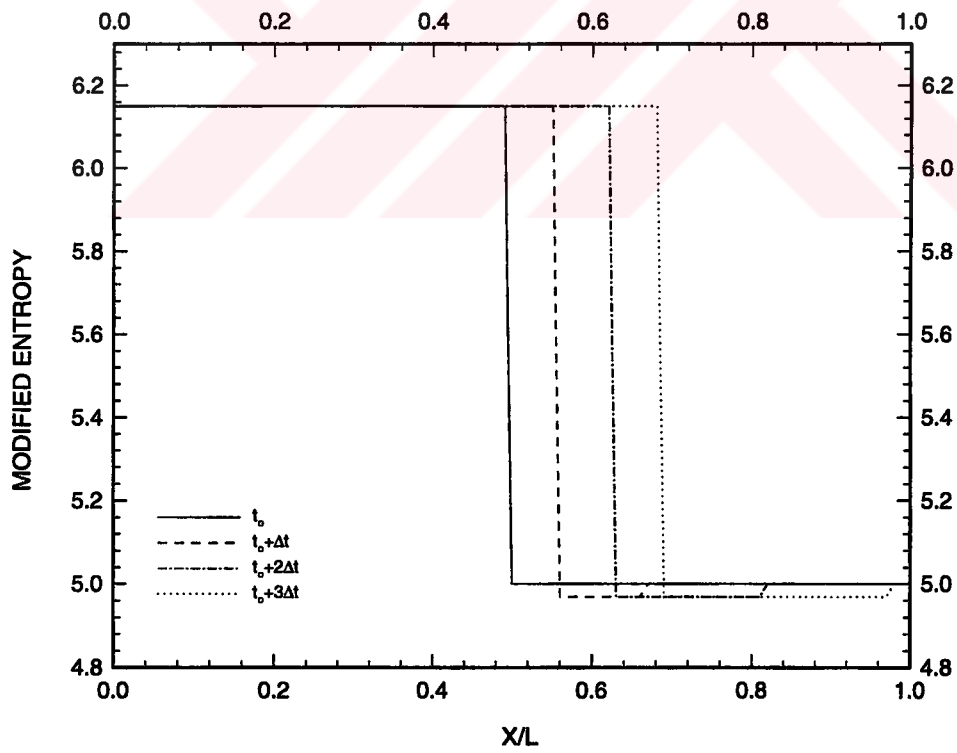


Figure 5.1.3. Entropy distribution along the shock tube

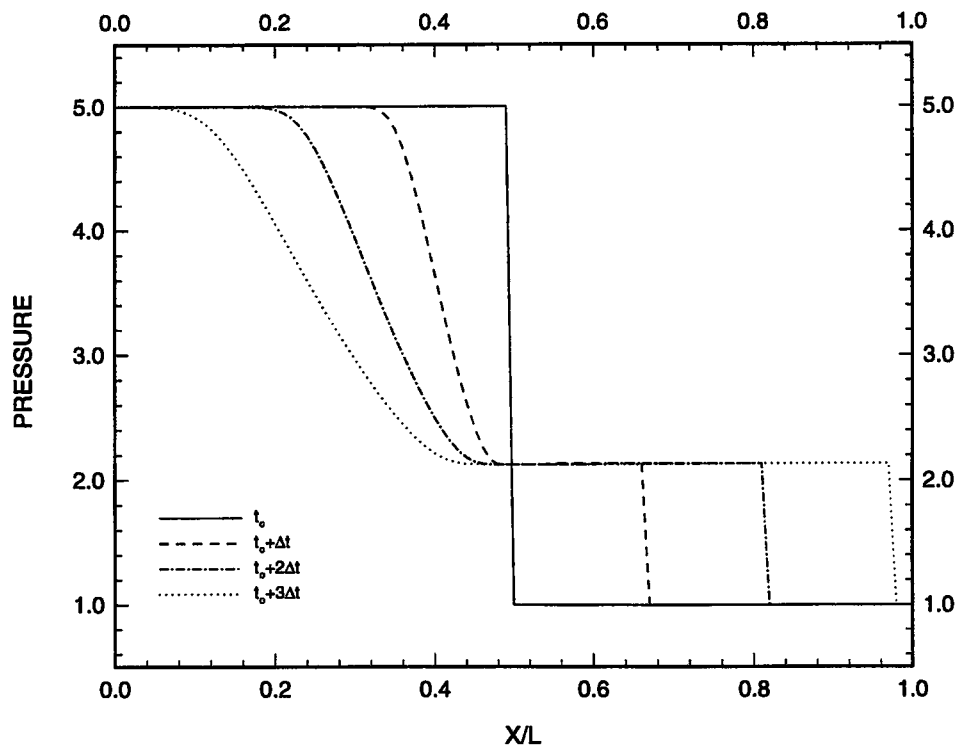


Figure 5.1.4. Pressure distribution along the shock tube

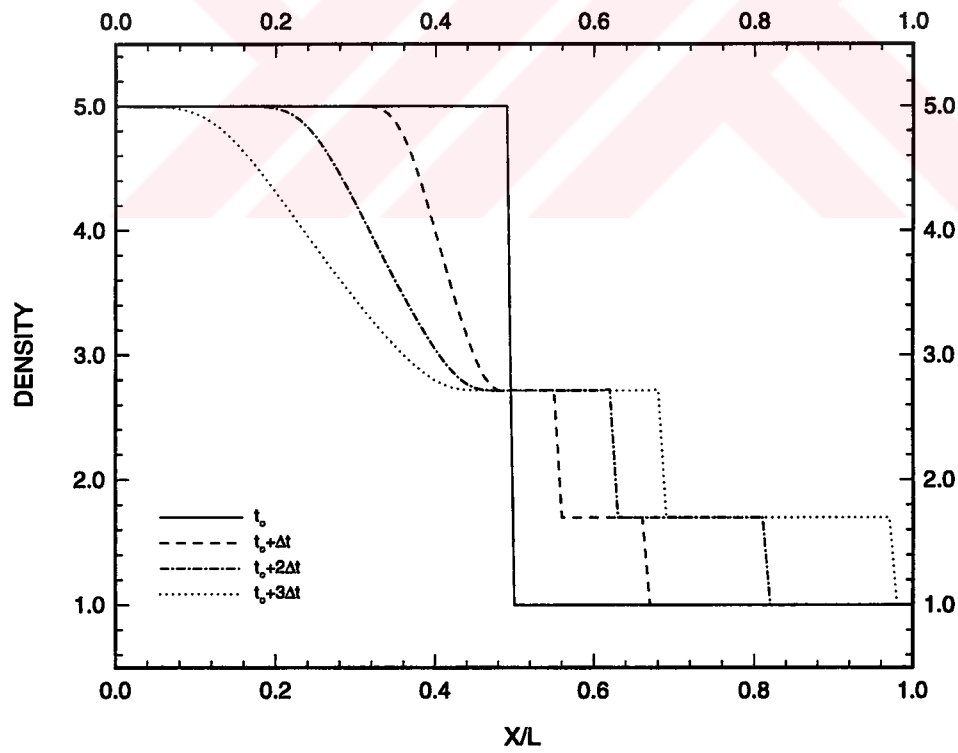


Figure 5.1.5. Density distribution along the shock tube

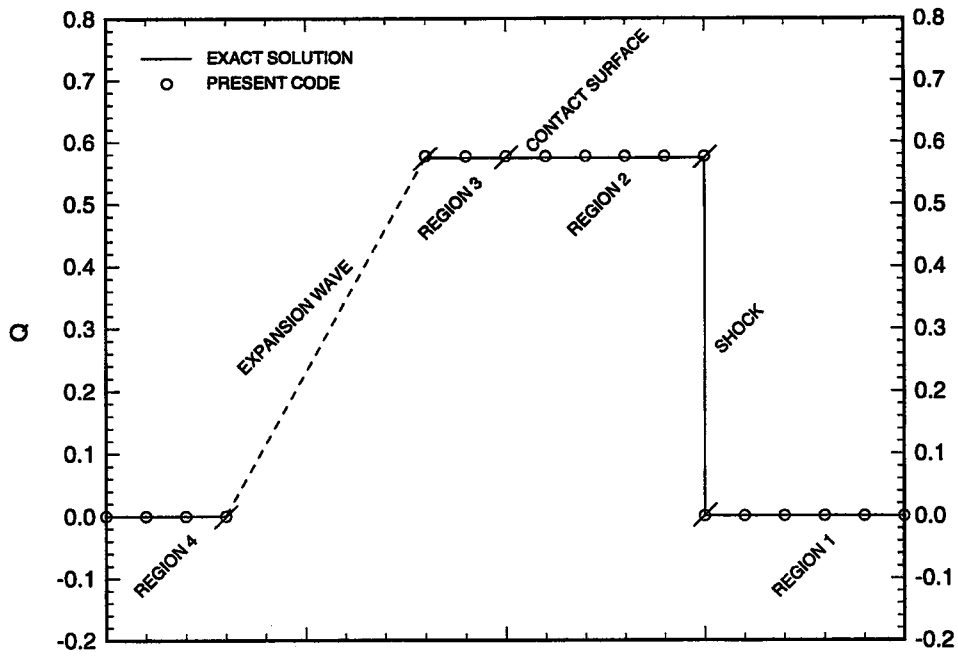


Figure 5.1.6. Change of flow velocity across the zones

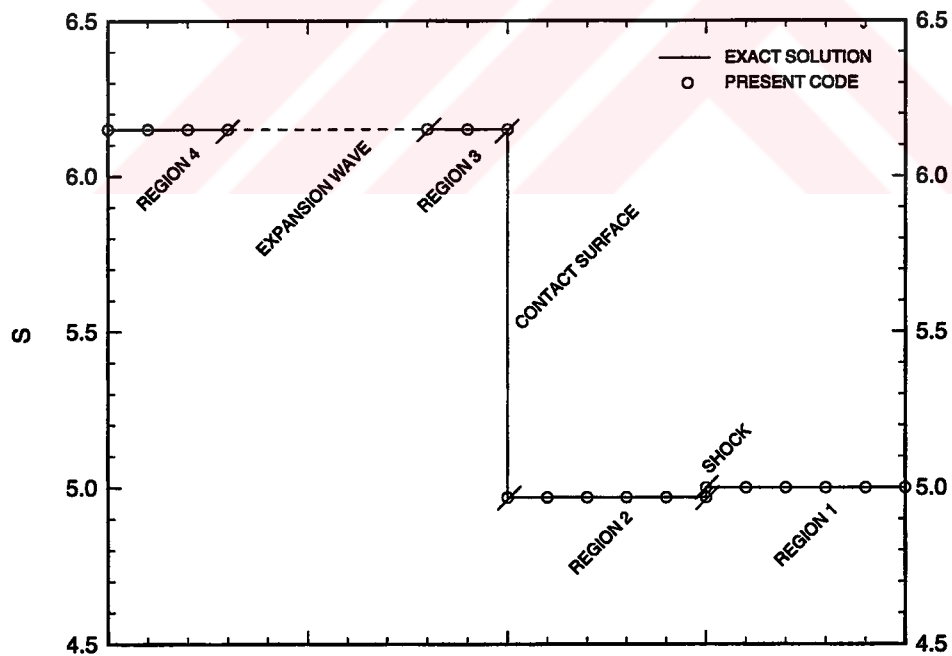


Figure 5.1.7. Change of entropy across the zones

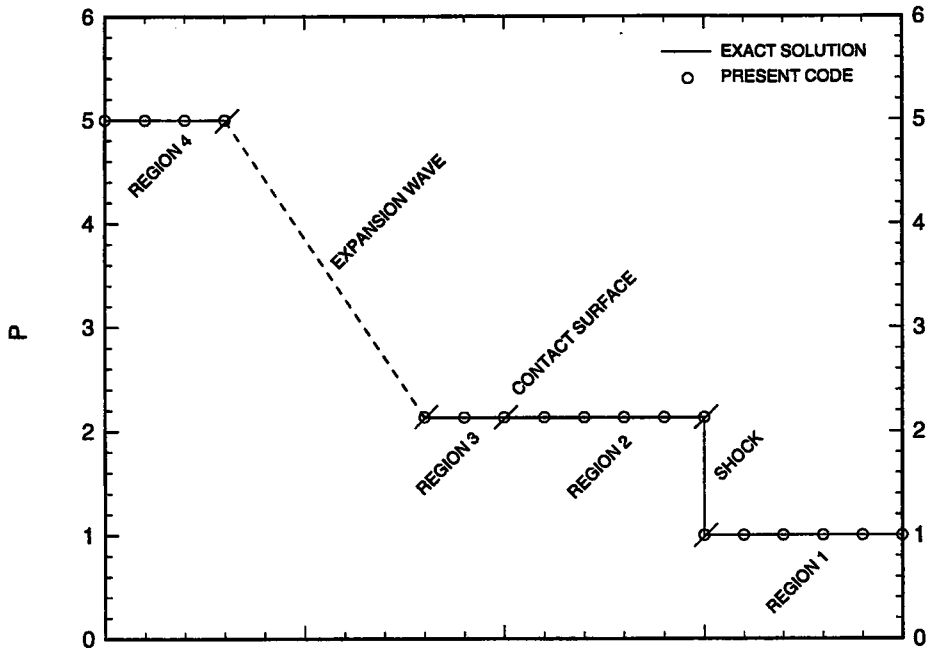


Figure 5.1.8. Change of pressure across the zones

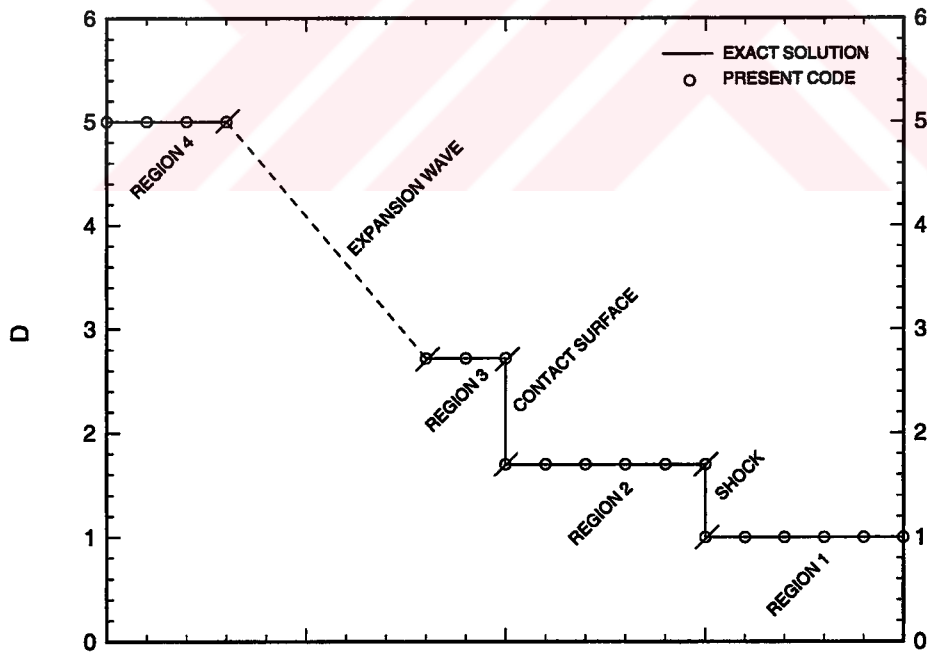


Figure 5.1.9. Change of density across the zones

5.2. TRANSONIC LAVAL NOZZLE (Q1D)

The transonic flow in a converging-diverging nozzle was solved to demonstrate the accuracy of the code for a quasi one-dimensional flow. The geometry of the nozzle is shown in Figure 5.2.1 and the area variation is given below,

$$0 \leq x \leq 2 \quad A(x) = 1 + 0.033333 (1 - 0.5 x)^2$$

$$2 \leq x \leq 10 \quad A(x) = 1 + 0.027083 (1 - 0.5 x)^2$$

Note that the throat is at $x/L=0.2$. Following boundary conditions are used,

$$p_{in} = 6.3953 \quad p_{out} = 6.9085$$

$$T_{in} = 0.9045 \quad T_{out} = 0.9636$$

$$\rho_{in} = 7.0704 \quad \rho_{out} = 7.1698$$

$$u_{in} = 0.7726 \quad u_{out} = 0.5492$$

Initially the nozzle was assumed to be separated by a diaphragm placed at $x/L=0.9$ as discussed in the shock tube test case. Initially the pressure and density ratio across the diaphragm were assumed to be 6.3953:6.9085 and 7.0704:7.1698 respectively. Initially the gas on both sides was assumed to have a flow velocities of 0.7726 and 0.5492. These unrealistic initial conditions were specified to see the robustness of the code. After the diaphragm was ruptured the discontinuity was tracked and a one point shock correction was performed after each iteration as discussed in Section 3.4.3. To obtain a sharp shock, two floating nodes, one placed immediately upstream of the shock and the other placed immediately downstream of the shock were used. CFL number was 0.99.

Starting from this non-physical initial condition the solution converges after about 2100 iterations. The unsteady evolution of the flow in the nozzle is illustrated in Figure 5.2.2.

Steady state pressure, density and Mach number distribution along the nozzle are given in Figure 5.2.3 to Figure 5.2.5 together with the analytical solution. Numerical and analytical results are in excellent agreement. Steady state shock location and the discontinuity magnitude across the shock are predicted accurately.

The convergence history is shown in Figure 5.2.6. The jumps in the convergence history are due to nodes crossed by the shock. This fact is evident in Figure 5.2.7

where shock location and maximum change in pressure are plotted on the same graph. When the shock crosses a node this node experiences a high pressure change which causes these jumps in the convergence history.

Sharp shock geometry, correct shock location and correct shock jump demonstrates that shock tracking and shock correction is managed accurately by the present method.

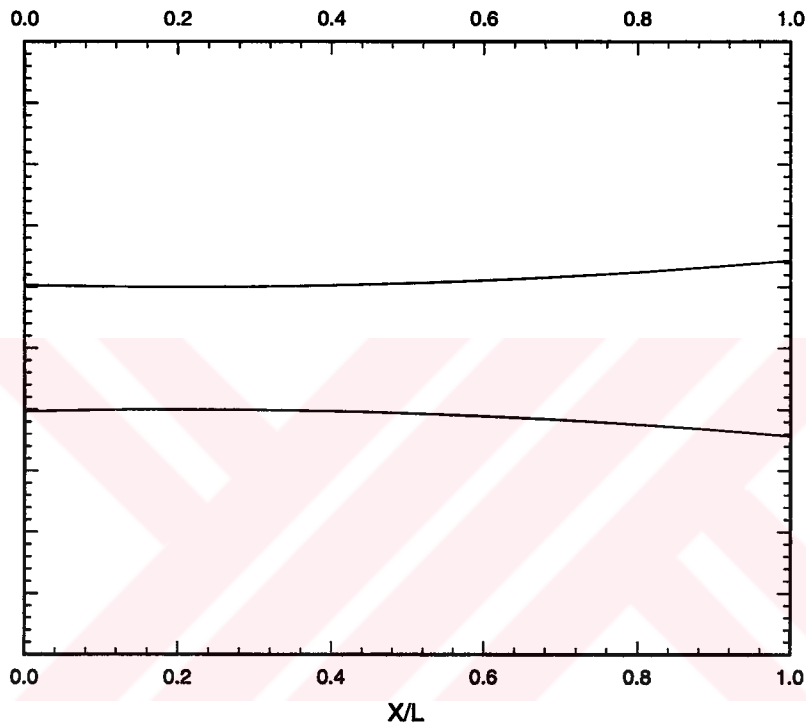


Figure 5.2.1. Converging-diverging nozzle geometry

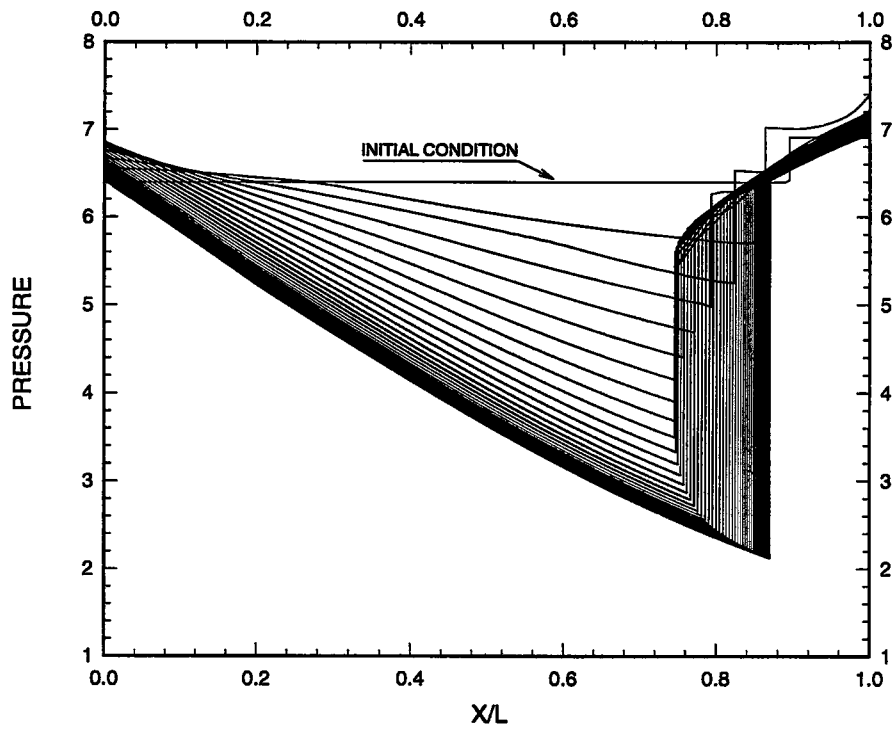


Figure 5.2.2. Unsteady evolution of the flow

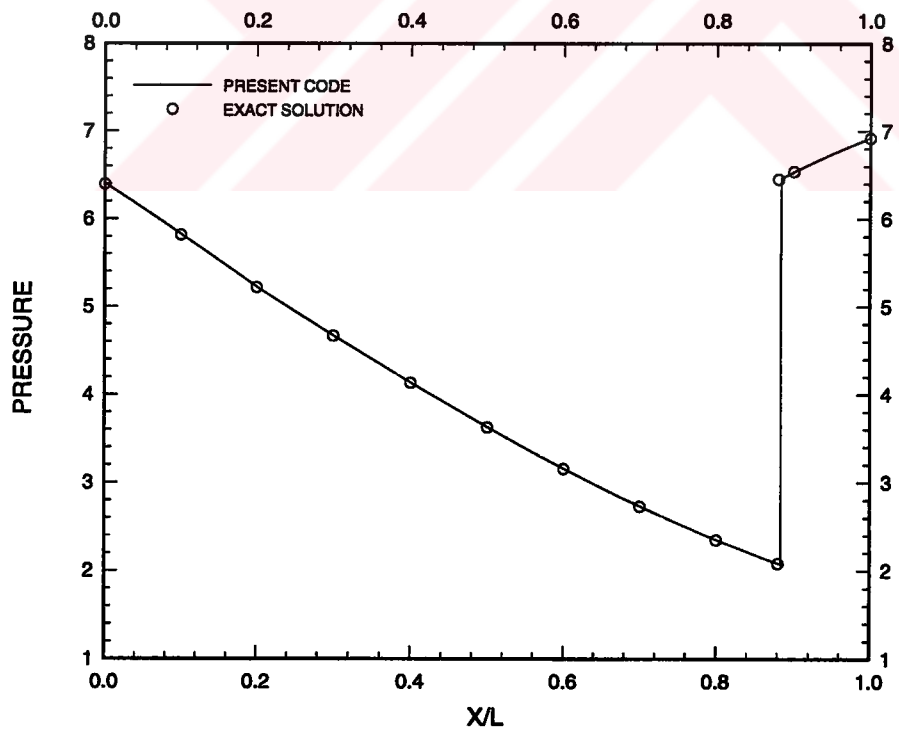


Figure 5.2.3. Steady state pressure distribution along the converging-diverging nozzle

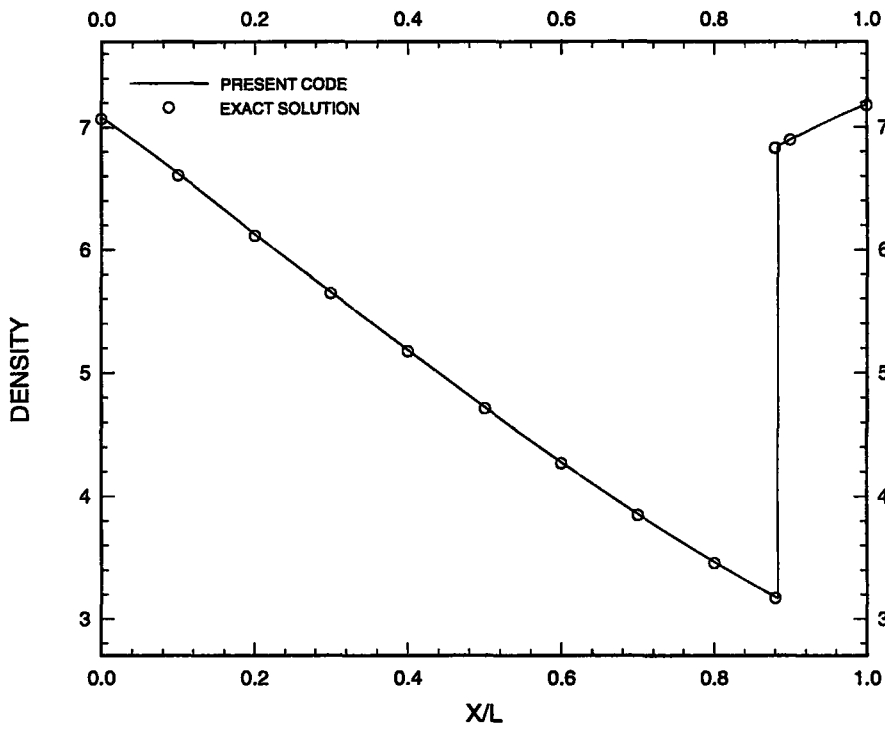


Figure 5.2.4. Steady state density distribution along the converging-diverging nozzle

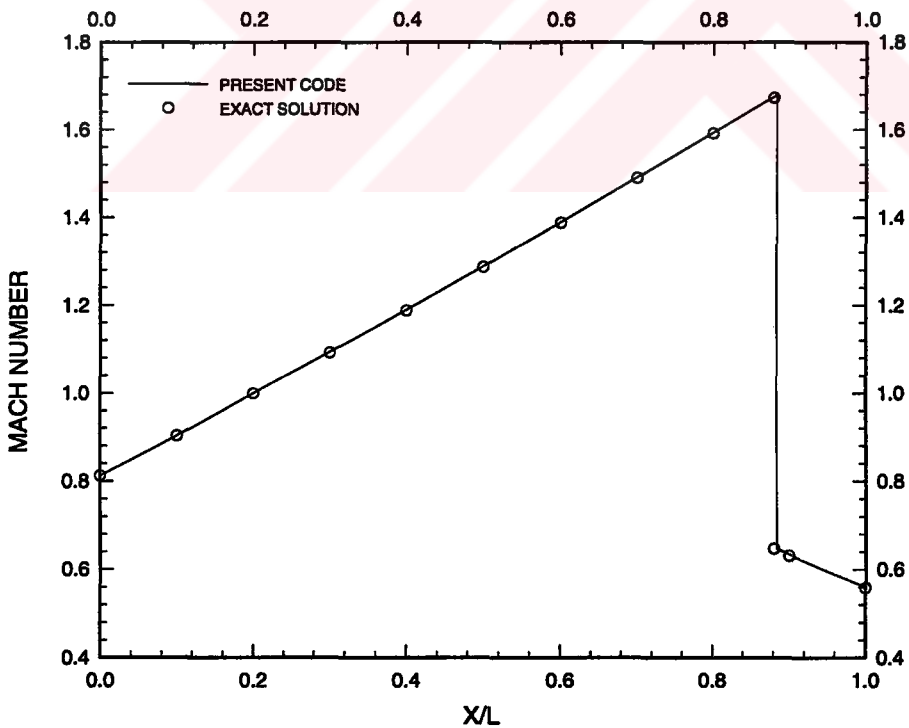


Figure 5.2.5. Steady state velocity distribution along the converging-diverging nozzle

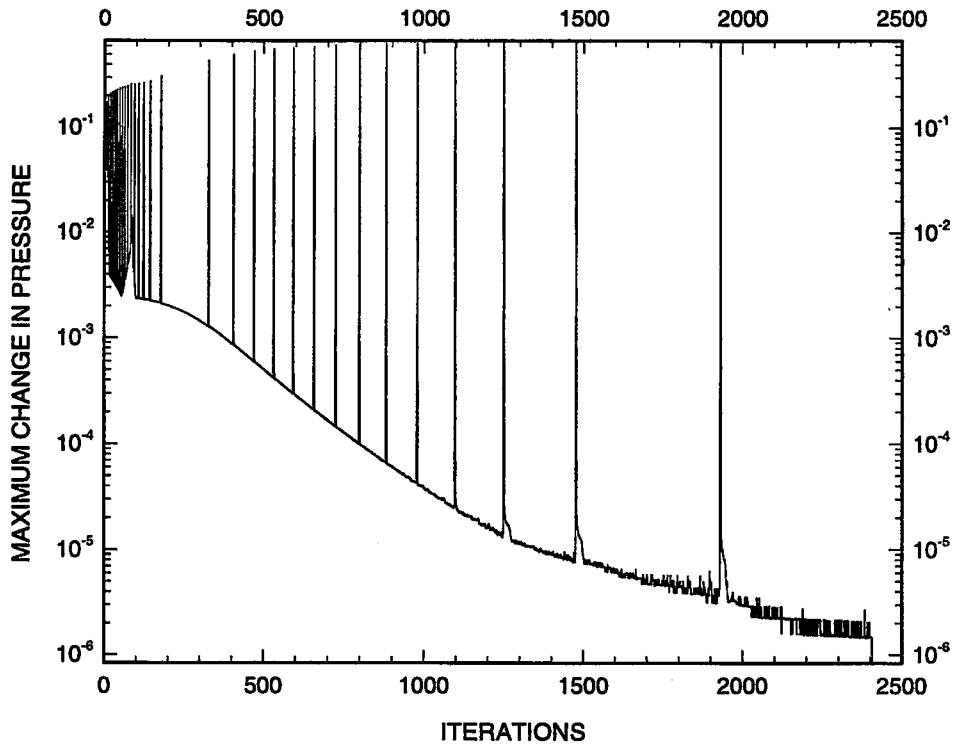


Figure 5.2.6. Convergence history

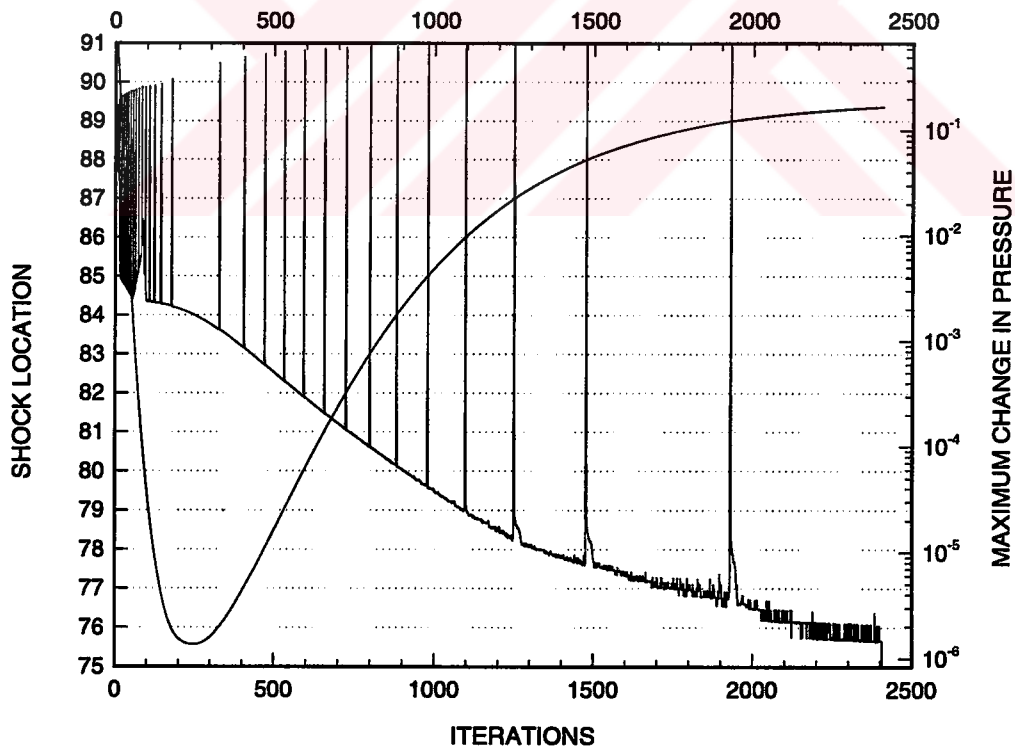


Figure 5.2.7. Shock location and its effect on convergence history

5.3. RECTANGULAR INLET (2D)

The flow in a two-dimensional rectangular inlet at an angle of attack was calculated for an inlet Mach number of 2. The rectangular inlet was inclined 11.5° to the incoming flow. A 71 by 21 grid with square grid cells was used (see Figure 5.3.2). The inlet flow was uniform. Supersonic boundary conditions were applied at the inflow boundary where the Riemann variables Q and R , modified entropy S and the flow angle θ were specified. At the outflow boundary supersonic boundary conditions were used, too. Thus, no flow variable was specified explicitly as the outflow boundary condition, but they were calculated based on the information from the interior of the computational domain. Shock correction was not employed for this test case. The solution converges after about 700 iterations with a CFL number of 0.5 (see Figure 5.3.1). The calculated pressure, Mach number and flow angle contours are shown in Figures 5.3.3, 5.3.4 and 5.3.6, respectively. The numerical results of Verhoff [2] for Mach number and flow angle are shown in Figures 5.3.5 and 5.3.7 for comparison. Formation of an oblique shock on the lower wall and its reflection on the upper wall are evident. Since shock correction was not applied for cells containing the discontinuity, the oblique shocks captured in this test case were isentropic. Although the oblique shocks were smeared the flow features obtained by both codes were similar.

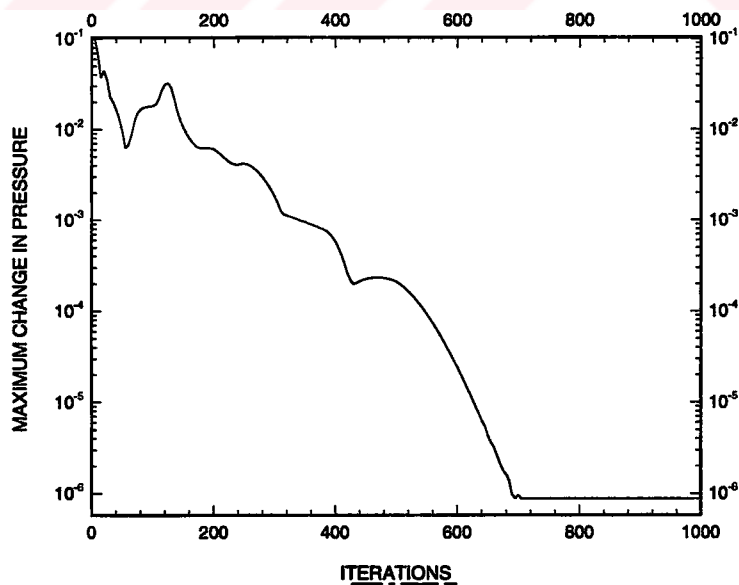


Figure 5.3.1. Convergence history

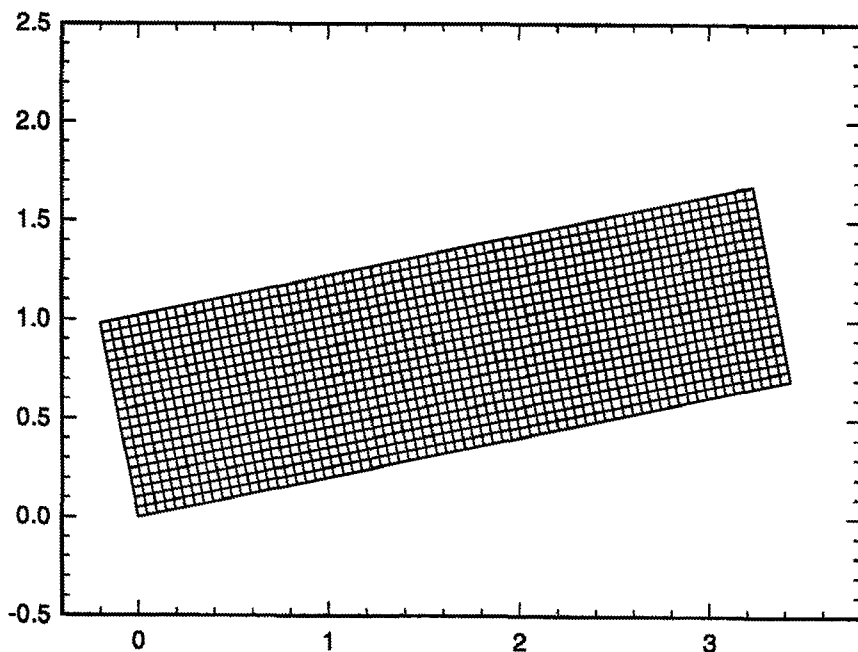


Figure 5.3.2. 71x21 computational mesh

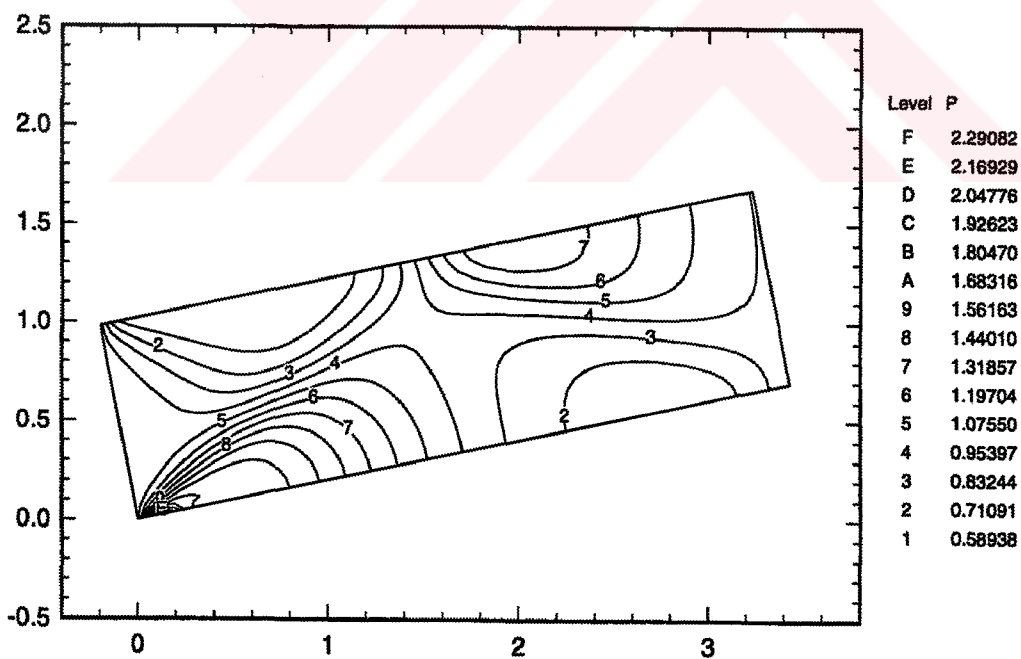


Figure 5.3.3. Pressure contours

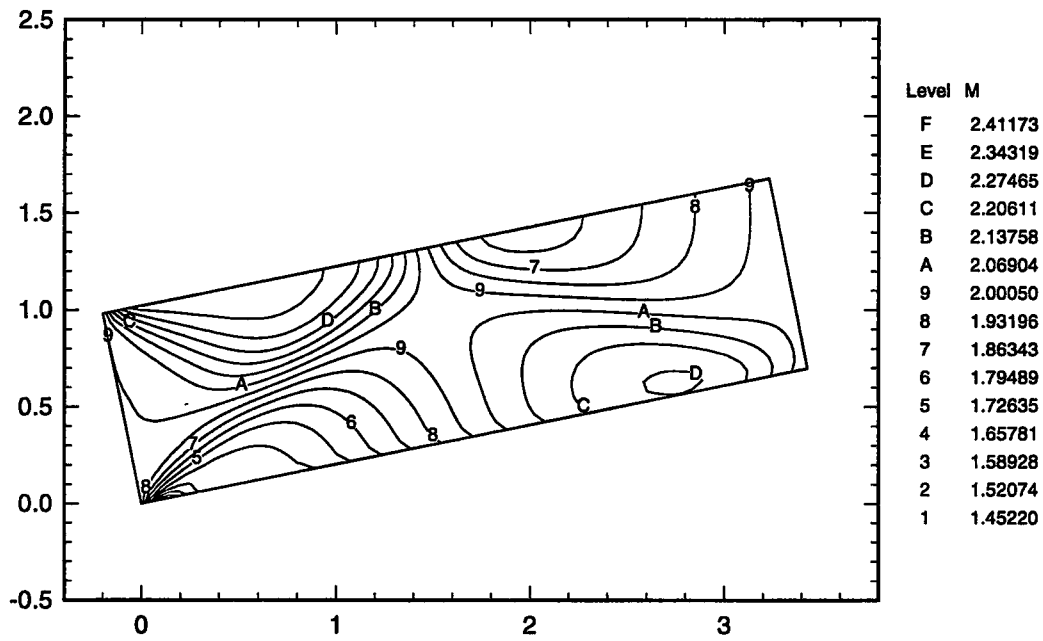


Figure 5.3.4. Mach number contours

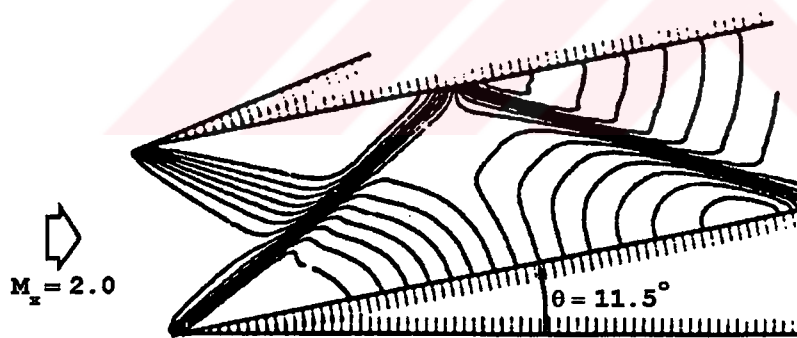


Figure 5.3.5. Mach number contours [2]

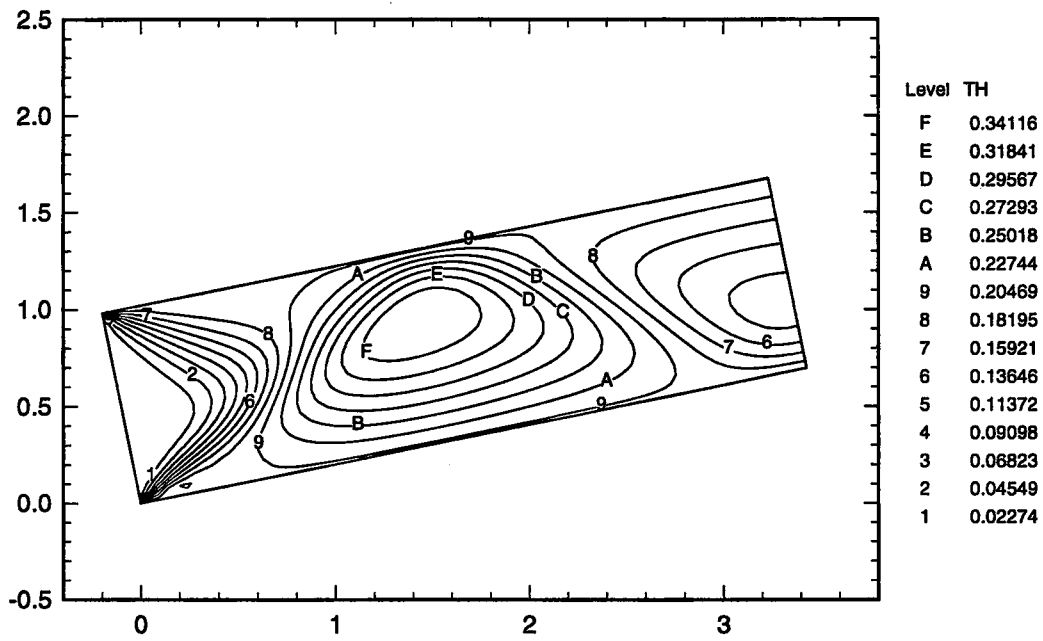


Figure 5.3.6. Flow angle (θ) contours

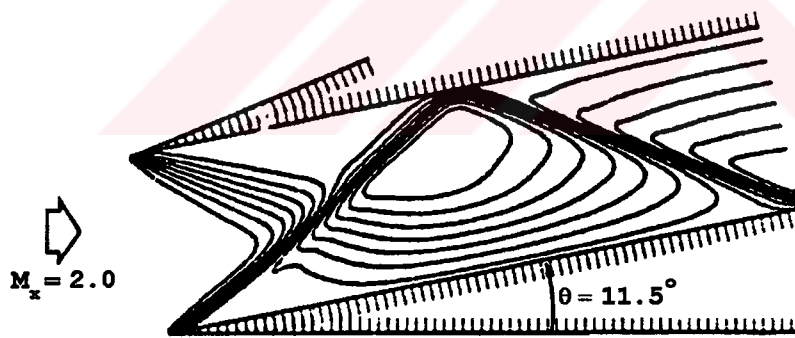


Figure 5.3.7. Flow angle (θ) contours [2]

5.4. SINUSOIDAL BUMP (2D)

The flow in a two dimensional duct with a sinusoidal bump was calculated for an inlet Mach number of 0.39. The duct contour is sinusoidal and symmetric about the throat. The area ratio of the throat is 0.75, and the upstream and downstream areas are equal. The computational grid used in this study is shown in Figure 5.4.2. The computational grid is 161 by 41 where the sinusoidal portion is discretized by a 81 by 41 grid. The computational grid was generated using transfinite interpolation with cubic blending functions [17]. The computational grid used in [12] is also shown for comparison (see Figure 5.4.3).

Zeroth order far field (characteristic) boundary conditions are employed by imposing the constant value of Q_∞ and a zero value of θ along the upstream boundary and the constant value of R_∞ along the downstream boundary. The solution converges after about 5500 iterations with a CFL number of 0.50 (see Figure 5.4.1). The calculated Mach number, pressure and flow angle contours by the present code and that of Verhoff [12] are shown in Figures 5.4.4 to 5.4.9. Mach number and pressure distributions along the lower and upper walls are shown in Figures 5.4.10 to 5.4.13. The contour lines and wall distributions are symmetric about the throat which indicates solution accuracy. Results obtained by both codes agree well.

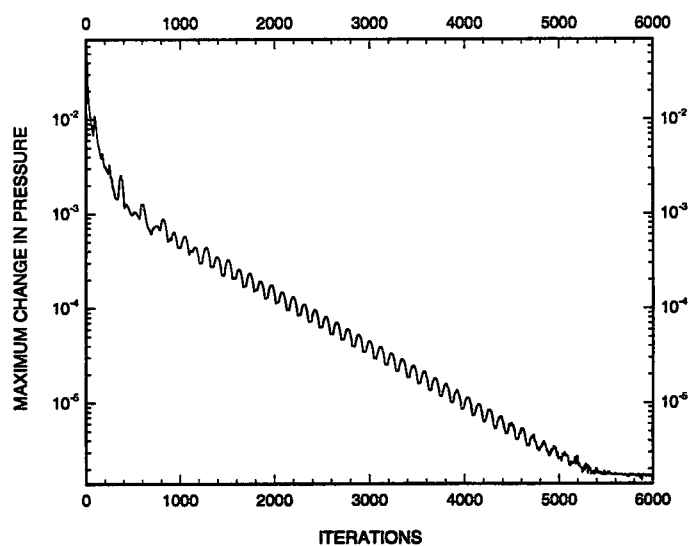


Figure 5.4.1. Convergence history

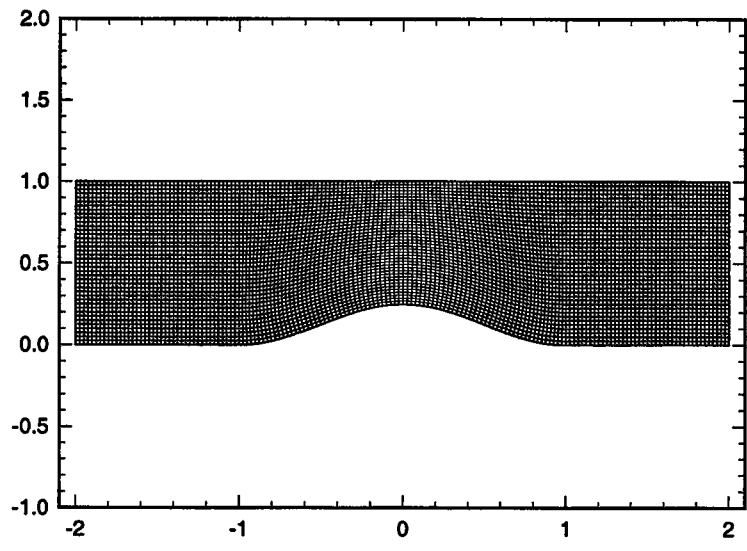


Figure 5.4.2. 161x41 computational mesh

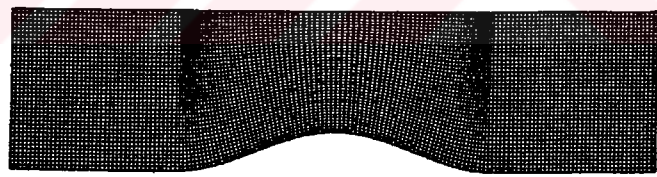


Figure 5.4.3. 161x41 computational mesh [12]

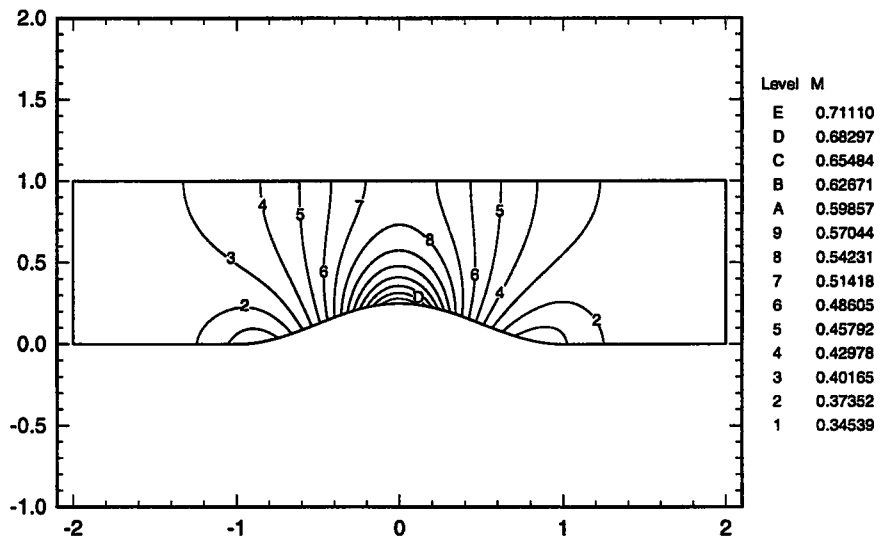


Figure 5.4.4. Mach number contours

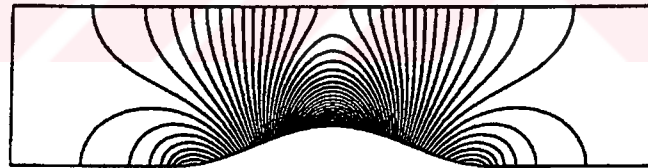


Figure 5.4.5. Mach number contours [12]

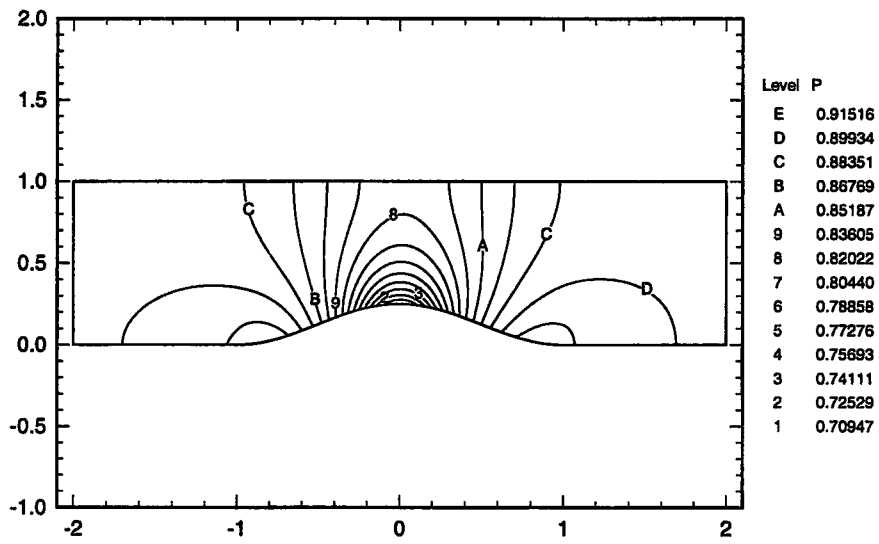


Figure 5.4.6. Pressure contours

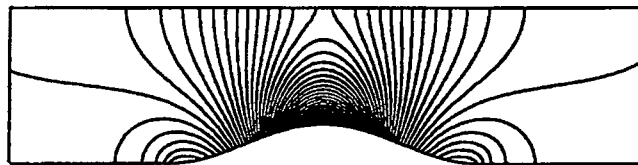


Figure 5.4.7. Pressure contours [12]

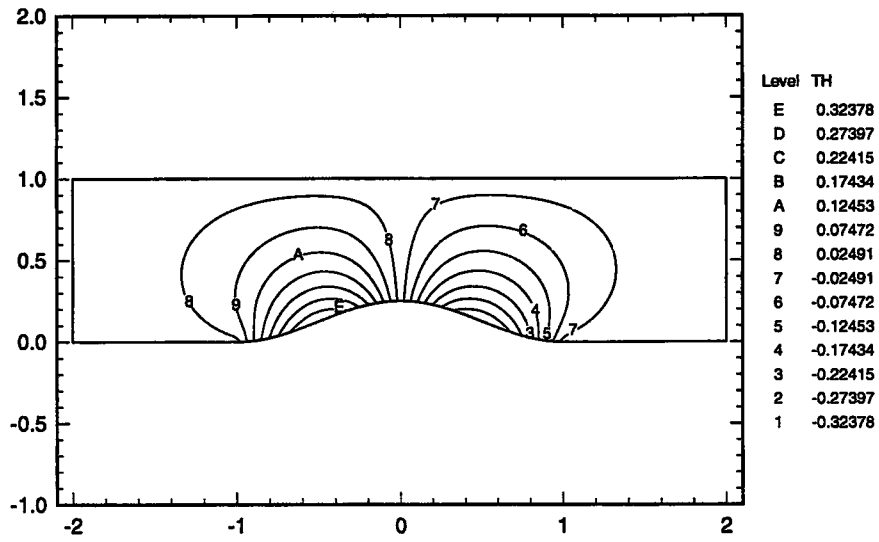


Figure 5.4.8. Flow angle (θ) contours

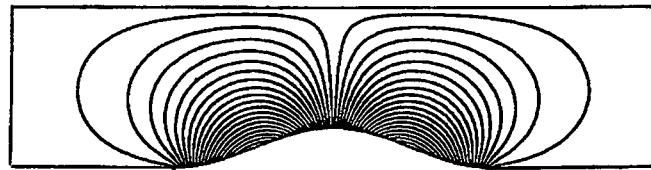


Figure 5.4.9. Flow angle (θ) contours [12]

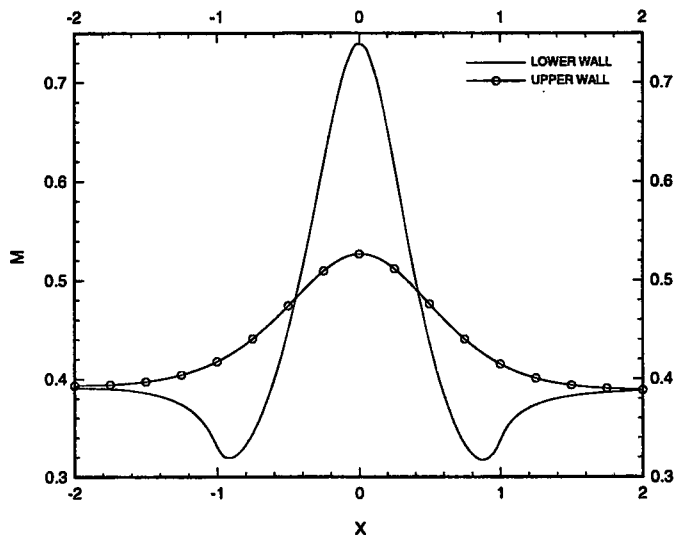


Figure 5.4.10. Mach number distribution along the walls

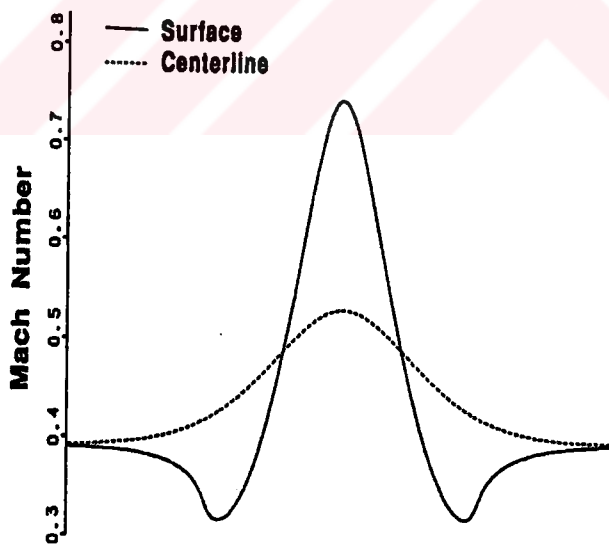


Figure 5.4.11. Mach number distribution along the walls [12]

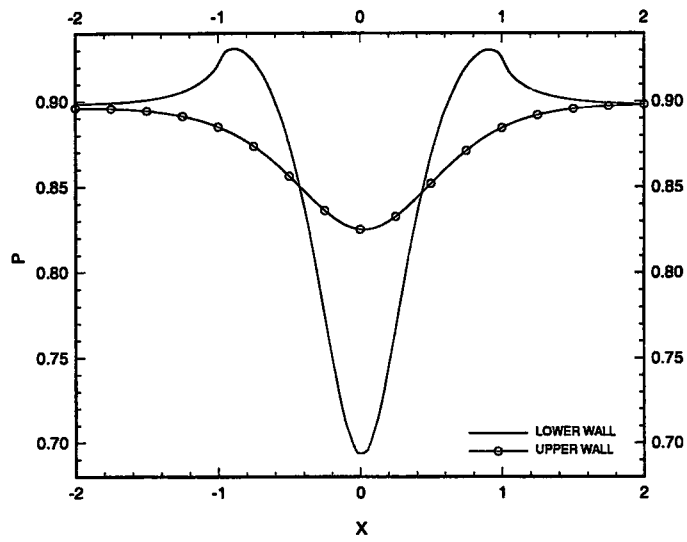


Figure 5.4.12. Pressure distribution along the walls

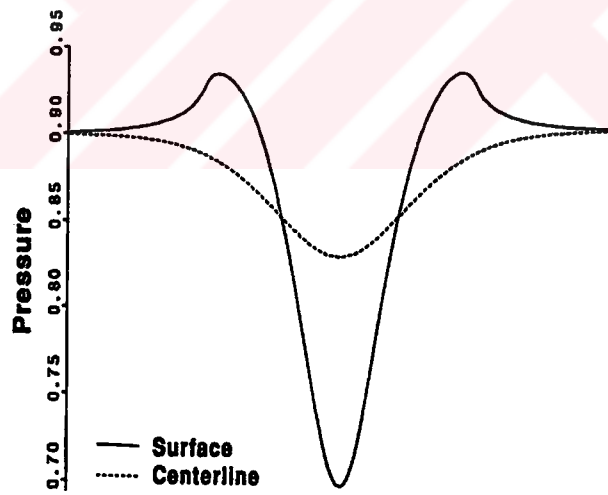


Figure 5.4.13. Pressure distribution along the walls [12]

5.5. SUPERSONIC CONSTANT AREA DUCT (3D)

The complex flow situation in a three-dimensional duct with square cross section was calculated for inlet Mach number of 2. A 21x21x21 grid with cubic cells was used (see Figure 5.5.1).

On both inflow and outflow surfaces zeroth order characteristic boundary conditions for supersonic flow were used. At the inflow boundary, the Riemann variables Q and R , modified entropy S , inlet flow angles θ and ϕ were specified explicitly, whereas at the outflow boundary no physical boundary conditions were specified, but numerical boundary conditions were calculated based on the information defined by the inner flow.

The inlet flow angles were $\theta = -6^\circ$ and $\phi = 6^\circ$. Thus, the flow is expected to be symmetric about the diagonal. Shock correction was not employed for this test case. Thus, isentropic shocks were captured. The solution converges after about 300 iterations with a CFL number of 0.50 (see Figure 5.5.2).

Mach contours at various axial stations along the duct are shown in Figures 5.5.3 to 5.5.6. As expected the flow is symmetric about the diagonal. Oblique shocks forming on the lower wall and right wall are evident by lower Mach numbers compared with that of the free stream flow. Similarly expansion wave forming on the upper wall and left wall are evident by higher Mach numbers compared with that of the free stream flow. The oblique shock surface forming on the lower and side surfaces of the duct interact to create the symmetry about the diagonal. Mach contours on the left and right walls, and bottom and top walls are shown in Figures 5.5.7 to 5.5.10. As a result of diagonal symmetry the contours on $y/h=0$ and that on $z/w=1.0$ are identical. Similarly, the contours on $y/h=1.0$ and that on $z/w=0$ are also identical. Mach contours at three locations along the duct obtained by Verhoff [13] is shown in Figure 5.5.11. Although the shocks obtained by the present method is slightly smeared, the results of both methods are in close agreement.

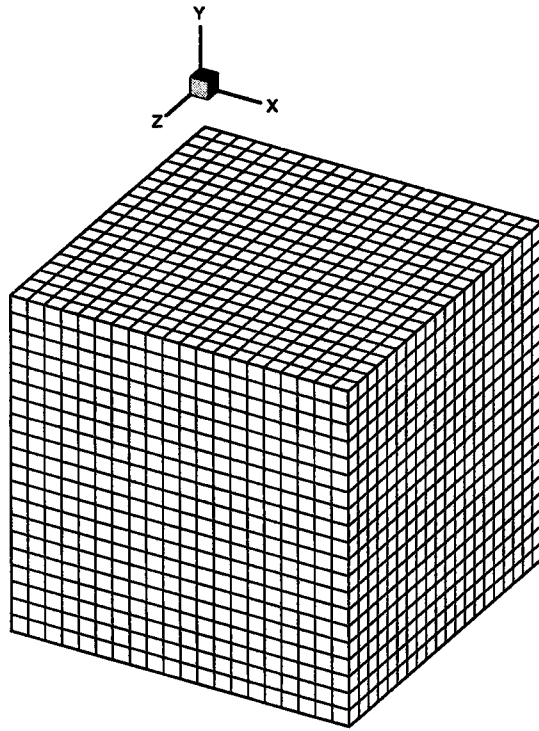


Figure 5.5.1. 21x21x21 computational mesh

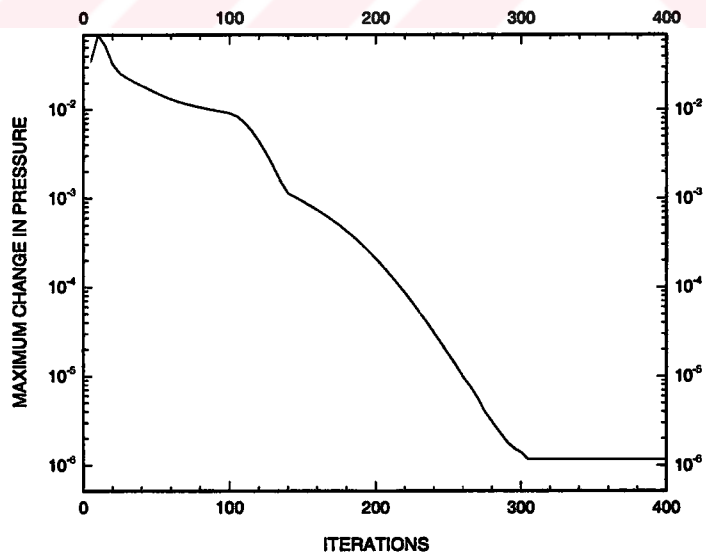


Figure 5.5.2. Convergence history

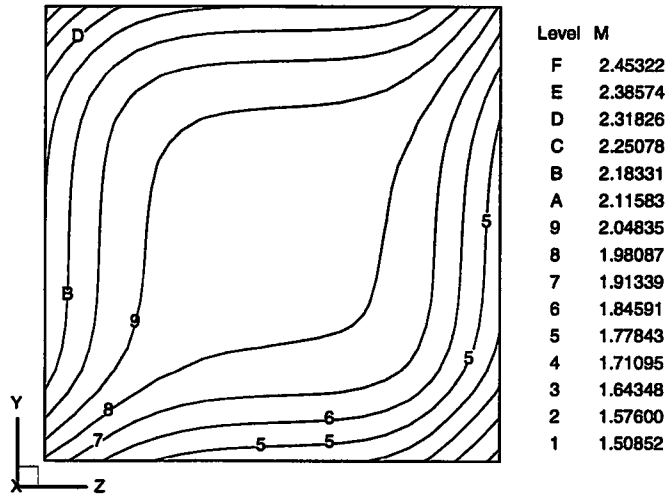


Figure 5.5.3. Mach contours at $x/L=0.20$

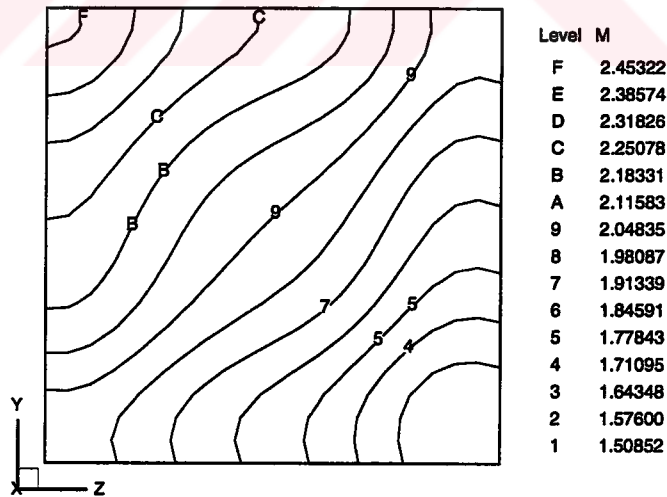


Figure 5.5.4. Mach contours at $x/L=0.45$

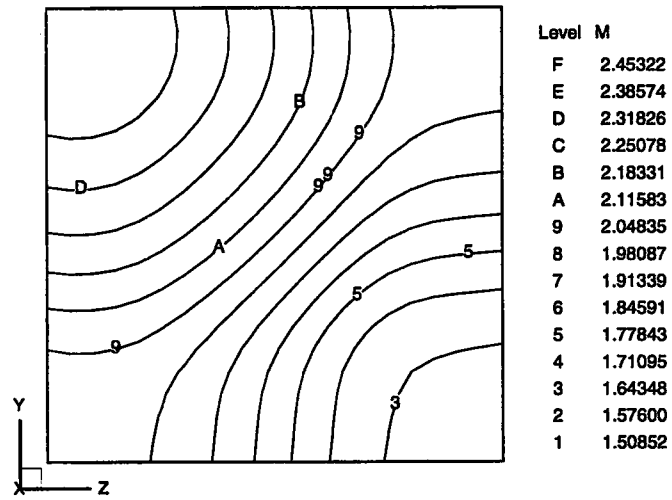


Figure 5.5.5. Mach contours at $x/L=0.70$

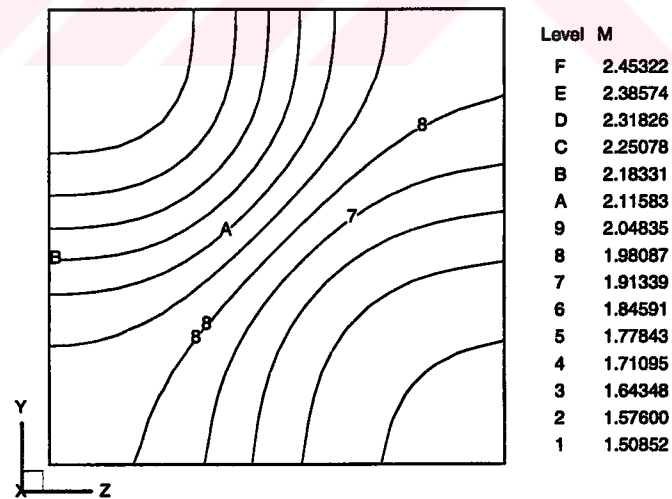


Figure 5.5.6. Mach contours at $x/L=0.95$

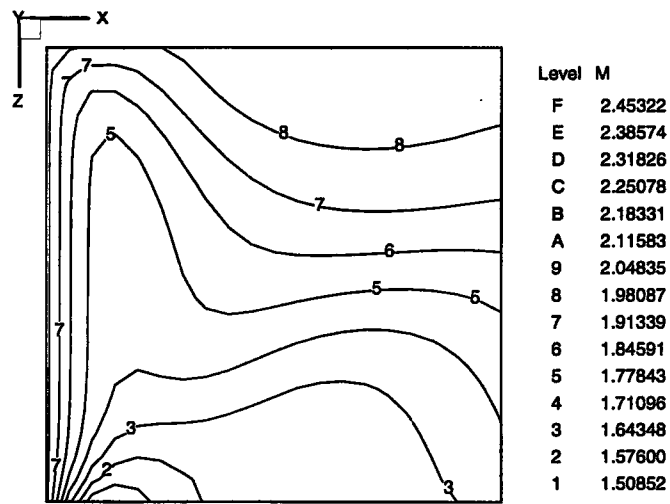


Figure 5.5.7. Mach contours at $y/h=0$

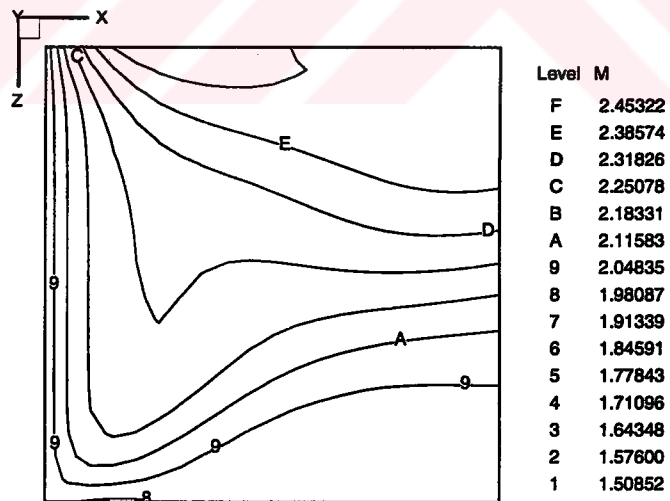


Figure 5.5.8. Mach contours at $y/h=1.0$

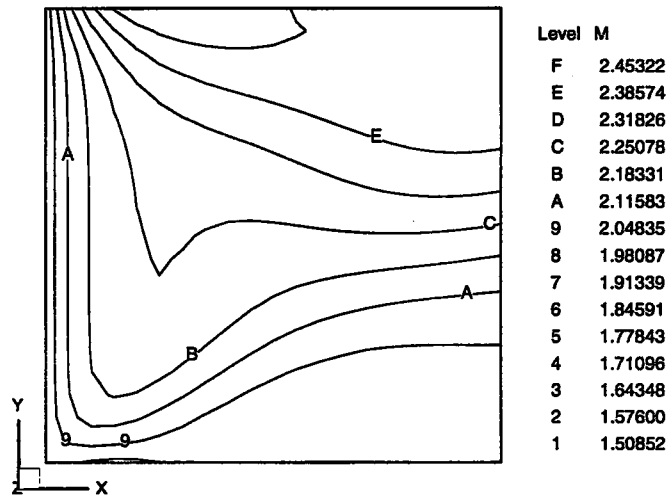


Figure 5.5.9. Mach contours at $z/w=0$

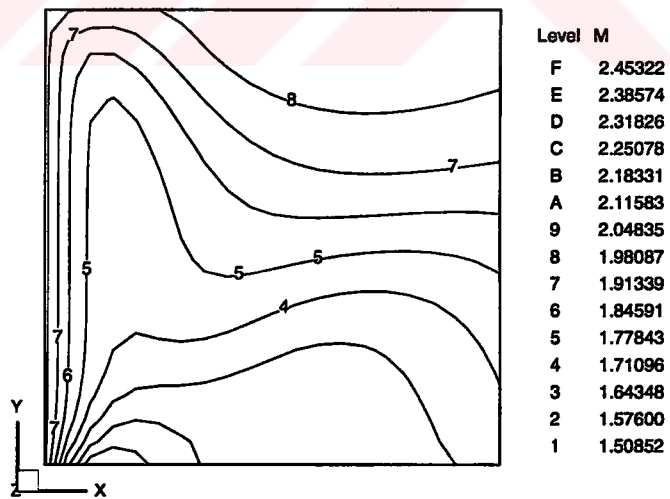


Figure 5.5.10. Mach contours at $z/w=1.0$

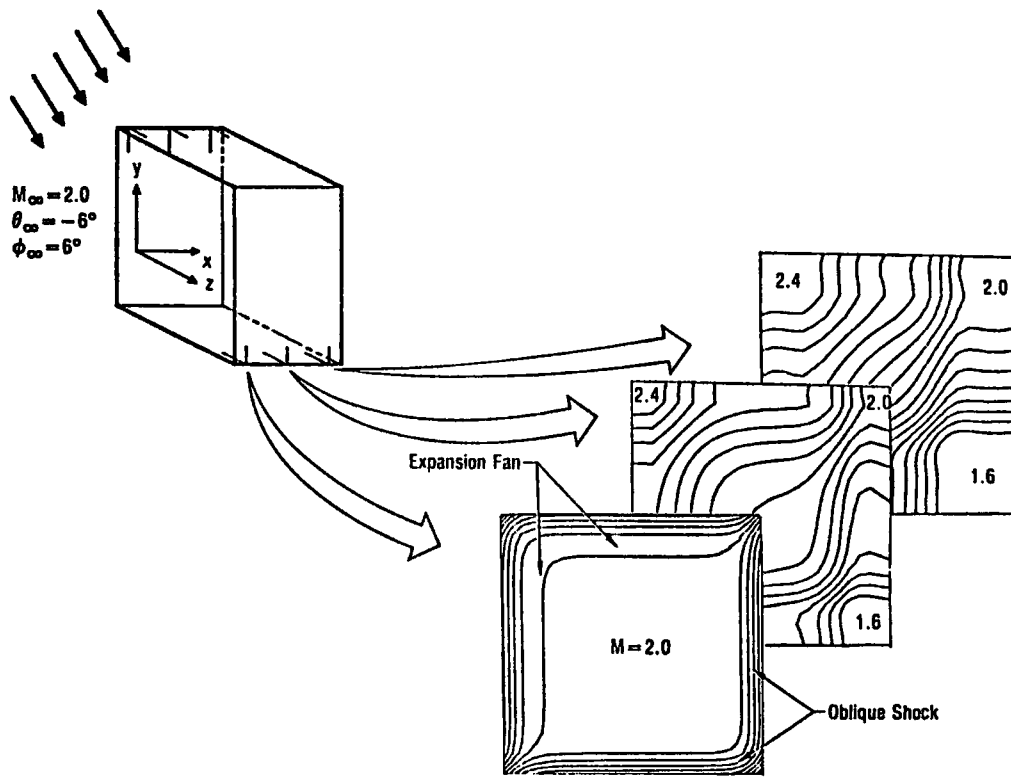


Figure 5.5.11. Mach contours [13]

5.6. 90° BEND (3D)

In order to investigate the applicability of the developed method to three dimensional internal flows with high turning, the flow through a 90° curved duct with a uniform square cross-section was considered. The duct geometry and coordinate system is shown in Figure 5.6.1. The 71x11x11 computational grid used in the solution is shown in Figures 5.6.2.a to 5.6.2.c.

At the inflow boundary a non-uniform subsonic inlet velocity distribution is specified. The inlet velocity profile is given in Figure 5.6.3. Constant pressure is specified as the physical boundary condition at the outflow boundary. The solution converges after about 2000 iterations with a CFL number of 0.2 (See Figure 5.6.4).

Contours of flow angles θ and ϕ , Mach number and pressure at $\alpha = 45^\circ$ plane are shown in Figures 5.6.5 to 5.6.8. Velocity vectors and streamlines at the same plane are shown in Figures 5.6.9 and 5.6.10.

It is known that if a non-uniform inlet velocity distribution is specified at the inlet, secondary velocities and streamwise vorticities develop in the duct while the flow turns with the duct. Secondary flow due to non-uniform inlet condition and duct curvature is formed and it is captured by the present code.

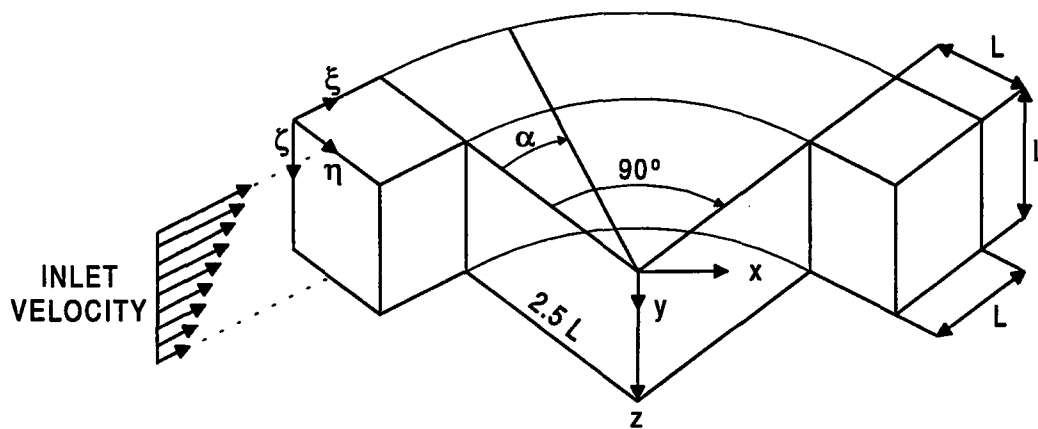


Figure 5.6.1. Duct geometry and coordinate system

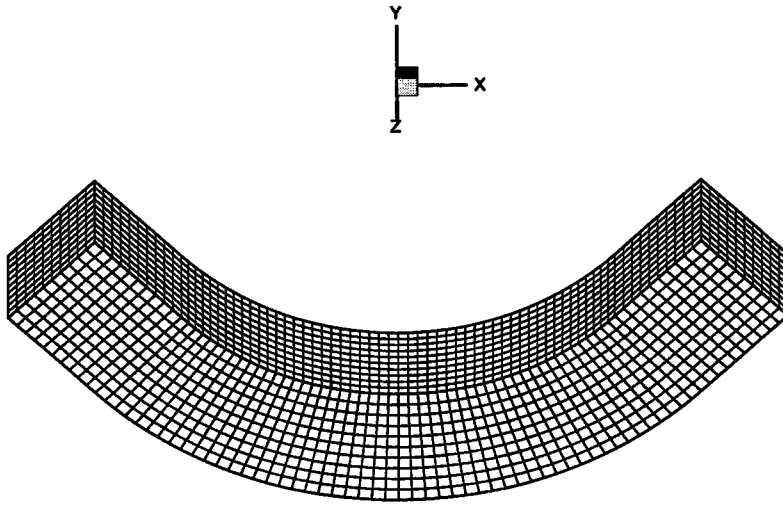


Figure 5.6.2.a. 71x11x11 computational mesh

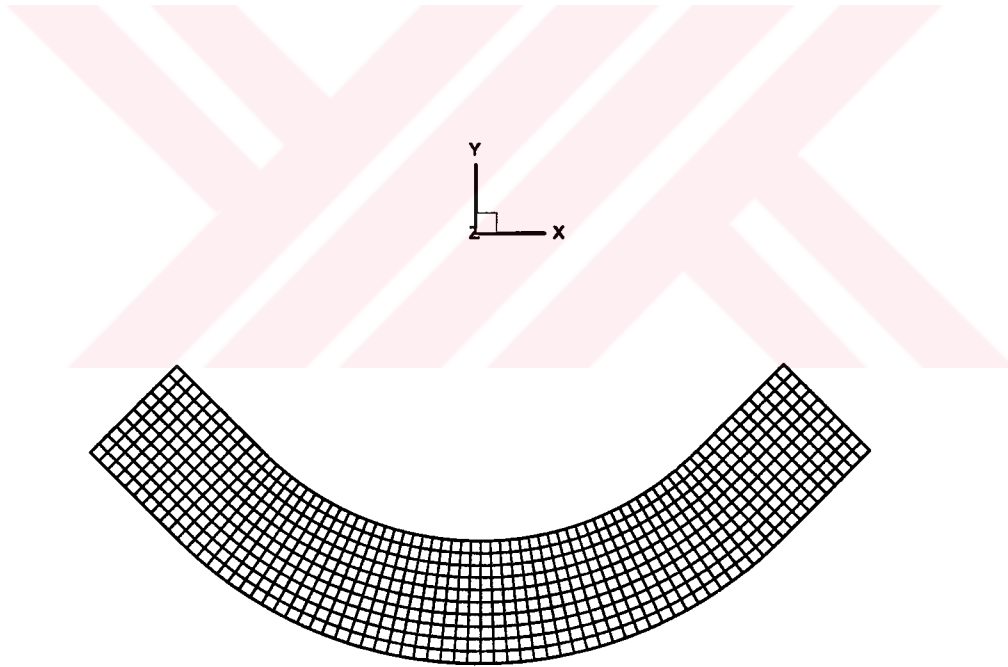


Figure 5.6.2.b. Side view of the 71x11x11 computational mesh

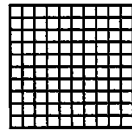
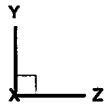


Figure 5.6.2.c. Cross-section of the 71x11x11 computational mesh

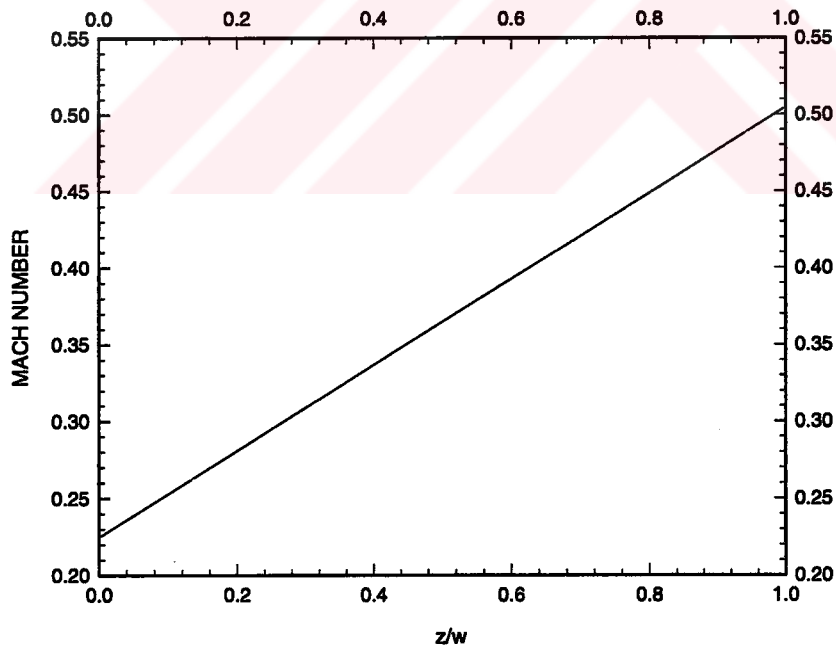


Figure 5.6.3. Inlet velocity profile

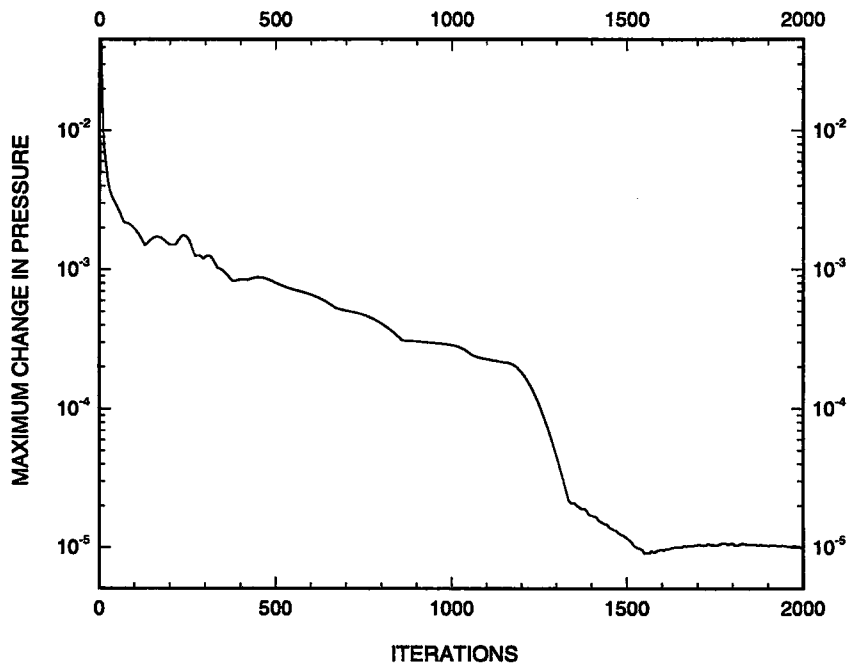


Figure 5.6.4. Convergence history

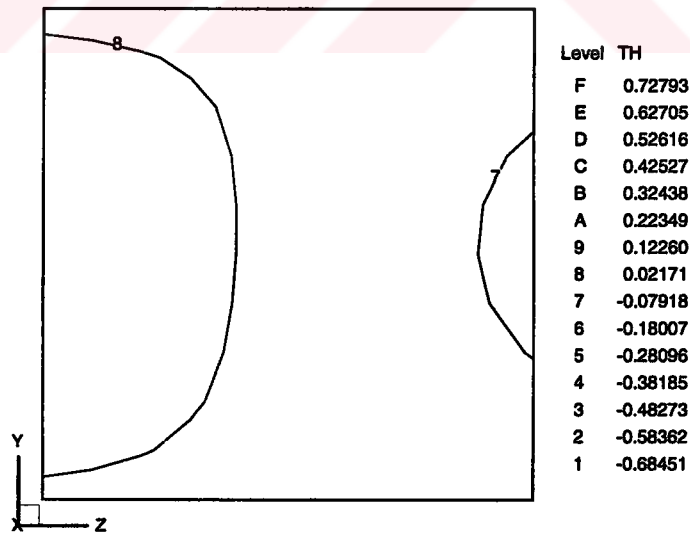


Figure 5.6.5. Flow angle (θ) contours at $\alpha=45^\circ$ plane

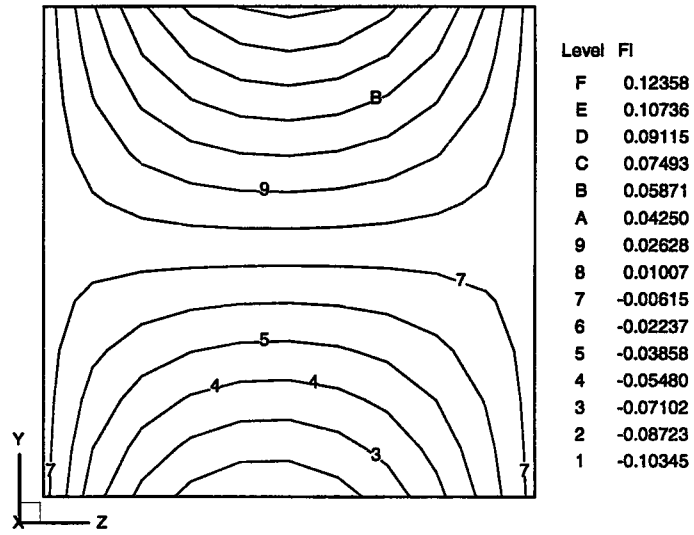


Figure 5.6.6. Flow angle (ϕ) contours at $\alpha=45^\circ$ plane

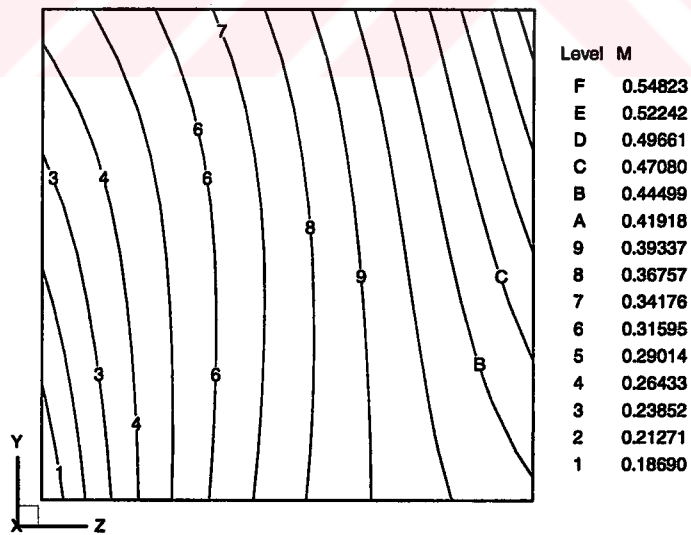


Figure 5.6.7. Mach contours at $\alpha=45^\circ$ plane

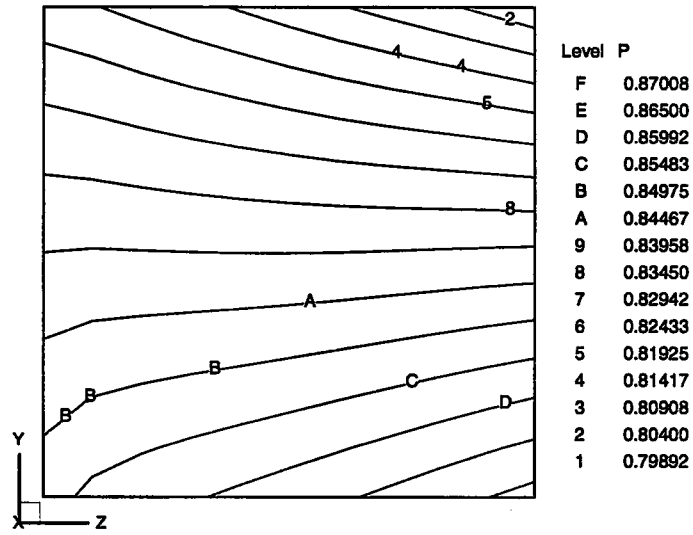


Figure 5.6.8. Pressure contours at $\alpha=45^\circ$ plane

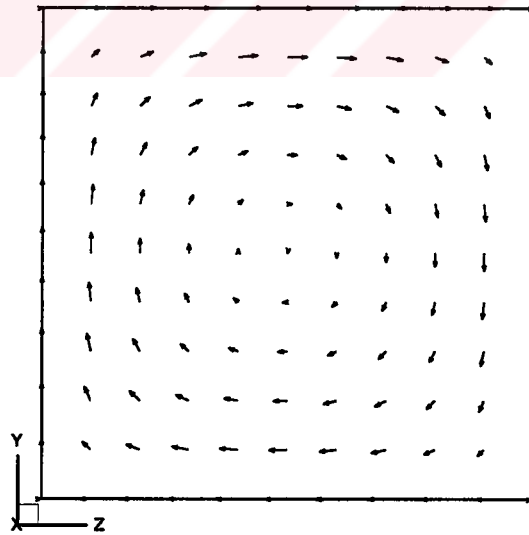


Figure 5.6.9. Velocity vectors at $\alpha=45^\circ$ plane

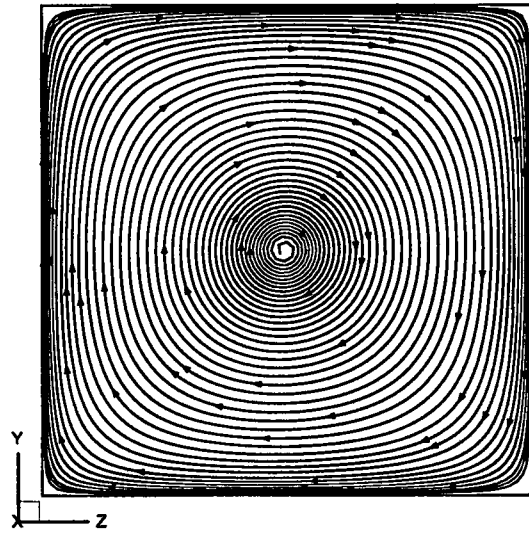


Figure 5.6.10. Streamlines at $\alpha=45^\circ$ plane

CHAPTER 6

CONCLUSION

6.1. SUMMARY OF THE WORK

A numerical solution procedure is developed for the solution of Euler equations. The equations are expressed in local streamline coordinate system and are written in terms of extended Riemann variables. In this form Euler equations become a quasi-one-dimensional system regardless of the number of spatial dimensions, which is in characteristic form. Thus multidimensional flows can be simply treated as quasi-one-dimensional flows using the method of characteristics. The procedure is conceptually simple and versatile.

No numerical dissipation or smoothing is required to assist the solutions.

As long as proper book-keeping can be achieved, multidimensional flows can be solved without any disproportionate difficulty.

Because the procedure uses characteristic-type dependent variables, boundary conditions can be imposed with ease in a physically consistent manner. Characteristic quantities are specified at the inflow or outflow boundaries depending on the direction of the propagation process described by each equation.

The numerical solution procedure is fully explicit. Steady state solutions are obtained by marching in time.

Differencing consistent with the physical direction of wave propagation is employed both along and normal to the streamline directions.

Subsonic, transonic and supersonic flows can be handled equally well.

Since the formulation is not conservative, shock location and shock strength are calculated with slight error unless a specific correction is introduced. Thus, after each iteration a simple shock correction is applied which is based on mass, momentum and energy conservation to remove shock jump errors, and force the shock wave to the correct location.

Shock treatment starts with identifying the intervals or cells where compressions of sufficient strength are located. Using an iterative procedure, the shock velocity is calculated and the unsteady problem is reduced to a steady one with respect to the shock. Normal shock relations are used afterwards to calculate the flow variables downstream of the shock. The shock location is tracked in time and the flow variables at the nodes downstream of the shock are calculated using the shock fitting technique described above.

A classical shock tube problem was solved to test and demonstrate the accuracy of the unsteady wave motion and shock fitting approach. The discontinuity location and the jump in flow parameters across the discontinuities were in close agreement with the analytical solution.

The quasi-one-dimensional transonic flow in a Laval nozzle was solved to show that the steady state solution is accurate and the discontinuity is located in the nozzle correctly.

Shock identification and shock correction studies were performed for two-dimensional flow problems. Cells that contain compressions of sufficient strength were located and marked as having a shock fragment. The shocks were thought to be formed by combinations of small fragments. Shock correction procedure described above was performed for each shock fragment. However, due to difficulties encountered in the bookkeeping of shock locations, shock angles, shock velocities, etc. shock correction was abandoned in the solution of two and three-dimensional flow problems. This simplification resulted in isentropic and smeared shocks.

The two-dimensional inlet flow where the supersonic flow is turned by a ramp was solved to demonstrate that the formation of oblique shock and expansion fan can be

calculated. Although oblique shocks were smeared and isentropic, the flow features obtained were similar to those obtained by another code.

The two-dimensional subsonic flow over a sinusoidal bump was solved to show the capability and accuracy in handling subsonic flows. Symmetry about the throat was demonstrated which indicates the accuracy of the method.

Three-dimensional flow solving capability was demonstrated by solving supersonic flow in a constant area duct and subsonic flow in a 90° bend.

In supersonic flow in the constant area duct, oblique shocks and expansion fans were formed due to inlet flow angles. The results were compared with that of another numerical solution, although shocks were slightly smeared the results of both codes were in close agreement.

In subsonic flow in 90° bend secondary velocity and streamwise vorticity development were predicted due to a non-uniform inlet velocity distribution and high turning of the flow.

Subsonic flow in an annular cascade was attempted. Due to difficulties in bookkeeping and the skewness of the available grid the orientation of the streamlines with respect to the grid could not be evaluated properly and convergent solutions could not be obtained.

6.2. FUTURE WORK

It is recommended that shock tracking and shock correction capability in two and three-dimensional flows be added to the present code.

It is also recommended that the boundary conditions should be improved. First or second order characteristic boundary conditions should be introduced, so that the need for placing far field boundaries far away from the main region of interest can be eliminated. Thus, grids with smaller number of elements can be used and shorter execution times can be achieved.

Currently, the equations of motion are integrated by a first order algorithm. Time integration algorithm can be improved to higher accuracy order.

External flow solving capability should be gained additional to the internal flow solving capability.

The method can be coupled with a boundary layer solver, so that more realistic solutions can be obtained for flows in ducts or over bodies.

Finally, the method can be evaluated for the solution of the Navier-Stokes equations.

REFERENCES

- [1] Critical Technologies Plan for the Committees on Armed Services United States Congress, The Department of Defence, 15 March 1990.
- [2] Verhoff, A., O'Neil, P.J., "A Natural Formulation for Numerical Solution of the Euler Equations", AIAA Paper No. 84-0163, January 1984.
- [3] Verhoff, A., O'Neil, P.J., Hopping, B., "Euler Solutions for Airfoils Using the QAZ1D Formulation", Proc. of the AIAA 18th Fluid Dynamics, Plasma Dynamics and Laser Conference, Cincinnati, Ohio, July 16-18, 1985.
- [4] Verhoff, A., Stookesberry, D., "Prediction of Inviscid Supersonic/Hypersonic Aircraft Flowfields", 17th Congress of International Council of the Aeronautical Sciences, September 1990.
- [5] Verhoff, A., Stookesberry, D., Hopping, B., Michal, T., "Supersonic/Hypersonic Euler Flowfield Prediction Method for Aircraft Configurations", Proc. of the 4th Symposium on Numerical and Physical Aspects of Aerodynamic Flows, Long Beach, California, January 16-19, 1989.
- [6] Verhoff, A., O'Neil, P.J., "Accurate, Efficient Prediction Method for Supersonic/Hypersonic Inviscid Flow", AIAA Paper No. 87-1165, June 1987.
- [7] Agrawal, S., Vermeland, R.E., Verhoff, A., Lowrie, R.B., "Euler Transonic Solutions Over Finite Wings", AIAA Paper No. 88-0009, January 1988.
- [8] Hirsch, C., Verhoff, A., "Far-Field Numerical Boundary Conditions for Internal and Cascade Flow Computations", AIAA Paper No. 89-1943, June 1989.
- [9] Verhoff, A., "Second Order Far Field Computational Boundary Conditions for Inviscid Duct Flow Problems", Naval Post Graduate School Report No. NPS67-90-001CR, March 1990.
- [10] Verhoff, A., Stookesberry, D., Agrawal, S., "Far-Field Computational Boundary Conditions for External Flow Problems", AIAA Paper No. 91-0630, January 1991.

- [11] Verhoff, A., Stookesberry, D., Agrawal, S, "Far-Field Computational Boundary Conditions for Two-Dimensional External Flow Problems", AIAA Journal, Vol. 30, No. 11, November 1992, pp.2585-2594.
- [12] Verhoff, A., Stookesberry, D., "Second-Order, Far-Field Computational Boundary Conditions for Inviscid Duct Flow Problems", AIAA Journal, Vol. 30, No. 5, May 1992, pp.1268-1276.
- [13] Verhoff, A., O'Neil, P.J., "A Natural Formulation for Numerical Solution of the Euler Equations", McDonnell Douglas Report.
- [14] Salacka, T.F., "Review, Implementation and Test of the QAZ1D Computational Method with a View to Wave Rotor Applications", M.S. Thesis, Naval Postgraduate School. Monterey, California, December 1985.
- [15] Johnston, D.T., "Further Development of a One-Dimensional Unsteady Euler Code for Wave Rotor Applications", M.S. Thesis, Naval Postgraduate School. Monterey, California, March 1987.
- [16] Moretti, G., DiPiano, M.T., "An Improved Lambda-Scheme for One-Dimensional Flows", NASA Contractor Report 3712, 1983.
- [17] Çakıroğlu, M., "Multiblock Grid Generation for Missile Configurations", Ph.D. Thesis in Mechanical Engineering, Middle East Technical University, March 1997.
- [18] Verhoff, A., Stookesberry, D., Hopping, B., Michal, T., "Supersonic/Hypersonic Euler Flowfield Prediction Method for Aircraft Configurations", Progress in Astronautics and Aeronautics, Vol. 125, Applied Computational Aerodynamics, Chapter 23, pp.839-861.
- [19] Zucrow, M.J., Hoffman, J.D., "Gas Dynamics, Multidimensional Flows", Volume II, Robert E. Krieger Publishing Company, Malabar, 1985.
- [20] Shapiro, A.H., "The Dynamics and Thermodynamics of Compressible Fluid Flow", Volume I, The Ronald Press Company, New York, 1953.
- [21] Anderson, D.A., Tannehill, J.C. Pletcher, R.H., "Computational Fluid Mechanics and Heat Transfer", Hemisphere Publishing Corporation, New York, 1984.
- [22] Hirsch, C., "Numerical Computation of Internal and External Flows", Volume I, John Wiley and Sons, New York, 1988.
- [23] Hirsch, C., "Numerical Computation of Internal and External Flows", Volume II, John Wiley and Sons, New York, 1990.
- [24] Hoffman, K.A., "Computational Fluid Dynamics for Engineers", A Publication of Engineering Education System, Austin, Texas, 1989.

- [25] Wendt, J.F. (editor), "Computational Fluid Dynamics, An Introduction", Springer-Verlag, New York, 1992
- [26] Slooff, J.W., Schmidt, W. (editor), "Computational Aerodynamics Based on the Euler Equations", AGARD-AG-325.
- [27] Smolderen, J.J. (editor), "Numerical Methods in Fluid Dynamics", AGARD-LS-48, 1971.
- [28] Anderson, J.D., "Modern Compressible Flow with Historical Perspective", McGraw-Hill Publishing Company, Singapore, 1990.
- [29] Vygodsky, M., "Mathematical Handbook, Higher Mathematics", Mir Publishers, Moscow, 1987.
- [30] Steger, J.L., Warming, R.F., "Flux Vector Splitting of the Inviscid Gasdynamic Equations with Application to Finite-Difference Methods", Journal of Computational Physics, Vol. 40, No. 2, April 1981, pp. 263-293.



APPENDIX A:

EULER EQUATIONS EXPRESSED IN NATURAL STREAMLINE COORDINATE SYSTEM

One-dimensional

$$Q_t + (q+a) Q_s = -\frac{\gamma-1}{2} a \left(S - \frac{2}{\gamma-1}\right) \frac{\partial}{\partial s} \left(q - \frac{2}{\gamma-1} a\right) \quad (\text{A.1})$$

$$R_t + (q-a) R_s = +\frac{\gamma-1}{2} a \left(S - \frac{2}{\gamma-1}\right) \frac{\partial}{\partial s} \left(q + \frac{2}{\gamma-1} a\right) \quad (\text{A.2})$$

$$S_t + q S_s = 0 \quad (\text{A.3})$$

Quasi-one-dimensional

$$Q_t + (q+a) Q_s = -\frac{\gamma-1}{2} a \left(S - \frac{2}{\gamma-1}\right) \frac{\partial}{\partial s} \left(q - \frac{2}{\gamma-1} a\right) - \frac{\gamma-1}{2} q a S \left(\frac{1}{A} \frac{\partial A}{\partial s}\right) \quad (\text{A.4})$$

$$R_t + (q-a) R_s = +\frac{\gamma-1}{2} a \left(S - \frac{2}{\gamma-1}\right) \frac{\partial}{\partial s} \left(q + \frac{2}{\gamma-1} a\right) + \frac{\gamma-1}{2} q a S \left(\frac{1}{A} \frac{\partial A}{\partial s}\right) \quad (\text{A.5})$$

$$S_t + q S_s = 0 \quad (\text{A.6})$$

Two-dimensional

$$Q_t + (q+a) Q_s = -\frac{\gamma-1}{2} a \left(S - \frac{2}{\gamma-1}\right) \frac{\partial}{\partial s} \left(q - \frac{2}{\gamma-1} a\right) - \frac{\gamma-1}{2} q a S \theta_n \quad (\text{A.7})$$

$$R_t + (q-a) R_s = +\frac{\gamma-1}{2} a \left(S - \frac{2}{\gamma-1}\right) \frac{\partial}{\partial s} \left(q + \frac{2}{\gamma-1} a\right) + \frac{\gamma-1}{2} q a S \theta_n \quad (\text{A.8})$$

$$S_t + q S_s = 0 \quad (\text{A.9})$$

$$\theta_t + q \theta_s = -\frac{a^2}{\gamma q} P_n \quad (\text{A.10})$$

Three-dimensional

$$Q_t + (q+a) Q_s = -\frac{\gamma-1}{2} a \left(S - \frac{2}{\gamma-1}\right) \frac{\partial}{\partial s} \left(q - \frac{2}{\gamma-1} a\right) - \frac{\gamma-1}{2} q a S (\theta_n + \phi_m \cos\theta) \quad (\text{A.11})$$

$$R_t + (q-a) R_s = +\frac{\gamma-1}{2} a \left(S - \frac{2}{\gamma-1}\right) \frac{\partial}{\partial s} \left(q + \frac{2}{\gamma-1} a\right) + \frac{\gamma-1}{2} q a S (\theta_n + \phi_m \cos\theta) \quad (\text{A.12})$$

$$S_t + q S_s = 0 \quad (\text{A.13})$$

$$\theta_t + q \theta_s = -\frac{a^2}{\gamma q} P_n \quad (\text{A.14})$$

$$\phi_t + q \phi_s = -\frac{a^2}{\gamma q \cos\theta} P_m \quad (\text{A.15})$$

where, velocity magnitude and speed of sound are denoted by q and a , respectively, and P is the logarithm of pressure, Q and R are the extended Riemann variables, S is the entropy, θ and ϕ are the flow. Time is denoted by t while distances along and normal to the streamline direction are denoted by the vectors s , m and n , respectively.

APPENDIX B:

SPLITTING OF MATRICES [4]

The QAZ1D equations in matrix form are,

$$\frac{\partial}{\partial t}\{F\} + [A] \frac{\partial}{\partial s}\{F\} + [B] \frac{\partial}{\partial n}\{F\} + [C] \frac{\partial}{\partial m}\{F\} = \{0\} \quad (B.1)$$

where

$$\{F\} = \{Q \ R \ \theta \ \phi\}^T \quad (B.2)$$

and [A] is the diagonal matrix of characteristic velocities,

$$[A] = \begin{bmatrix} q+a & 0 & 0 & 0 \\ 0 & q-a & 0 & 0 \\ 0 & 0 & q & 0 \\ 0 & 0 & 0 & q \end{bmatrix} \quad (B.3)$$

Since the [A] matrix is composed of eigenvalues along the diagonal, it distinguishes upstream from downstream characteristics by the sign of the eigenvalue. The [B] and [C] matrices are written as

$$[B] = \begin{bmatrix} 0 & 0 & qa & 0 \\ 0 & 0 & -qa & 0 \\ \frac{a}{2q} & -\frac{a}{2q} & 0 & 0 \\ 0 & 0 & 0 & 0 \end{bmatrix} \quad (B.4)$$

$$[C] = \begin{bmatrix} 0 & 0 & 0 & qa \cos q \\ 0 & 0 & 0 & qa \cos q \\ 0 & 0 & 0 & 0 \\ \frac{a}{2q \cos q} & -\frac{a}{2q \cos q} & 0 & 0 \end{bmatrix} \quad (B.5)$$

In order to distinguish directions of propagation normal to the local streamline direction (eg. along n), the [B] matrix is transformed according to

$$[B] = [X]^{-1}[\lambda_B][X] \quad (B.6)$$

where

$$[\lambda_B] = \begin{bmatrix} 0 & 0 & 0 & 0 \\ 0 & 0 & 0 & 0 \\ 0 & 0 & -a & 0 \\ 0 & 0 & 0 & a \end{bmatrix} \quad (\text{B.7})$$

The $[\lambda_B]$ matrix is composed of eigenvalues normal to the streamline direction. Using equations B.4, B.6 and B.7 the matrix $[X]$ is determined and the $[B]$ matrix is split into two parts as

$$[B] = [B^+] + [B^-] \quad (\text{B.8})$$

where

$$[B^+] = \begin{bmatrix} \frac{a}{4} & \frac{-a}{4} & 0 & \frac{q a}{2} \\ \frac{-a}{4} & \frac{a}{4} & 0 & \frac{q a}{2} \\ 0 & 0 & 0 & 0 \\ \frac{a}{4q} & \frac{-a}{4q} & 0 & \frac{a}{2} \end{bmatrix} \quad (\text{B.9})$$

$$[B^-] = \begin{bmatrix} \frac{-a}{4} & \frac{a}{4} & 0 & \frac{q a}{2} \\ \frac{a}{4} & \frac{-a}{4} & 0 & \frac{-q a}{2} \\ 0 & 0 & 0 & 0 \\ \frac{a}{4q} & \frac{-a}{4q} & 0 & \frac{-a}{2} \end{bmatrix} \quad (\text{B.10})$$

Similarly, in order to distinguish directions of propagation along the m coordinate direction, the matrix $[C]$ is split as

$$[C] = [C^+] + [C^-] \quad (\text{B.11})$$

where

$$[C^+] = \begin{bmatrix} \frac{a}{4} & \frac{-a}{4} & 0 & \frac{q a \cos\theta}{2} \\ \frac{-a}{4} & \frac{a}{4} & 0 & \frac{-q a \cos\theta}{2} \\ 0 & 0 & 0 & 0 \\ \frac{a}{4q \cos\theta} & \frac{-a}{4q \cos\theta} & 0 & \frac{a}{2} \end{bmatrix} \quad (\text{B.12})$$

$$[C^-] = \begin{bmatrix} \frac{-a}{4} & \frac{a}{4} & 0 & \frac{q a \cos\theta}{2} \\ \frac{a}{4} & \frac{-a}{4} & 0 & \frac{-q a \cos\theta}{2} \\ 0 & 0 & 0 & 0 \\ \frac{a}{4q \cos\theta} & \frac{-a}{4q \cos\theta} & 0 & \frac{-a}{2} \end{bmatrix} \quad (B.13)$$

Here $[B^+]$, $[B^-]$, $[C^+]$ and $[C^-]$ each have a unique direction of propagation corresponding to the positive and negative eigenvalue, respectively. The system of equations for 3D isentropic flow thus becomes

$$Q_t + (q+a) Q_s = -\frac{a}{4} \left[\frac{\partial}{\partial n} (Q-R)^+ - \frac{\partial}{\partial n} (Q-R)^- + \frac{\partial}{\partial m} (Q-R)^+ - \frac{\partial}{\partial m} (Q-R)^- \right] \\ - \frac{q a}{2} \left[\left(\frac{\partial \theta^+}{\partial n} + \frac{\partial \theta^-}{\partial n} \right) + \cos\theta \left(\frac{\partial \phi^+}{\partial m} + \frac{\partial \phi^-}{\partial m} \right) \right] \quad (B.14)$$

$$R_t + (q-a) R_s = \frac{a}{4} \left[\frac{\partial}{\partial n} (Q-R)^+ - \frac{\partial}{\partial n} (Q-R)^- + \frac{\partial}{\partial m} (Q-R)^+ - \frac{\partial}{\partial m} (Q-R)^- \right] \\ + \frac{q a}{2} \left[\left(\frac{\partial \theta^+}{\partial n} + \frac{\partial \theta^-}{\partial n} \right) + \cos\theta \left(\frac{\partial \phi^+}{\partial m} + \frac{\partial \phi^-}{\partial m} \right) \right] \quad (B.15)$$

$$\theta_t + q \theta_s = -\frac{a}{4q} \left[\frac{\partial}{\partial n} (Q-R)^+ + \frac{\partial}{\partial n} (Q-R)^- \right] - \frac{a}{2} \left(\frac{\partial \theta^+}{\partial n} - \frac{\partial \theta^-}{\partial n} \right) \quad (B.16)$$

$$\phi_t + q \phi_s = -\frac{a}{4q \cos\theta} \left[\frac{\partial}{\partial m} (Q-R)^+ + \frac{\partial}{\partial m} (Q-R)^- \right] - \frac{a}{2} \left(\frac{\partial \phi^+}{\partial m} - \frac{\partial \phi^-}{\partial m} \right) \quad (B.17)$$

where, $\frac{\partial}{\partial n}(\)^+$ and $\frac{\partial}{\partial n}(\)^-$ are one sided-derivatives along n, corresponding to the positive and negative eigenvalues normal to the streamline direction, respectively.

Along m, $\frac{\partial}{\partial m}(\)^+$ and $\frac{\partial}{\partial m}(\)^-$ derivatives have similar meaning.

The splitting of the matrices allows numerical differencing normal to the streamline direction in a manner consistent with the physical direction of wave propagation.

APPENDIX C:

DIFFERENCE EQUATIONS

Table C.1 Finite Difference Equations Used in Calculation of $\frac{\partial w}{\partial s}$, $\frac{\partial w}{\partial n}$ and $\frac{\partial w}{\partial m}$

	$\frac{\partial w}{\partial \xi}$	$\frac{\partial w}{\partial \eta}$	$\frac{\partial w}{\partial \zeta}$
$\left. \frac{\partial w}{\partial s} \right)_F$	$(w_{i+1} - w_i)$	$(w_{j+1} - w_j)$ if $\theta_p > \theta_i^F$ $(w_j - w_{j-1})$ if $\theta_p < \theta_i^F$ $0.5(w_{j+1} - w_{j-1})$ if $\theta_p = \theta_i^F$	$(w_{k+1} - w_k)$ if $\phi > \phi_i^F$ $(w_k - w_{k-1})$ if $\phi < \phi_i^F$ $0.5(w_{k+1} - w_{k-1})$ if $\phi = \phi_i^F$
$\left. \frac{\partial w}{\partial s} \right)_B$	$(w_i - w_{i-1})$	$(w_j - w_{j-1})$ if $\theta_p > \theta_i^B$ $(w_{j+1} - w_j)$ if $\theta_p < \theta_i^B$ $0.5(w_{j+1} - w_{j-1})$ if $\theta_p = \theta_i^B$	$(w_k - w_{k-1})$ if $\phi > \phi_i^B$ $(w_{k+1} - w_k)$ if $\phi < \phi_i^B$ $0.5(w_{k+1} - w_{k-1})$ if $\phi = \phi_i^B$
$\left. \frac{\partial w}{\partial n} \right)_F$	$(w_i - w_{i-1})$ if $(\theta + \frac{\pi}{2})_p > \theta_j^F$ $(w_{i+1} - w_i)$ if $(\theta + \frac{\pi}{2})_p < \theta_j^F$ $0.5(w_{i+1} - w_{i-1})$ if $(\theta + \frac{\pi}{2})_p = \theta_j^F$	$(w_{j+1} - w_j)$	$(w_{k+1} - w_k)$ if $\phi > \phi_i^F$ and $\theta < 0$ $(w_{k+1} - w_k)$ if $\phi < \phi_i^F$ and $\theta > 0$ $(w_k - w_{k-1})$ if $\phi < \phi_i^F$ and $\theta < 0$ $(w_k - w_{k-1})$ if $\phi > \phi_i^F$ and $\theta > 0$ $0.5(w_{k+1} - w_{k-1})$ else
$\left. \frac{\partial w}{\partial n} \right)_B$	$(w_{i+1} - w_i)$ if $(\theta + \frac{\pi}{2})_p > \theta_j^B$ $(w_i - w_{i-1})$ if $(\theta + \frac{\pi}{2})_p < \theta_j^B$ $0.5(w_{i+1} - w_{i-1})$ if $(\theta + \frac{\pi}{2})_p = \theta_j^B$	$(w_j - w_{j-1})$	$(w_k - w_{k-1})$ if $\phi > \phi_i^F$ and $\theta < 0$ $(w_k - w_{k-1})$ if $\phi < \phi_i^F$ and $\theta > 0$ $(w_{k+1} - w_k)$ if $\phi < \phi_i^F$ and $\theta < 0$ $(w_{k+1} - w_k)$ if $\phi > \phi_i^F$ and $\theta > 0$ $0.5(w_{k+1} - w_{k-1})$ else
$\left. \frac{\partial w}{\partial m} \right)_F$	$(w_i - w_{i-1})$ if $\phi + \frac{\pi}{2} > \phi_k^F$ $(w_{i+1} - w_i)$ if $\phi + \frac{\pi}{2} < \phi_k^F$ $0.5(w_{i+1} - w_{i-1})$ if $\phi + \frac{\pi}{2} = \phi_k^F$	$0.5(w_{j+1} - w_{j-1})$	$(w_{k+1} - w_k)$
$\left. \frac{\partial w}{\partial m} \right)_B$	$(w_{i+1} - w_i)$ if $\phi + \frac{\pi}{2} > \phi_k^B$ $(w_i - w_{i-1})$ if $\phi + \frac{\pi}{2} < \phi_k^B$ $0.5(w_{i+1} - w_{i-1})$ if $\phi + \frac{\pi}{2} = \phi_k^B$	$0.5(w_{j+1} - w_{j-1})$	$(w_k - w_{k-1})$

In Table C.1, F and B stand for forward and backward differencing, respectively. The definitions of angles ϕ_i^F , ϕ_i^B , ϕ_k^F , ϕ_k^B , θ_i^F , θ_i^B , θ_j^F and θ_j^B are given below:

$$\phi_i^F = a \tan\left(\frac{Z_{i+1} - Z_i}{X_{i+1} - X_i}\right) \quad (C.1)$$

$$\phi_i^B = a \tan\left(\frac{Z_i - Z_{i-1}}{X_i - X_{i-1}}\right) \quad (C.2)$$

$$\phi_k^F = a \tan\left(\frac{Z_{k+1} - Z_k}{X_{k+1} - X_k}\right) \quad (C.3)$$

$$\phi_k^B = a \tan\left(\frac{Z_k - Z_{k-1}}{X_k - X_{k-1}}\right) \quad (C.4)$$

$$\theta_i^F = a \tan\left(\frac{Y_{i+1} - Y_i}{X_{i+1} - X_i}\right) \quad (C.5)$$

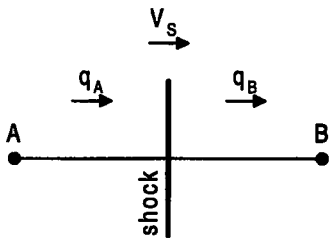
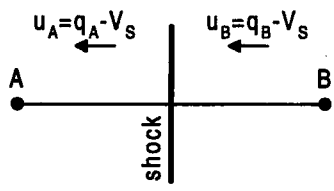
$$\theta_i^B = a \tan\left(\frac{Y_i - Y_{i-1}}{X_i - X_{i-1}}\right) \quad (C.6)$$

$$\theta_j^F = a \tan\left(\frac{Y_{j+1} - Y_j}{X_{j+1} - X_j}\right) \quad (C.7)$$

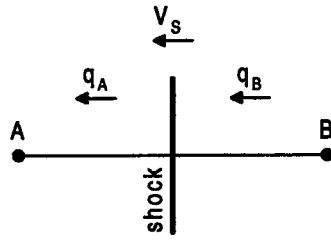
$$\theta_j^B = a \tan\left(\frac{Y_j - Y_{j-1}}{X_j - X_{j-1}}\right) \quad (C.8)$$

APPENDIX D:

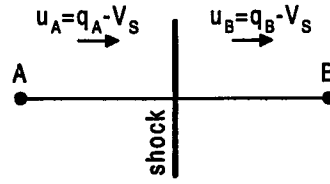
SHOCK EQUATIONS [14]

High Pressure on the Left	
	
Unsteady	Steady
Riemann Variable Change (Approximate)	
$\frac{Q_A - Q_B}{a_B} \approx -2.7574 + 3.1573 W - 0.2863 W^2 \quad (D.1)$	
Riemann Variable Change	
$\frac{Q_A - Q_B}{a_B} = \frac{2(W^2 - 1)}{(\gamma + 1)W} + \frac{2}{\gamma - 1} \cdot \left(\frac{a_A}{a_B} - 1\right) - \frac{a_A}{a_B} \cdot \frac{1}{\gamma(\gamma - 1)} \ln \left[\left[\frac{2\gamma}{\gamma + 1} W^2 - \frac{\gamma - 1}{\gamma + 1} \right] \left[\frac{(\gamma - 1)W^2 + 2}{(\gamma + 1)W^2} \right]^\gamma \right] \quad (D.2)$	
Relative Incoming Mach Number	
$W = -\frac{u_B}{a_B} = -\frac{(q_B - V_s)}{a_B} \quad (D.3)$	
Speed of Sound Ratio	
$\frac{a_A}{a_B} = \frac{1}{(\gamma + 1)W} \left[2(\gamma - 1) \left[1 + \frac{\gamma - 1}{2} W^2 \right] \left[\frac{2\gamma}{\gamma - 1} W^2 - 1 \right] \right]^{\frac{1}{2}} \quad (D.4)$	
Velocity Change	
$\frac{q_A - q_B}{a_B} = \frac{2(W^2 - 1)}{(\gamma + 1)W} \quad (D.5)$	
Entropy Change	
$S_A - S_B = -\frac{1}{\gamma(\gamma - 1)} \ln \left[\frac{2\gamma W^2 - \gamma + 1}{\gamma + 1} \right] - \frac{1}{\gamma - 1} \ln \left[\frac{(\gamma - 1)W^2 + 2}{(\gamma + 1)W^2} \right] \quad (D.6)$	

High Pressure on the Right



Unsteady



Steady

Riemann Variable Change (Approximate)

$$\frac{R_A - R_B}{a_A} \approx -2.7574 + 3.1573 W - 0.2863 W^2 \quad (D.7)$$

Riemann Variable Change

$$\begin{aligned} \frac{R_A - R_B}{a_A} = & \frac{2(W^2 - 1)}{(\gamma + 1)W} + \frac{2}{\gamma - 1} \cdot \left(\frac{a_B}{a_A} - 1\right) \\ & - \frac{a_B}{a_A} \cdot \frac{1}{\gamma(\gamma - 1)} \ln \left[\left[\frac{2\gamma}{\gamma + 1} W^2 - \frac{\gamma - 1}{\gamma + 1} \right] \left[\frac{(\gamma - 1)W^2 + 2}{(\gamma + 1)W^2} \right]^\gamma \right] \end{aligned} \quad (D.8)$$

Relative Incoming Mach Number

$$W = -\frac{u_A}{a_A} = \frac{(q_A - V_s)}{a_A} \quad (D.9)$$

Speed of Sound Ratio

$$\frac{a_B}{a_A} = \frac{1}{(\gamma + 1)W} \left[2(\gamma - 1) \left[1 + \frac{\gamma - 1}{2} W^2 \right] \left[\frac{2\gamma}{\gamma - 1} W^2 - 1 \right] \right]^{\frac{1}{2}} \quad (D.10)$$

Velocity Change

$$\frac{q_A - q_B}{a_A} = \frac{2(W^2 - 1)}{(\gamma + 1)W} \quad (D.11)$$

Entropy Change

$$S_B - S_A = -\frac{1}{\gamma(\gamma - 1)} \ln \left[\frac{2\gamma W^2 - \gamma + 1}{\gamma + 1} \right] - \frac{1}{\gamma - 1} \ln \left[\frac{(\gamma - 1)W^2 + 2}{(\gamma + 1)W^2} \right] \quad (D.12)$$

APPENDIX E:

NODE TYPES

To identify every node a specific node tag is attached to each node in the computational grid. This numerical node tag identifies whether the node is

- on a solid wall
- on a periodic boundary
- on an inflow boundary
- on an outflow boundary
- a normal inner node
- a combination of the above.

The numerical node tag is obtained by adding up specific factors for each character.

The specific factors for different characters are summarised in Table E-1.

Table E-1. Specific Factors for Different Characters

<i>CHARACTER</i>		<i>FACTOR</i>
Node on the inflow surface	I=1	1
Node on the outflow surface	I=IMX	2
Node on the solid boundary	J=1	10
Node on the solid boundary	J=JMX	20
Node on the solid boundary	K=1	1000
Node on the solid boundary	K=JMX	2000
Node on the periodic boundary	K=1	100
Node on the periodic boundary	K=JMX	200
Node on the periodic boundary (leading edge)	I=ILE	1
Node on the periodic boundary (trailing edge)	I=ITE	2
Else (normal inner node)		0

Numerical tags for 2 and 3 dimensional flows are given in the following Figures and Tables.

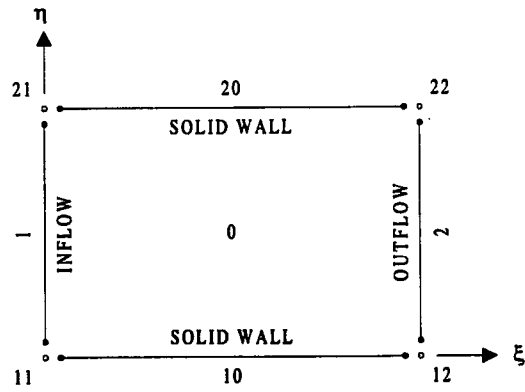


Figure E.1. Two-dimensional flow with solid wall boundaries

Table E.2. Node tags in two-dimensional flow with solid wall boundaries

0
1, 2
10, 20
11, 21
12, 22

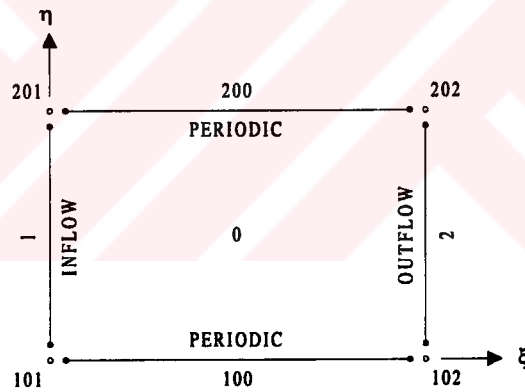


Figure E.2. Two-dimensional flow with solid wall boundaries

Table E.3. Node tags in two-dimensional flow with solid wall boundaries

0
1, 2
100, 200
101, 201
102, 202

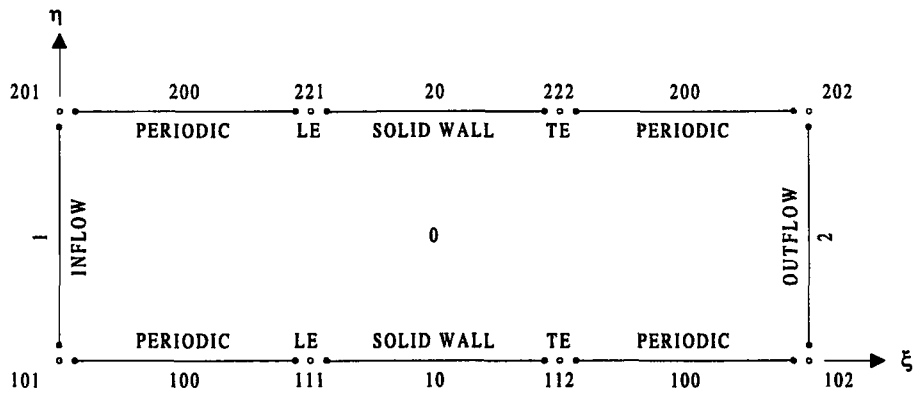


Figure E.3. Two-dimensional flow with solid wall and periodic boundaries

Table E.4. Node tags in two-dimensional flow with solid wall and periodic boundaries

0
1, 2
10, 20
11, 21
12, 22
100, 200
101, 201
102, 202
111, 112
221, 222

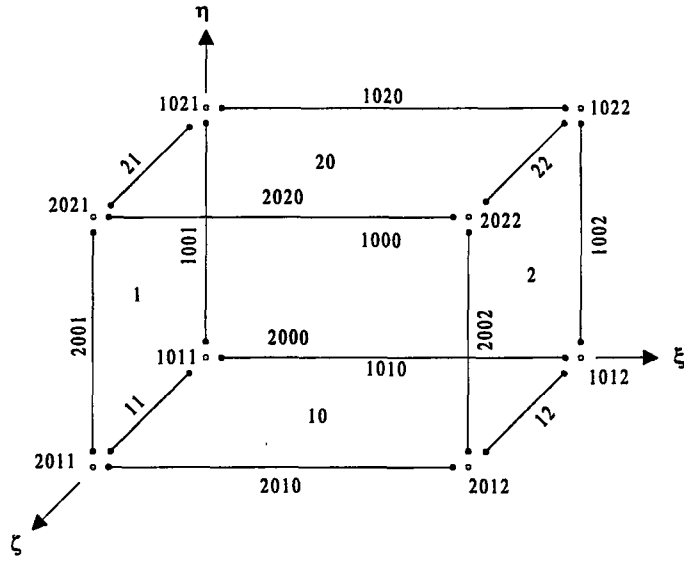


Figure E.4. Three-dimensional flow with solid wall boundaries

Table E.5. Node tags in three-dimensional flow with solid wall boundaries

0
1, 2
10, 20
11, 21
12, 22
1000, 2000
1001, 2001
1002, 2002
1010, 1020
2010, 2020
1011, 1021
2011, 2021
1012, 1022
2012, 2022

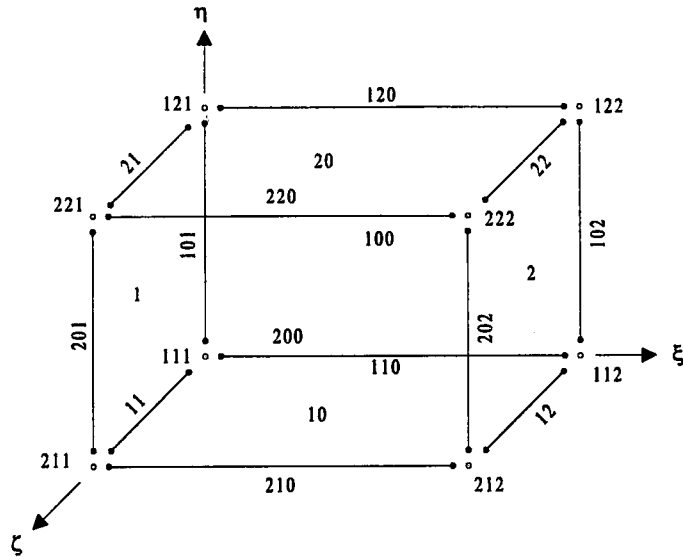


Figure E.5. Three-dimensional flow with solid wall and periodic boundaries

Table E.6. Node tags in three-dimensional flow with solid wall and periodic boundaries

0
1, 2
10, 20
11, 21
12, 22
100, 200
101, 201
102, 202
110, 120
210, 220
111, 121
211, 221
112, 122
212, 222

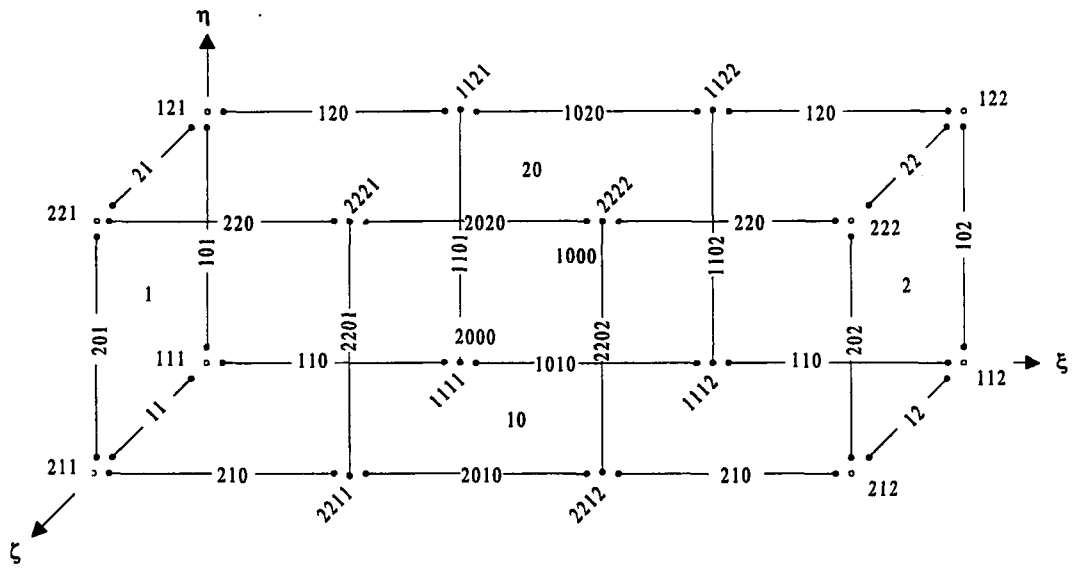


Figure E.6. Three-dimensional flow with solid wall and periodic boundaries

Table E.7. Node tags in three-dimensional flow with solid wall and periodic boundaries

0
1, 2
10, 20
100, 200
1000, 2000
11, 21
12, 22
101, 201
102, 202
110, 210
120, 220
1010, 2010
1020, 2020
1101, 2201
1102, 2202
121, 221
111, 211
112, 122
212, 222
1111, 1112
1121, 1122
2211, 2212
2221, 2222

APPENDIX F:

COMPONENTS OF UNIT VECTORS s , n & m

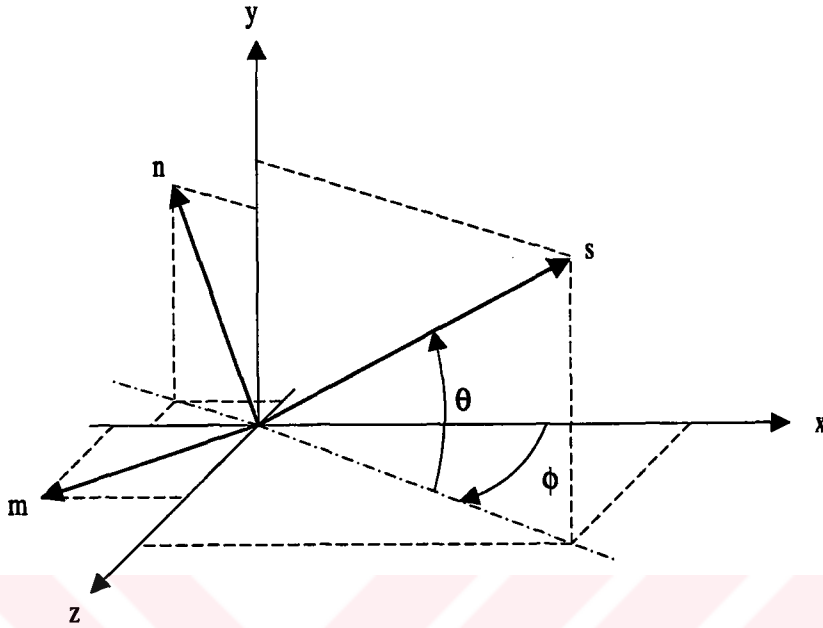


Figure F.1. Streamline coordinate system

$$s_x = \cos \theta \cos \phi \quad (\text{F.1})$$

$$s_y = \sin \theta \quad (\text{F.2})$$

$$s_z = \cos \theta \sin \phi \quad (\text{F.3})$$

$$n_x = -\sin \theta \cos \phi \quad (\text{F.4})$$

$$n_y = \cos \theta \quad (\text{F.5})$$

$$n_z = -\sin \theta \sin \phi \quad (\text{F.6})$$

$$m_x = -\sin \phi \quad (\text{F.7})$$

$$m_y = 0 \quad (\text{F.8})$$

$$m_z = -\cos \phi \quad (\text{F.9})$$

T.C. YÜKSEKÖĞRETİM ENSTİTÜSÜ
DOKÜMAN

VITA

Ertuğrul Başeşme was born in Ankara, Turkey, on June 21, 1966. He attended the Middle East Technical University, Ankara, Turkey. Ranking top of his class he graduated in 1988 with high honours and a bachelor of mechanical engineering degree. From 1988 to 1990, he attended the Lehigh University, Pennsylvania, USA under research assistantship, graduating with a MSc. degree in mechanical engineering. He joined the Aerospace Design Technology Group (ADTG) in 1991. He received the Parlar Award due to "Research on the Internal Ballistics and External Aerodynamics of Rockets" in 1992 as a member of ADTG. In 1991 he joined Roketsan Missiles Industries Engineering Development Group where he took active part in design, development and testing of artillery rockets and rocket launchers. He has publications in Powder Technology and AIChE Annual Meeting due to his studies on the Wake Exchange in Bubbling Fluidized Beds.